Alma Mater Studiorum · Università di Bologna

DOTTORATO DI RICERCA IN
FISICA
Ciclo XXVII

Settore Concorsuale di afferenza: 02/B1
Settore Scientifico disciplinare: FIS/03

Nanocrystalline Silicon Based Films for Renewable Energy Applications

Presentata da: Martina Perani

Coordinatore Dottorato:
Prof. Fabio Ortolani

Relatore:
Prof. Daniela Cavalcoli

Esame finale anno 2013/2014

Contents

Introduction

In the last century, greenhouse gases (GHGs) emissions have greatly increased due to the development of industrialization. This fact lead to significant climate changes such as: warming of the Earth surface and atmosphere, changes in the precipitation patterns, shrink of the sea-ice coverage and acidification of the oceans [1]. Emission reduction and international politics aimed to the conversion towards a low carbon society are necessary in order to reduce the effect that human activity has on the Earth.

Research in the renewable energy field is mandatory within this framework to provide alternatives to fossil fuels in energy production. Among the available renewable energy sources, photovoltaics is one of the most promising as solar energy is widely distributed over the Earth. The related technology is nowadays easily available, it can be integrated with buildings and presents limited environmental issues [2].

Among photovoltaic technologies, Si-based solar cells are still the most investigated and promising. Silicon is indeed a widely known material, abundant, diffuse and non-toxic. 90% of the current market is constituted by Si-based solar cells [3]. Within this framework, two different systems which could lead to a substantial improvement of Si-based cell efficiency will be investigated in the present thesis. In particular, Silicon Oxi-Nitride (SiO_xN_y) thin films and multilayers of Silicon Rich Carbide (SRC)/Si have been characterized in view of their application in photovoltaics.

The study has been carried out at the Physics and Astronomy Department of the University of Bologna, Italy, in close cooperation with the University of Konstanz, Germany, and the CNR IMM Institute of Bologna, Italy.

The technologies under study share a basic assumption: the constituent

materials of a cell should be abundant and non-toxic and the research should go in the direction of cost reduction and efficiency improvement [4]. Silicon offers the above mentioned properties, together with its mature technology industry.

One of the key factors responsible for power loss in single band gap solar cells is that photons with energy higher than the band gap lose their excess energy by thermalization, while photons with energy below the band gap are not successfully converted. One way to overcome this limit is to introduce the multi-junction concept, where materials with different band gap are stacked together [5, 6]. In this framework, silicon nano-crystals (Si NCs) embedded in a dielectric matrix were proposed as absorbers in all-Si multi-junction solar cells due to the quantum confinement capability of Si NCs, that allows a better match to the solar spectrum thanks to the size-induced tunability of the band gap [7, 8]. SiC as a dielectric matrix is considered promising as it shows better conduction properties and lower barrier to the Si NCs with respect to e.g. SiO_2 [5, 6]. Despite the efficient solar radiation absorption capability of this structure, its charge collection and transport properties have still to be fully demonstrated. The results presented in the thesis aim to the understanding of the transport mechanisms at macroscopic and microscopic scale. Current Atomic Force Microscopy (c-AFM) has been used to investigate the conductivity at the nano-scale and to perform local current-voltage measurements. Macroscopical IV curves as a function of temperature have been employed to gain information about the transport mechanism.

SiO_xN_y is a promising material for applications in thin-film solar cells, e.g. as window layer or intermediate reflector [9, 10] as well as for wafer based silicon solar cells, like Silicon HeteroJunction (SHJ) solar cells. It has already been shown that the utilization of amorphous silicon oxide (a-SiO_x) or amorphous silicon oxy-nitride (a-SiO_xN_y) instead of amorphous silicon (a-Si) as emitter layers in SHJ solar cells can boost the solar cell efficiency due to a reduced parasitic absorption in the emitter layer [11, 12]. An additional efficiency gain can be expected by replacing the amorphous emitter with a nanocrystalline emitter layer, due to the higher conductivity of the latter and the lower contact resistance between the nc-emitter and the transparent

conductive oxide layer [13]. In addition, nc-SiO_x and SiO_xN_y layers might be superior to nc-Si layers as they suffer less from parasitic absorption due to higher optical band gap. Notwithstanding those interesting properties, many issues relevant to the material properties have not been studied yet, such as the role of the deposition condition and precursor gas concentrations on the optical and electronic properties of the film, the composition and structure of the nanocrystals. The results presented in the thesis aim to clarifying several aspects concerning nc-SiO_xN_y film properties in view of its photovoltaic applications. The process of nanocrystal formation have been investigated through structural, compositional and optical methods. The morphology as well as the local conductivity of the layers has been measured with the AFM. The effects of the annealing and the oxygen incorporation within the SiO_xN_y layers have been clarified.

The outline of the thesis is the following: Chap. 1 introduces the energy challenges that our society should address and it briefly reviews the state of the art of quantum dots and HIT solar cells; the materials and analysis strategies used for the systems under study are described in Chap. 2 and the results obtained for SRC/SiC multilayers and SiO_xN_y thin films are reported in Chap. 3 and 4, respectively. Finally, some conclusions about the obtained results are presented.

Chapter 1

The Energy Challenge

1.1 The climate change

In the last century, greenhouse gases (GHGs) emission have greatly increased due to the development of industrialization. Although greenhouse effect exists in nature, allowing the Earth to be warm and develop life as we see it in present days, the increment of this natural phenomenon due to human GHGs emission is leading to major changes in climate.

Greenhouse effect is caused by GHGs (mainly H_2O, CO_2, CH_4 and N_2O), which are able to absorb an re-emit radiation in the infra-red (IR) region of the electromagnetic spectrum. The IR radiation is initially emitted e.g. by the Earth and the clouds and is then re-emitted isotropically by the GHGs, so that part of it goes back through the Earth causing a warming effect.

The main reasons for the climate changes are the land usage (e.g. deforestation), that causes changes in Earth surface reflectivity, and GHGs emissions [14]. There are multiple consequences on climate and its evolution takes places on very large time scales. Nowadays, measurements relative to the last century are available and several models have been proposed in order to predict future scenarios. Some of the main effects observed are [1, 14]:

- warming of the Earth surface and atmosphere (0.72°C between 1951 and 2012);
- changes in the precipitation patterns, with an enhancement of rain in

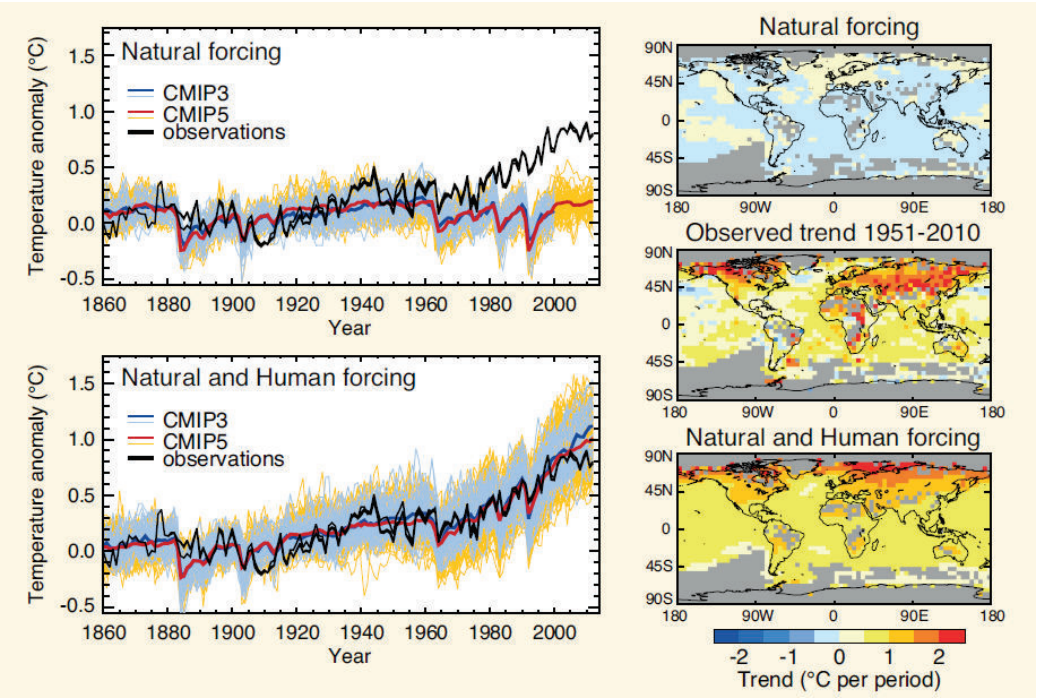

Figure 1.1: (left) Observed and simulated surface temperature changes in the period 1860-2010. Simulations taking into account only natural (top) and natural and human forcing (bottom) are reported. (right) Spatial distribution of the local surface temperature changes in the period 1951-2010 related to simulated natural forcing (top), observed changes (middle) and simulated natural and human forcing (bottom) [15].

the northern and southern regions of the world and a reduction in some areas of the tropical region and the Mediterranean;

- shrink of the sea-ice coverage (-4.1%/year in the Arctic up to 2012) and reduced snow coverage;
- acidification of the oceans due to the dissolution of CO_2 in the oceans (reduction of pH of $\sim$0.1 units with possible problems for marine species with calcium carbonate skeletons), increasing of water temperature and rising of the sea level.

Several models are proposed to reproduce the climate observation. The Intergovernmental Panel on Climate Change (IPCC) reports on the evolution of the knowledge relevant to climate changes. The physical science basis

of climate changes has been examined in depth and reported in the Fifth Assessment Report (AR5) [1]. In the AR5 report, the models have shown improvements in the reproduction of climate phenomena with respect to AR4 (2007). The importance of having reliable models lies in the need of determination of future politics about GHGs emission that would reduce the human impact on the climate [16]. Even though all climate models are affected by uncertainties, the actual warming pattern could not be reproduced only by natural forcing (e.g. Sun irradiance variations, volcano explosions etc...), but anthropogenic forcing (such as GHGs emissions) needs to be included in the simulations [15]. Figure 1.1 show the comparison between the observed temperature changes in the period 1860-2010 and the simulations in two cases: when only natural forcing are inserted in the models and when also human forcing is taken into account. The observed and simulated data are in agreement only in the latter case, showing how important the human contribution is to the warming trend. The same agreement between observation and simulation (natural+human forcing) is observed when the spatial distribution of the local surface temperature variation is taken into account, as reported in Fig. 1.1.

In order to make projections on future climate, different emission scenarios are used as an input. The AR5 uses four Representative Concentration Pathways (RCP), relative to different GHGs emission hypothesis and include the influence of mitigation policies, unlike previous reports. The RCPs were selected in order to achieve a specific radiative forcing target in 2100 and to represent a large set of mitigation scenarios [1]. If GHGs emission will not be significantly reduced, a warming trend of air temperature, as well as a shrink of the Arctic ice coverage and an increase of the oceans water temperature is to be expected in the near term (up to 2035 [18]) as well as in the long term (up to the end of the 21st century [17]). Figure 1.2 shows the predicted global surface mean temperature changes in the near-term (left) and the local ones (right) for four different RCPs. These predictions underline how important a reduction of GHGs emission is to reduce human impact on Earth climate. One step in this direction is the improved use of renewable energies for generating electricity.

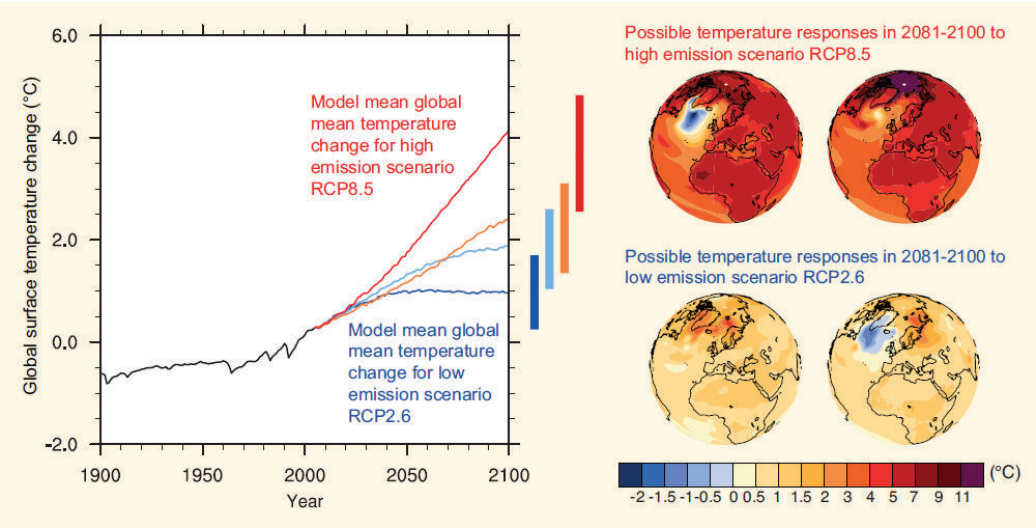

Figure 1.2: Global surface mean temperature changes (left) as predicted from the Coupled Model Intercomparison Project Phase 5 (CMIP5) for different RCP scenarios. The vertical bars represent the likely ranges (66%-100% likelihood) by the end of the 21st century. Surface temperature changes (right) for two different CMIP5 models in the high and low emission RCP scenarios [17].

Electricity generation contributes to ∼40% of the total CO_2 emissions, with a production of more than 10 gigatonnes per year [2]. Several carbon-free sources can be exploited, namely hydropower, nuclear fission, biomass, wind, geothermal, solar and ocean energy. Each one presents advantages as well as disadvantages, different capacity, cost and availability of the natural resource. Within this framework, solar energy will be the focus of this thesis and, in particular, innovative materials for photovoltaic application will be investigated.

1.2 Solar Cells

About 10^5 TW of solar power reach the Earth at its surface, providing every hour the energy that humanity needs in one year. Sunlight is also widely distributed and comes unlimited and without any cost [2]. The spectrum of the sun is shown in Fig. 1.3 and can be approximated by the spectrum of a

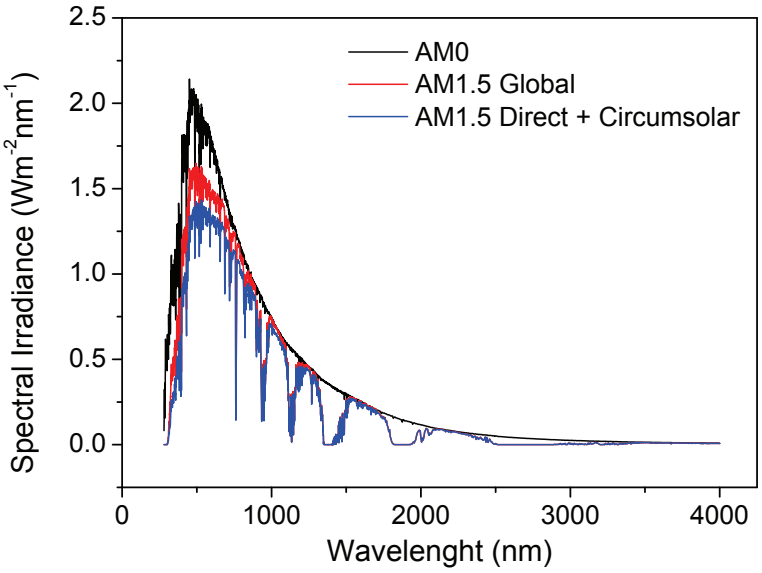

Figure 1.3: Solar irradiance spectra standards by American Society for Testing and Materials (ASTM). Extraterrestrial spectrum AM0 [22] and surface spectra AM1.5 [21]. Data plotted from the sources in [20].

6050 K black body. Several differences can be found between the spectra in Fig. 1.3 and a common black body spectrum because of the presence of the Earth's atmosphere and the main contributions are the water content, turbidity, cloudiness, ozone and ground reflection [19]. Commonly, the path length of the sunlight through the atmosphere is expressed in terms of equivalent air mass, m_r, for terrestrial applications. In particular $m_r = 1/\cos z$, where z is the zenith angle. Solar spectra are then addressed as AMm_r and the solar spectrum in outer space is conventionally labeled AM0 [19]. Figure 1.3 plots AM0 spectrum and AM1.5 spectra relative to the direct+circumsolar and global irradiance, which takes into account also other components, like reflected and diffused light [20–22].

Despite the abundance of the resource used for electricity generation, i.e. sunlight, conversion efficiency together with the variability of the above-mentioned resource are two of the main problems of the solar technology. Darkness as well as clouds do not allow for a stable electricity production

and therefore the integration with energy storage devices and the development of smart grids are necessary [2]. Efficiency improving is a goal of major importance in actual research, together with cost reduction and optimization of the processes for feasible industrial production. Figure 1.4 shows the evolution of solar cell efficiencies from the 1970s to present days for different technologies [20]. The highest achievements have been obtained so far for multijunction technologies used in combination with solar concentrators. c-Si solar cells currently represent ∼90% of the market because of two main factors: first of all, Si is stable, non toxic, abundant and its physical properties are well known. Secondly, the technology is mature, thanks also to the success Si has in microelectronic industry [3]. In the last decade, the efficiency of c-Si solar cells ranges from 20% to 25% (Fig. 1.4) and the highest efficiency (25.6%) for a c-Si solar cell has been achieved by Panasonic in 2014 for a Si Heterojunction with Intrinsic Thin layer (HIT). This record has been obtained for a cell of a practical size (143.7 cm^2) and improves the previous record of 0.6 points [23]. The HIT solar cells will be described in details in Sec. 1.3.2.

Photovoltaic (PV) devices exploit the incoming light to directly produce electricity through charge carries photogeneration. If the photons have an energy greater than the band gap, free electrons and holes are generated and extracted by means of an electric field before they recombine. Therefore, a reverse current density J flows into the external circuit and it is called short-circuit current J_{sc} under short-circuit conditions. The drift of the carriers through the photovoltaic material generates a potential difference ϕ, which is called open-circuit voltage ϕ_{oc} under open-circuit conditions [19]. In order to have a better performance of the photovoltaic device, it is necessary to maximize both J_{sc} and ϕ_{oc}. Therefore, some of the characteristics that the material should have are high minority carrier lifetime, high mobility and high absorption over a wide wavelength range in order to achieve high values of J_{sc}, while ϕ_{oc} strongly depends on the kind of transport mechanism involved and on the band gap of the material.

Figure 1.5a shows a simple example of a photovoltaic device, where the following different components are present: the current generator is related

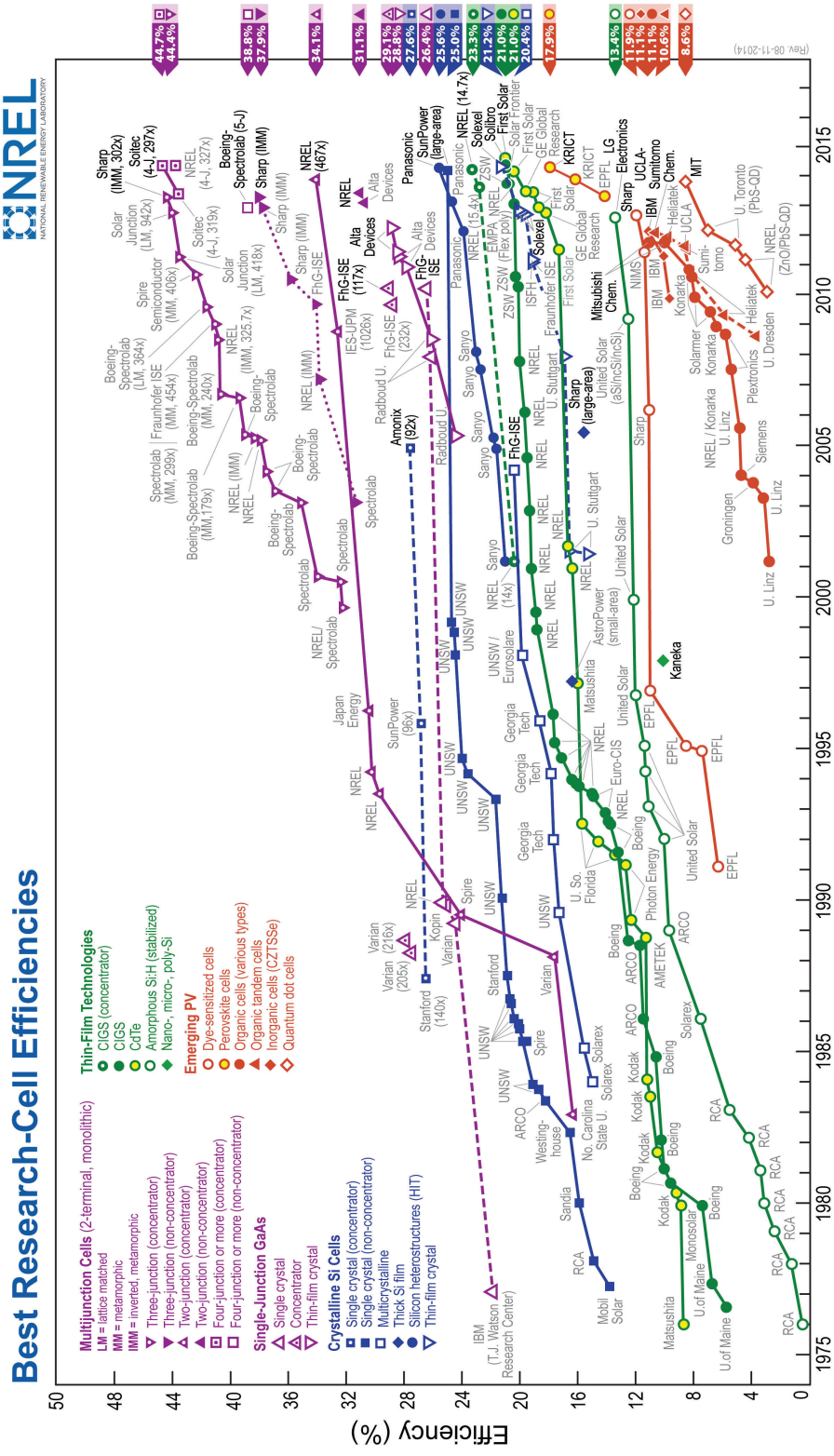

Figure 1.4: State of the art of the highest confirmed efficiencies for different photovoltaic technologies, as reported by NREL [20]. This plot is courtesy of the National Renewable Energy Laboratory, Golden, CO.

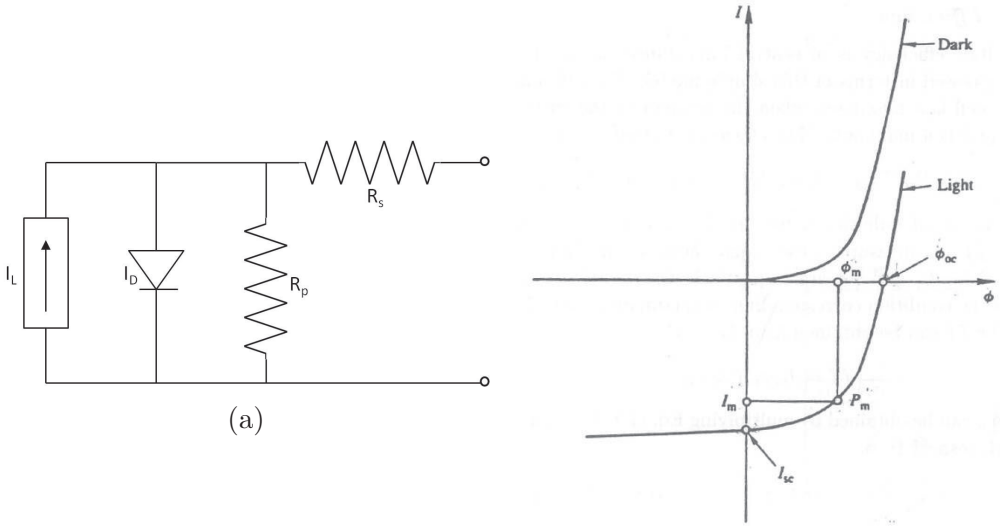

Figure 1.5: a) Schematic equivalent circuit for a photovoltaic cell. I_L represents the total light current, I_D the total dark current of the diode, R_s a series resistance and R_p a parallel resistance. b) Idealized total light and dark current versus voltage curves for a solar cell. ϕ_{oc} is the open-circuit voltage, I_{sc} is the short-circuit current and P_{m}. Plots adapted from [19].

to the photoexcitation process, the diode responsible for the electric field that drives the photogenerated carries outside the device, a series resistance R_s and a parallel resistance R_p. For an ideal device R_s=0 and $R_p = \infty$ and the photoinduced current is superimposed to the dark current. Therefore, the current density flowing in the device is given by:

$$J = J_0 \left[\exp\left(q\phi/AkT\right) - 1\right] - J_L \tag{1.1}$$

where J_0 is the reverse saturation current of the diode, A is the ideality factor (which depends on the mechanism of the junction transport) and J_L is the reverse current generated by the incoming light [19]. Figure 1.5b shows the typical idealized I-V response of a photovoltaic device in the dark and under illumination. When the bias applied is equal to zero, the resulting current in

the dark is zero, while under illumination the following relation is valid:

$$J_{\mathrm{sc}} = -J_L. \tag{1.2}$$

In the open-circuit condition the current density flowing in the device is zero and therefore:

$$\phi_{\mathrm{oc}} = (AkT/q) \ln \left[(J_L/J_0) + 1 \right], \tag{1.3}$$

while the dependence of J_{sc} by ϕ_{oc} can be written as:

$$J_{\mathrm{sc}} = J_0 \left[\exp \left(q\phi_{\mathrm{oc}}/AkT \right) - 1 \right]. \tag{1.4}$$

It is worth noting that Eq. 1.4 has the same functional form of the current flowing in the device in the dark [19]. The photovoltaic efficiency is defined as:

$$\eta = P_m/P_{\mathrm{rad}} = \frac{J_m \phi_m}{P_{\mathrm{rad}}} = \frac{J_{\mathrm{sc}} \phi_{\mathrm{oc}} FF}{P_{\mathrm{rad}}} \tag{1.5}$$

where P_m represents the maximum power, P_{rad} the incoming radiation power, J_m and ϕ_m the values of current density and voltage corresponding to the maximum power and *FF* is the fill factor. The latter is therefore defined as:

$$FF = \frac{J_m \phi_m}{J_{\mathrm{sc}} \phi_{\mathrm{oc}}}. \tag{1.6}$$

Doping of the semiconductor materials is used in order to build an internal electric field to separate and extract the photogenerated charge carriers. Figure 1.6a shows the energy diagram of a homojunction, which is defined as *p*-*n* junction where the *p* and *n* type portions are made of the same material. The quantities represented in the figure are the vacuum level E_{vac}, the conduction band edge E_c, the Fermi level E_F, the valence band edge E_v, the band gap E_g, the electron affinity χ_s and the diffusion potential $q\phi_D$. The band bending visible in Fig. 1.6a is due to the higher work function $q\phi_W$ of the *p* type portion with respect to the *n* type one. The diffusion potential is the difference between these two work function. The minority carriers photogenerated have to travel in the junction to be extracted in the external circuit. In order to do so, recombination should not occur and therefore the

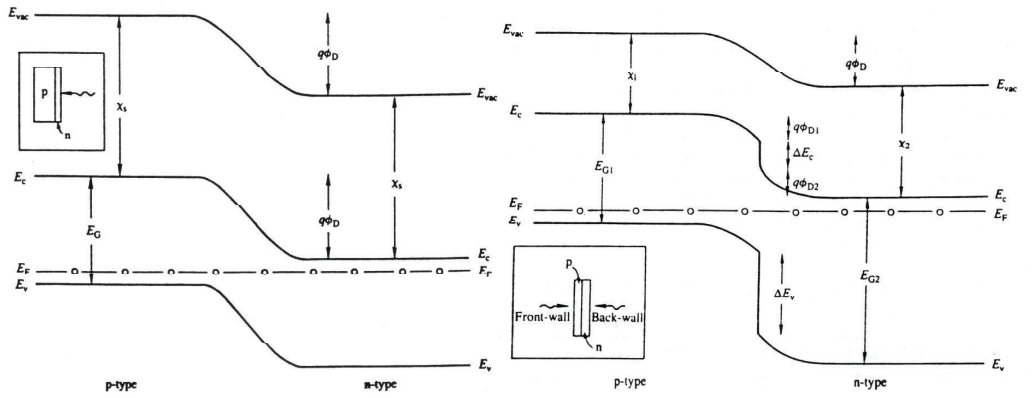

(a) (b)

Figure 1.6: a) Band diagram of a p-n homojunction. The density of the doping in the two sides is the same. b) Band diagram of a p-n homojunction. The density of the doping in the two sides is the same and $E_{g1} < E_{g2}$ and $\chi_1 < \chi_2$ [19].

carriers should be generated within one diffusion length of the junction. In practical cases this means that the illuminated side of the junction should be thinner than the opposite side [19]. Figure 1.6b shows the band diagram of a p-n heterojunction, where the p and n sides of the junction are made of different semiconductors. In this example the p type material has a smaller band gap (E_{g1}) with respect to the n type one (E_{g2}) and all the effects relevant to interface states have been neglected (Anderson abrupt junction model [24]). The difference between the two semiconductors generates discontinuities in the conduction and in the valence band, which can be either positive or negative [19]. The case represented in Fig. 1.6b is based on the assumption $\chi_1 < \chi_2$. If the light is coming on the n side, then this layer absorbs only higher wavelengths with respect to the p one as it has a wider band gap. Therefore, the n layer is acting as a window layer, letting part of the incoming light reach the p type portion with minimum losses. Interface states can act as recombination centers and contribute to an increase in J_0, resulting in a lower value of ϕ_{oc}. One way to overcome this limitation is the insertion of a passivation layer between the p and n layer, as it is done in Heterojunction with Intrinsic Thin Layer (HIT) solar cells, that are discussed

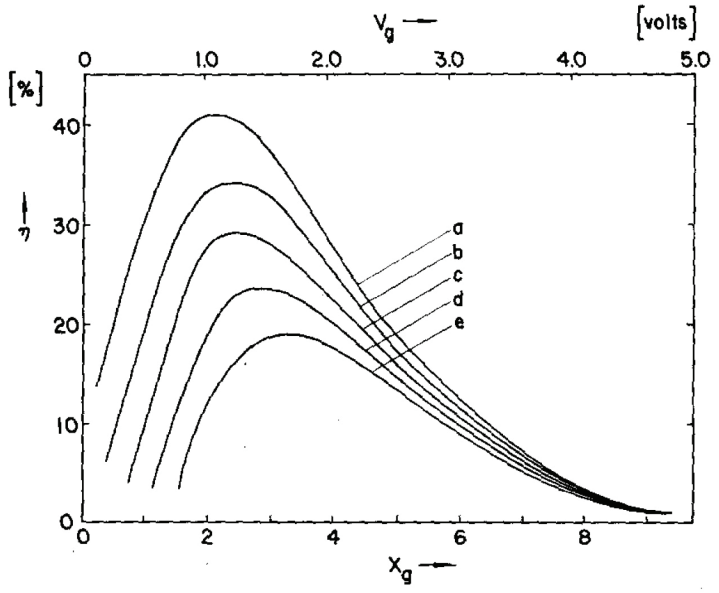

Figure 1.7: Black body solar cell efficiency η for a temperature of the cell of 300 K illuminated by the sun (modeled as a black body at 6000 K) as a function of the band gap for different values of the parameter f. From top to bottom: a) $f = 1$, b) $f = 10^{-3}$, c) $f = 10^{-6}$, d) $f = 10^{-9}$, e) $f = 10^{-12}$ [25].

in Sec. 1.3.

In order to better understand the potential of photovoltaic energy production, it is important to clarify which is the limit efficiency achievable from the devices. In 1961 Shockley and Queisser proposed the theory of the detailed balance limit for p-n junction solar cells [25]. In this work, the effect of radiative recombination in limiting the minority carrier lifetime is investigated and the upper limit efficiencies achievable for a solar cell are evaluated as a function of the band gap of the material, the temperature of the cell, the probability t_s that a photon with energy higher than the band gap generates a hole-electron pair and a parameter f. This parameter takes into account the reduction to the open circuit voltage due to a reduced efficiency of transmission of solar photons into the cell, a reduction of the solid angle subtended by the sun or its incidence upon the solar cell and the presence of additional non-radiative recombination processes. Figure 1.7 shows the predicted maximum efficiency as a function of the band gap of the material of a

solar cell for different values of f. A decrease of the efficiency for decreasing values of f (that is ≤ 1 by definition) is observed. The quantity x_g is defined as E_g/kT_s, where E_g is the band gap of the material that forms the cell, k is the Boltzmann's constant and T_s is the temperature of the sun. The quantity V_g is related to the energy gap by the relation $E_g = qV_g$, where q is the electronic charge. The maximum efficiency predicted by the theory for c-Si Solar cells (E_g=1.1 eV) is 30% [25]. It is worth noting that the highest record efficiency (up to date) is 25.6% for HIT solar cell (see Fig. 1.4), which is not so far from this theoretical limit.

Before the description of the solar cell technologies relevant to this thesis, a summary of some of the desirable material properties is given [19].

- One crucial point is the band gap of the material, that should be small enough to allow absorption of a wide range of the solar spectrum, but also large enough to minimize the reverse saturation current J_0. One way to allow a better match with the solar spectrum is the multi-junction concept, where different materials are stacked one on the top of the other in such a way that the material with wider band gap is placed on top and the others follow with decreasing energy gap. Another way to obtain this structure is the multilayer approach, that will be discussed in Sec. 1.3.

- The diffusion length of the minority carriers $L_{\min}$, which should be as large as possible so that carriers generated at a higher distance from the junction can actually be extracted before they recombine. The diffusion length is defined as:

$$L_{\min} = \left(D_{\min}\tau_{\min}\right)^{1/2} = \left[\left(kT/q\right)\left(\mu\tau\right)_{\min}\right]^{1/2} \tag{1.7}$$

  where $D_{\min}$ is the diffusion constant, $\tau_{\min}$ is the lifetime and $\mu_{\min}$ is the mobility of the minority carriers [19]. The value of the lifetime is influenced by several factors, one of which being the recombination at the surface. One way to overcome this limitation and obtaining higher values of $\tau_{\min}$ is the deposition of passivation layers, that is discussed

in Sec 1.3.

- In real cells it is valid that $R_s > 0$ and $R_p < \infty$. The presence of these resistances can contribute in the value of *FF* and therefore to the efficiency of the device. The series resistance can be increased by contact resistance between the semiconductor and the other circuit elements, e.g. the Transparent Conductive Oxide (TCO), used to extract the photogenerated charge carriers. The value of R_p can be reduced by defects and grain boundaries that contribute to a decrease of ϕ_{oc} [19].

- A solar cell is designed to operate under illumination and various weather conditions for a long period of time. Therefore, the stability of the device under such conditions is crucial and a significant reduction of the efficiency of the cell with exposure is undesirable.

1.3 New generation photovoltaics

In the following sections two of the many technologies relevant to the photovoltaic research will be briefly reviewed: the HIT solar cells and the quantum dots solar cells. These two technologies share a basic assumption: the constituent materials of a cell should be abundant and non-toxic and the research should go in the direction of cost reduction and efficiency improvement. In Chap. 3 the results obtained within the framework of these kind of devices are presented.

1.3.1 Quantum dots solar cells

Manipulating materials at the nano-scale allows to modify significantly their properties. In the photovoltaic field this fact is crucial as it allows to create new structures with enhanced optoelectronic properties, such as tunable band gap layers based on Si, whose bulk optical properties are relative poor. Therefore, nanostructured materials mark the beginning of a new era of silicon photovoltaics [26].

Reducing the dimension of a portion of material in one or more directions can lead to quantum confinement, quantum wires and quantum dots are examples of quantum confinement in two and three dimensions. The effective band gap of these structures depends on their size. Figure 1.8a shows the photoluminescence spectra of Si nanocrystals (NCs) with decreasing diameter and a blue shift is observed for smaller size of the NCs [26, 27]. The transition energy of an electron-hole pair of effective reduced mass m^* confined in a quantim dot can be written as:

$$E = E_g + \frac{\hbar^2}{2m^*}\left[\left(\frac{n_x\pi}{L_x}\right)^2 + \left(\frac{n_y\pi}{L_y}\right)^2 + \left(\frac{n_z\pi}{L_z}\right)^2\right] \sim E_g + \frac{\hbar^2}{2m^*}\left(\frac{n\pi}{d}\right)^2 \quad (1.8)$$

where L_x, L_y and L_z are the sizes of the quantum dot, E_g is the band gap of the bulk semiconductor, the confining energy barrier is assumed to be infinite and n_x, n_y and n_z are quantum numbers used to describe a given quantized energy level and d represents the diameter of the dot in case it is spherical [28]. Figure 1.8b reports the band gap of Si confined structures as a function of their size [29].

The size of the nanostructure controls also its electrical properties, such as the doping efficiency. Theoretical studies have shown that boron inclusion in the nanocrystals is favored for bigger diameter, while the position of the dopants is closer to the surface for smaller size of the nanostructure [30]. Figure 1.8c shows a linear increase of the impurity activation energy for increasing inverse radius both for B and P doped Si NCs. This dependence can be expressed for B doped NCs as:

$$E_{\mathrm{act}} = 0.050904 + \frac{16.298819}{R} \quad (1.9)$$

where R is the radius expressed in Å and E_{act} is the activation energy in eV [30].

Si based nanostructures provide the abundance, technological maturity and minimal environmental footprint of Si together with the possibility of band structure engineering and surface modification typical of the nanostructures [4]. In the photovoltaic field, all these characteristics can be used to

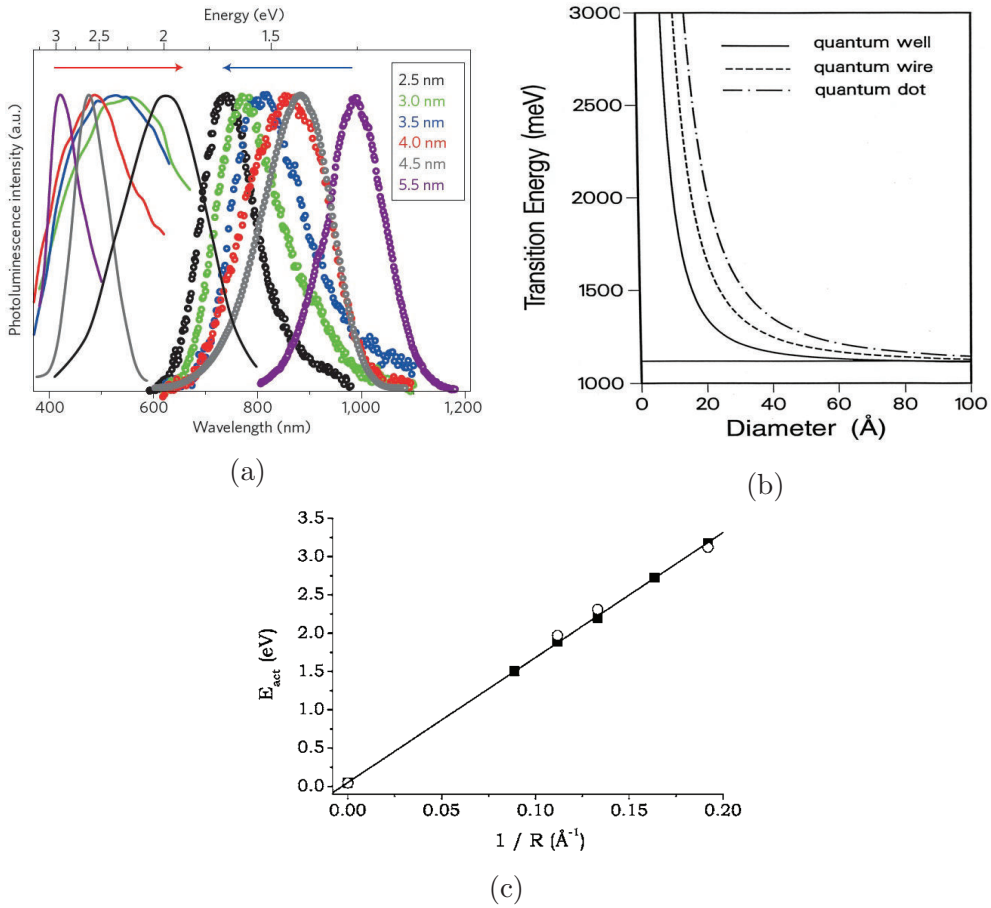

Figure 1.8: a) Normalized excitonic photoluminescence spectra on the longer wavelengths region, with a blue shift for smaller nanocrystal diameter [26]. b) Optical band gap of Si quantum wells, wires and dots as a function of the system diameter [29]. c) Impurity activation energy for B and P doped Si NCs as a function of the inverse nanocluster radius. Zero on the x-axis corresponds to bulk Si and the line is a fit for the B doped NCs. The impurity is considered at the cluster center [30].

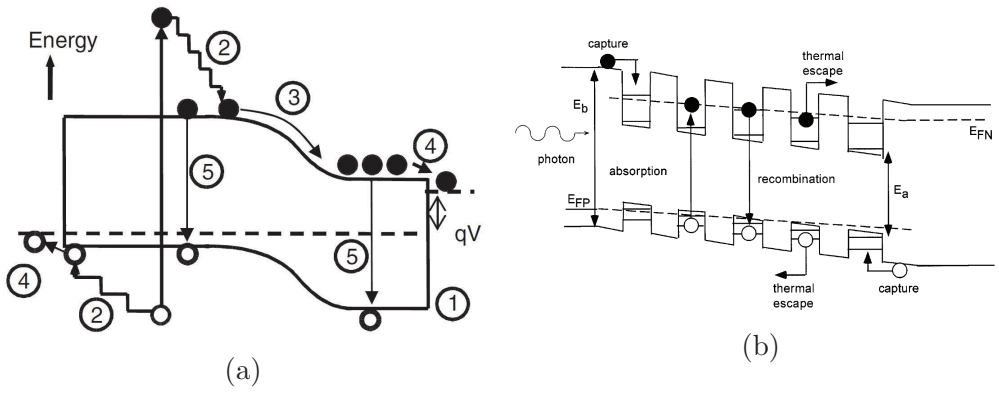

(a) (b)

Figure 1.9: a) Loss processes in a solar cell: 1) non-absorption of below band gap photons, 2) thermalization loss, 3) and 4) junction and contact losses, 5) recombination loss [5]. b) Band diagram for a multiple quantum well solar cell [8].

produce all-Si tandem cells, that will be described in detail in this section, as well as new kind of structures such as the solar shapers, that use the concept of *UV cutting* and *IR pasting* to convert the incoming light in a wavelength range suitable to high efficiency technologies [31–33].

All-Si tandem solar cells are studied within the concept of the third generation photovoltaics, that aims to an increase of the cell efficiency while using thin film processes and abundant, non-toxic materials [5]. Figure 1.9a shows several loss processes in a standard solar cell. Two important factors of losses are the inability to absorb photons with energy below the band gap and the thermalization of the photons with energy higher than the band gap (processes 1 and 2 in fig. 1.9a). Quantum Dots (QDs) superlattice tandem cells aim to solve these issues providing an increased number of band gaps within the photovoltaic device [5].

The structure of these devices is composed of Si nanocrystals embedded in a wider band gap matrix (such as SiO_2 or SiC). The NCs size should be small enough to obtain quantum confinement effects and with a spacing between the NCs small enough to allow an overlap of the wavefunctions of the confined carriers in adjacent dots. If these requirements are met, a mini-band is formed, resulting in a three band conduction mechanism. Figure 1.9b shows the band diagram of a Multiple Quantum Well (MQW) solar cell, that was

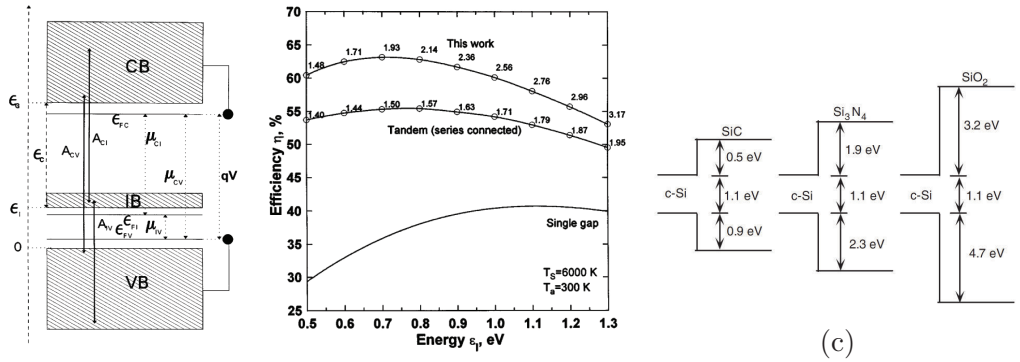

(a) (b) (c)

Figure 1.10: a) Band structure of a three band solar cell [34]. b) Detailed balance calculation for a single gap (lower), tandem (middle) and three band (top) solar cell as a function of the lowest band gap. The values of the highest band gap cell are also reported [34]. c) Band diagram alignments for bulk Si, SiC, Si_3N_4 and SiO_2 [5].

first proposed in 1990 [35] in order to absorb photons with energy as low as in the well region [8]. A detailed balance theory involving three energy level, as depicted in fig. 1.10a, suggested that a performance increase is possible with this structure [34]. The third band has an intermediate energy with respect to the valence and conduction band, radiative transitions between this band and the others are possible and charge carriers can flow inside it. Figure 1.10b shows the detailed balance efficiency limit calculated for a single junction (bottom), tandem cell (middle) and three band (top) solar cell [34]. The limit efficiency is plotted versus the lowest band gap value and close to each marker is reported the value of the highest band gap material used for obtaining maximum efficiency. Both tandem and three band devices exceed the Shockley-Queisser limit for a single junction cell and it is worth noting that the efficiency limit obtained for a three band solar cell can reach high values up to 63.1%.

The three band structure can be obtained with the superlattice approach previously described and band spacing as well as transport properties depend on the matrix in which the Si NCs are embedded. Figure 1.10c shows the bulk band alignments of crystalline Si and three different matrixes: SiC, Si_3N_4 and SiO_2. The latter displays a higher transport barrier with respect to Si_3N_4

and SiC. As the tunnel probability strongly depends on the barrier height, the presence of a smaller barrier allows a larger NCs spacing for obtaining the same tunneling current. The tunnel probability is given by:

$$T_e = 16 \exp\left(-\sqrt{\frac{8m^*}{\hbar}}\Delta E^{1/2} d\right) \tag{1.10}$$

where m^* is the bulk effective mass, ΔE is the energy difference between the bulk band and the one formed by the QD interaction and d is the spacing between the QDs [5, 36]. Therefore, a lower dot density is required for obtaining a given conductivity or a higher conductivity is reached for a given dot density.

In Chap 3 Si QDs/SiC MQW solar cells are described and electrical and morphological characterization carried out at macroscopical as well as microscopical level is presented.

1.3.2 HIT solar cells

The actual cost of a PV module includes the cost of silicon (50%), the cell processing (20%) and the module processing (30%) [37]. Therefore, reducing the amount of silicon used for fabrication of the cell is of major importance in cost reduction. If Si-wafers are thinner, recombination processes at the surface become more and more important and therefore good passivation is central in improving the cell efficiency. Silicon heterojunction are solar cells in which an amorphous silicon layer (a-Si:H) is deposited on top of the crystalline silicon (c-Si) active material. The efficiency of this kind of device at industrial production level is above 20% [3].

Recombination processes in silicon occur in large part through defect levels within the band gap. These defect can be either located within the bulk of the material or at the surface, the latter being a huge disturbance of the crystalline structure of the material [38]. A large density of surface defects is present due to non-saturated bonds, called dangling bonds. Long-term stable passivation of the surface is highly desirable in a solar cell to avoid undesirable drops in the cell efficiency. The recombination rate U_s through

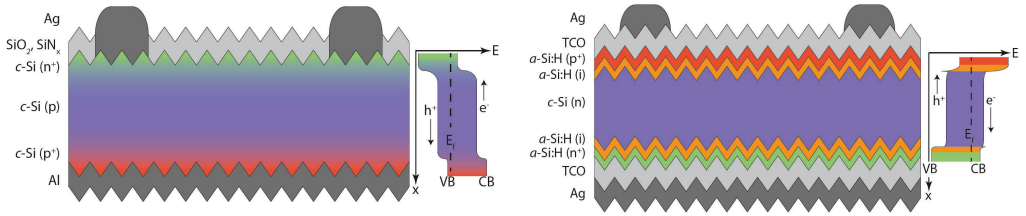

(a) (b)

Figure 1.11: a) Schematic view of a diffused junction solar cell with a p-type silicon wafer, and its band diagram. b) Schematic view of a SHJ cell developed by Sanyo, with a n-type silicon wafer, and its band diagram [3].

a surface state at energy E_t is given by the Shokley-Read-Hall theory [39]:

$$U_s = \frac{n_s p_s - n_i^2}{\frac{n_s+n_1}{S_{p0}} + \frac{p_s+p_1}{S_{n0}}} \tag{1.11}$$

with

$$n_1 = n_i \exp \frac{E_t - E_1}{kT}, \quad p_1 = n_i^2/n_1, \quad S_{n0} = s_n n_{th} N_{st}, \quad S_{p0} = S_p n_{th} N_{st} \tag{1.12}$$

where n_s and p_s are the electron and hole concentrations at the surface, n_i is the intrinsic carrier density, S_{n0} and S_{p0} are the parameters of surface recombination velocity for electrons and holes, E_i is the intrinsic Fermi level, N_{st} is the density of the surface defects, n_{th} is the thermal velocity of the carriers ($\sim 10^7$ cm^{-1} at 300 K in Si) and T is the temperature [38]. There are two possibilities to reduce the recombination rate: the reduction of the density of the surface states and the reduction of the free electrons and holes at the surface. The latter can be achieved by the implementation of a doping profile below the surface, while reduction of surface states is achieved by passivation as it is done in HIT solar cells [38].

Figure 1.11 depicts the structure and the band diagram of a traditional diffused junction solar cell (Fig. 1.11a) and of a HIT device (Fig. 1.11b). In the first structure, passivation of the front surface can be achieved by thermal growth of SiO_2 (which is carried out at very high temperatures) or by silicon nitride or aluminum oxide films. In the structure depicted in

Fig. 1.11a the rear side of the cell is not passivated and therefore the c-Si active material is directly in contact with the highly recombination active metal contacts [3]. In high efficiency diffused junction, the rear side is passivated as well. Figure 1.11b depicts the structure of a HIT solar cell. In this device, the passivating heterostructure acts also as contact, with no need of spiking metal contacts through the passivating layer. In Silicon Hetero-Junction (SHJ) solar cells the charge can trickle through the wide band gap amorphous layer slowly enough to build up a high voltage, but fast enough to avoid recombination. Therefore, the amorphous layer can be viewed as a semi-permeable membrane for carrier extraction [3].

a-Si:H has a wider band gap with respect to c-Si, it is easily doped and it has been therefore regarded as a good candidate for the buffer layer. The passivation is achieved by hydrogenation of Si dangling bonds, with a reduction of the surface defects. Nevertheless, the lifetime of the carriers generated in the amorphous layer is short and a large fraction of the photogenerated carriers recombine there. Another limitation of a-Si:H is the light degradation induced by Staebler-Wronski effect, which causes the lack of stability of a-Si:H. Silicon oxi-nitride (SiO_xN_y) has been studied because it shows improved properties with respect to a-Si:H, such as reduced parasitic light absorption and higher band gap [12]. Moreover, nc-SiO_xN_y could offer improved transport properties, particularly a lower contact resistivity with the Transparent Conductive Oxide (TCO) with respect to an amorphous layer [13]. The obtained results are described in Chap. 4.

The major breakthrough in SHJ solar cells has been the insertion of the amorphous undoped layer, forming the HIT structure. Figure 1.12a shows the minority carrier lifetime for different structures. The values achieved with passivation through doped layers (red curve) is less effective that the one achieved with an intrinsic buffer layer (green curve). This effect is due to doping related defect generation in the amorphous matrix [3]. A doped layer is required nonetheless for carrier extraction, and so a ni/c-Si/ip structure should be formed. The minority carrier lifetime of such a device is also reported in Fig 1.12a and a small loss with respect to the i/c-Si/i case is visible. Note that for the blue curve both front and rear side of the c-Si

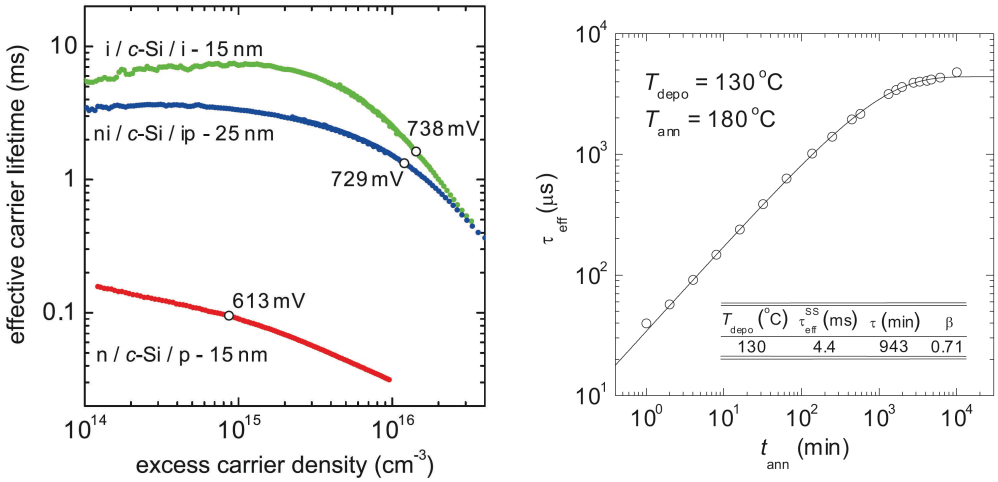

(a) (b)

Figure 1.12: a) Minority carrier lifetime for a-Si:H passivated layer for different structures. The voltage on the curves represents the implied ϕ_{oc} under 1 sun illumination. b)Minority carrier lifetime as a function of the annealing time (annealing temperature 180 °C for a FZ wafer passivated on both sides by 50 nm of a-Si:H [3].

wafer are passivated.

A short annealing at low temperatures generally improves the passivation of Si surfaces. Figure 1.12b shows the minority carrier lifetime as a function of the annealing time for a FZ wafer passivated by a-Si:H on both sides. The annealing temperature is 180 °C. Lifetime data can be fitted by the following relationship:

$$\tau_{\text{eff}}(t_{\text{ann}}) = \tau_{\text{SS}} \left[1 - \exp - \left(\frac{t_{\text{ann}}}{\tau} \right)^{\beta} \right] \tag{1.13}$$

where τ_{eff} is the minority carrier lifetime, τ_{SS} is the steady-staty value of T_{eff}, t_{ann} is the annealing time and β is the dispersion parameter, which ranges between 0 and 1 [3].

An atomically sharp interface between the c-Si wafer and the amorphous layer is a key feature to have good passivating properties. This means that no crystalline material should be deposited on the active layer. Despite this fact, a crystalline doped layer is desirable because it reduces the contact resistivity between the emitter and the TCO layer deposited on top of the structure.

For this reason nanocrystaline SiO_xN_y layers have been investigated and the results are described in Chap. 4.

Chapter 2

Materials and methods

In the following sections, Silicon Rich Carbide (SRC)/SiC multilayer and SiO_xN_y thin film preparation is described and previous results obtained on such systems are summarized. The techniques and the data analyses used for the characterization are depicted as well. Section 2.1 is focused on SRC/SiC multilayer deposition, Sec. 2.2 outlines the growing procedure of SiO_xN_y films, while Sec. 2.3 reviews the experimental techniques and analysis strategies used.

2.1 SRC/SiC multilayers

SRC/SiC multilayers (ML) were deposited by PECVD on quartz at CNR-IMM in Bologna. The precursor gases used are SiH_4, CH_4 and H_2, the temperature of the substrate is 325°C [40]. The multilayers are composed by a stack of 30 bi-layers of SRC and SiC, as depicted in Fig. 2.1a. The silicon fraction in the SRC layers is 0.85. The thickness of the as-deposited layers is 9 nm for SiC (d^0_{SiC}) and varies between 2 and 4 nm for SRC (d^0_{SRC}). An annealing step at 110°C for 30 minutes in flowing N_2 and 10% O_2 has been performed for Si and SiC NCs formation [41]. A sacrificial a-Si:H layer (20 nm thick) was deposited on top of the multilayer structure in order to prevent SiC surface oxidation during the annealing.

Reference single layers a-SiC:H and a-Si:H were deposited for comparison:

Sample name	d^0_{SiC} (nm)	d^0_{SRC} (nm)	d_{SiC} (nm)	d_{SRC} (nm)
X9-2	9	2	5±1	2.0±0.5
X9-3	9	3	5±1	3.0±0.5
X9-4	9	4	5±1	4.0±0.5

Table 2.1: As-deposited and post-annealing SiC and SRC thicknesses of samples deposited on quartz. Adapted from [40].

nc-SiC and nc-Si were produced by annealing at 1100°C, a-SiC and a-Si by dehydrogenation at 600°C. The preparation of all the samples was completed by wet etching of the sacrificial layer as described in [42]. Figure 2.1b shows a schematic view of the ML after annealing and Tab. 2.1 summarizes the thicknesses of the SiC and SRC layers in the as-deposited state and after the annealing. The sample are named as X9 followed by a number that represents the thickness of the SRC layers, d^0_{SiC} and d^0_{SRC} represent the as-deposited thicknesses of the SiC and SRC layers, respectively, and d_{SiC} and d_{SRC} the post annealed ones. The latter have been evaluated by Summonte *et al.* [40] taking into account the shrinking factors of such layers using the following equation:

$$d_{\mathrm{SiC}} = F d_{\mathrm{SiC+SRC}} \qquad d_{\mathrm{SRC}} = (1-F) d_{\mathrm{SiC+SRC}} \tag{2.1}$$

where $d_{\mathrm{SiC+SRC}}$ is the SRC+SiC bilayer thickness anf F is determined using:

$$F = \frac{d^0_{\mathrm{SiC}} S_{\mathrm{SiC}}}{d^0_{\mathrm{SiC}} S_{\mathrm{SiC}} + d^0_{\mathrm{SRC}} S_{\mathrm{SRC}}(x)}, \tag{2.2}$$

where S_{SiC} and $S_{\mathrm{SRC}}(x)$ are the shrinking factors of SiC and SRC layers, respectively. S_{SiC} is equal to 0.53, while $S_{\mathrm{SRC}}(x)$ is determined using:

$$S_{\mathrm{SRC}}(x) = 0.114 + 0.83x \tag{2.3}$$

where x is the Si fraction, which is equal to 0.85 for the multilayers under investigation [40].

Parallel Ni pads were deposited on the top surface of the multilayers

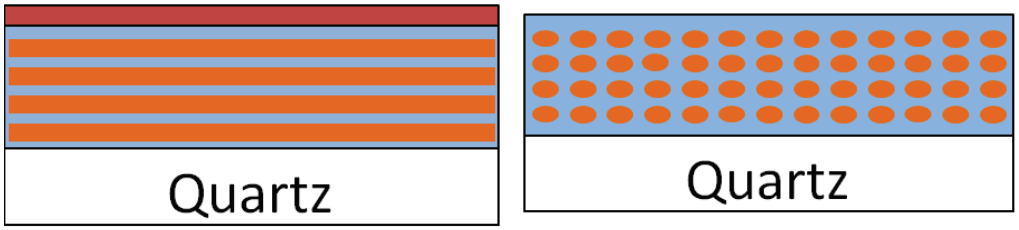

(a) (b)

Figure 2.1: a) Sketch of the SRC/SiC multilayer deposited by PECVD and (b) ML structure after the annealing (not in scale). The SRC layers (a) and the Si nanocrystals (b) are represented in orange, while the SiC layers in blue.

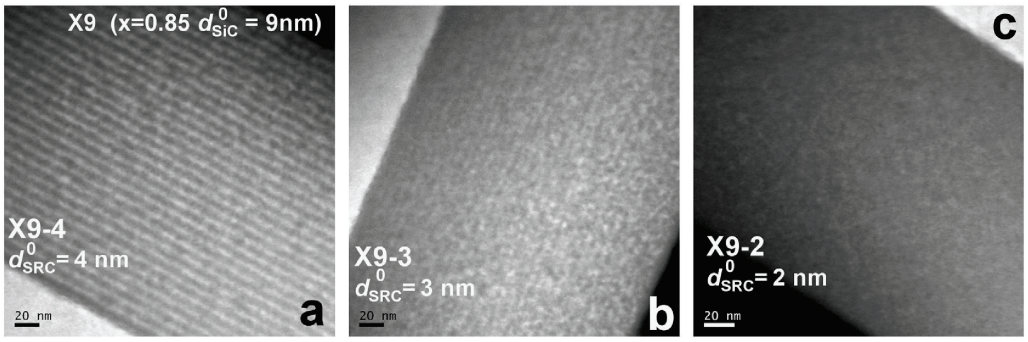

Figure 2.2: EF-TEM images of the cross section of samples X9-2, X9-3, X9-4 [40].

by thermal evaporation for current-voltage measurements. A dry etching (SF_6+0_2, 20 s) was used to remove the shallowest 5-10 nm from the surface before local conductivity measurements. In all cases the SiC-rich surface was effectively thinned. The thickness of the dry-etched layer was measured by fitting the R&T spectra of the layers before and after the etching treatment [43].

Figures 2.2 and 2.3 report previous results obtained on SiC/SRC multilayers by Energy filtered Transmission Electron Microscopy (EF-TEM) and X-Ray Diffraction (XRD) [40]. EF-TEM cross section maps of the sample under investigation show how the ML structure is well defined for d_{SRC}= 4nm (Fig. 2.2a), while it is less defined for decreasing d_{SRC} and it is lost for sample X9-2 (Fig. 2.2c).

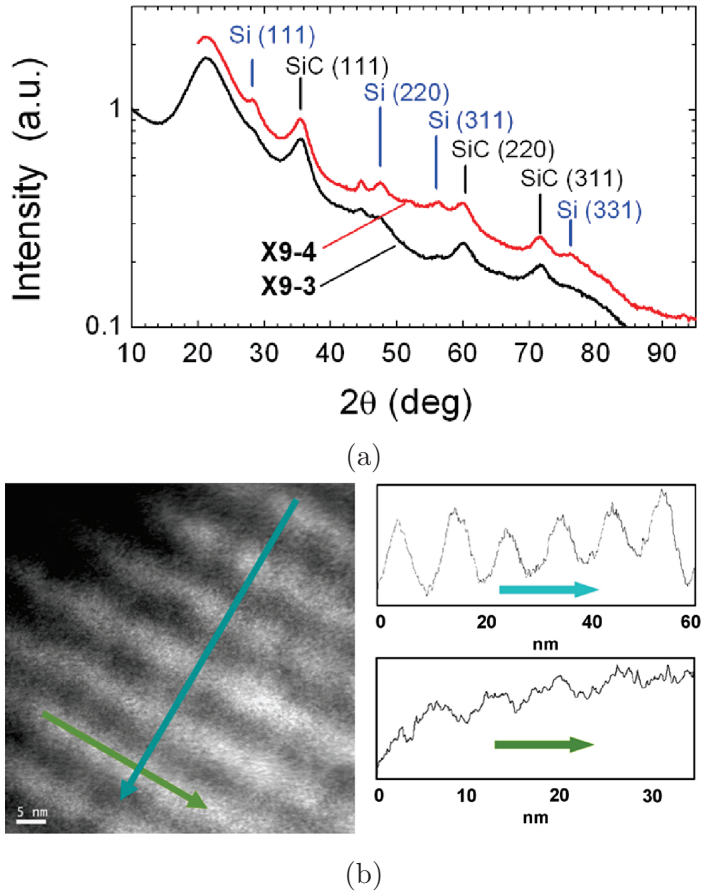

Figure 2.3: a) X- Ray diffraction spectra of sample X9-3 and X9-4 [40]. b) EF-TEM picture of sample X9-4 after annealing and intensities profiles across the ML (top) and along a SRC plane (bottom). Adapted from [40].

XRD underlines the presence of crystallized phases relative to SiC and silicon features are visible for samples X9-3 and X9-4, indicating the formation of Si nanocrystals (NCs). The results are reported in Fig. 2.3a and the average diameters obtained for samples X9-3 and X9-4 are (1.5±1.0) nm and (4.0±0.5) nm, respectively. TEM measurements of the ML deposited on Si reveal NC sizes of (4.3 ± 0.3) nm and (5 ± 1) nm for samples X9-3 and X9-4, respectively [40]. Figure 2.3b shows a magnified EF-TEM picture of sample X9-4 and the intensity profiles obtained across the multilayer and along a SRC layer. The intensity does not vanish along the SRC plane, and this fact could be due either to the presence of touching NCs or to the projection of NCs positioned at different depths onto the same location [40].

2.2 SiO_xN_y thin films

nc-SiO_xN_y layers are grown by Plasma Enhanched Chemical Vapor Deposition (PECVD) using a commercial system (PlasmaLab 100 from Oxford Instrument) in a parallel plate configuration [44]. The radio frequency (RF) is set at 13.56 MHz. Silane (SiH_4), hydrogen (H_2) and nitrous oxide (N_2O) are used as precursor gases, while diborane (B_2H_6) is added in order to obtain p-type doping [44]. Diborane is diluted in hydrogen (0.5%). The nitrous oxide gas flow is referred to its dilution in silane and the same is done for diborane ratio. Thus, we can define N_2O and B_2H_6 gas flows ratio as:

$$R_{\mathrm{N2O}} = \frac{[N_2O]}{[N_2O] + [SiH_4]} \tag{2.4a}$$

$$R_{\mathrm{B2H6}} = \frac{[B_2H_6]}{[B_2H_6] + [SiH_4]}, \tag{2.4b}$$

where the gas concentration are in square brackets.

All the results that will be presented are related to layers deposited at a temperature of 300 °C with R_{B2H6}=2.34% and subsequently annealed at 800 °C in order to obtain nanocrystals formation. The same effect could be achieved with an enhancement of the hydrogen dilution during the deposition phase, but an annealing step has been necessary due to technical limitation

Sample name	Annealing time (h)	R_{N2O} (%)	R_{B2H6} (%)	Thickness (nm)	Rate ($\AA$/s)
A	0, 3, 6	9.09	2.34	209	2.32
B	0, 3, 6	16.7	2.34	224	2.49
C	0, 3, 6	23.1	2.34	270	3.00
D	0, 3, 6	28.6	2.34	255	2.83
E	0, 3, 6	47.4	2.34	283	3.14
R	0, 3, 6	0	2.46	177	1.97

Table 2.2: Deposition parameters of SiO_xN_y thin films. All the layers have been deposited on glass and Si substrates.

of the H_2 to SiH_4 ratio in the system used. Table 2.2 shows the deposition parameters of the thin films, the thickness measured by ellipsometry and the corresponding growth rate. Titanium/palladium/silver parallel contacts have been deposited by electron beam evaporation on the top surface of the layers deposited on glass to measure the lateral conductivity. The layers are sintered after the contacts deposition for 90 minutes at 150 °C in a nitrogen atmosphere in order to obtain good ohmic contacts between the metal and the nc-SiO_xN_y layers.

Previous studies have been carried out on a-SiO_xN_y thin films to investigate their properties as passivating layer in Heterojuntion with Intrinsic Thin layer structures by Brinkmann *et al.* [12]. Figure 2.4a [12] shows a High Resolution Transmission Electron Microscopy (HR-TEM) image of an a-SiO_xN_y layer deposited on FZ Si substrate. The measurement has been done close to the interface between the layer and the substrate and no crystals are visible within the SiO_xN_y film, further confirming their amorphous nature. Figure 2.4b [12] reports the results of SIMS measurements on the B-doped a-SiO_xN_y layers. It can be seen that B and N concentrations do not increase significantly with increasing R_{N2O}, while the O content within the layer increases of almost four times going from R_{N2O}=17% up to 45%. The frequency of the Si-O-Si bond measured by FTIR as a function of R_{N2O} is reported in Fig. 2.4c [12] for B- and P-doped a-SiO_xN_y layers. The linear shift of the peak position is due to the homogeneous distribution of Si-Si and

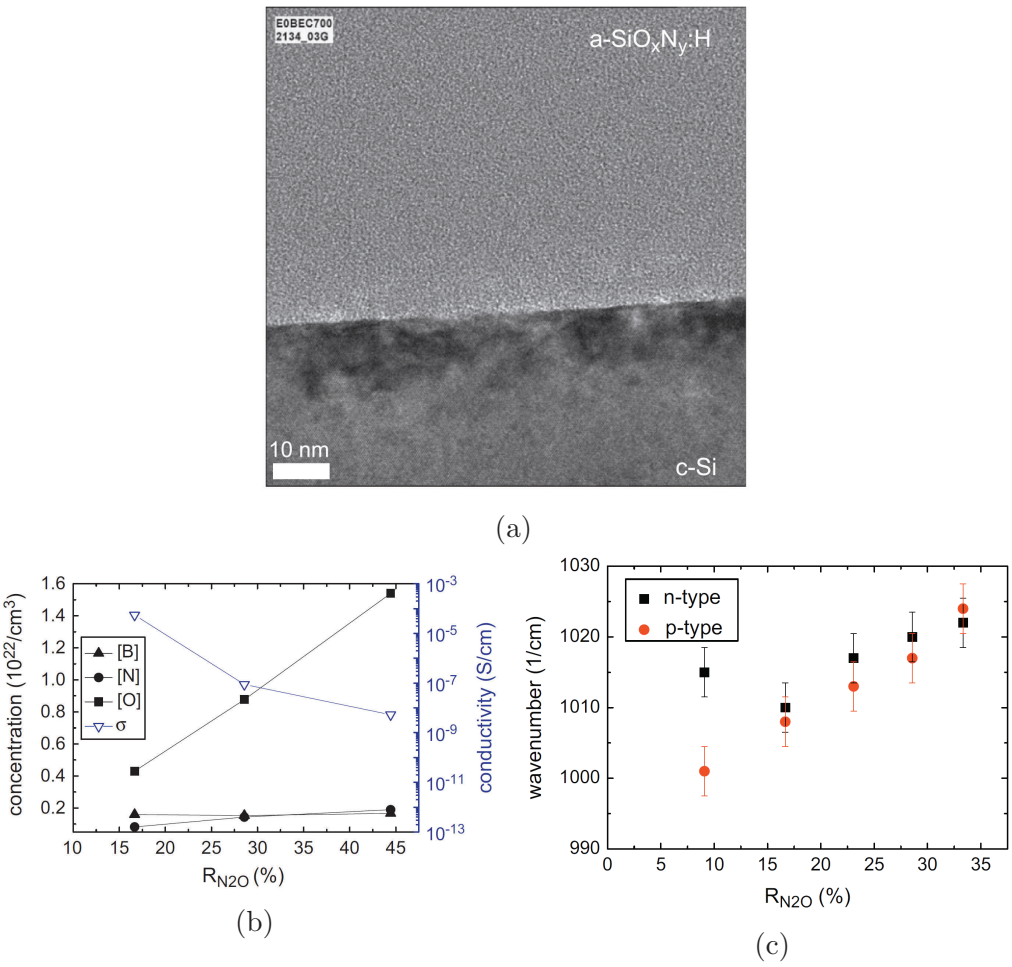

Figure 2.4: a) HR-TEM picture of an a-SiO_xN_y layer [12]. b) Conductivity and SIMS results for B doped a-SiO_xN_y layers [12]. c) Si-O-Si bond frequency for a-SiO_xN_y layers [12].

Si-O-Si bonds in the layers [45, 46].

2.3 Experimental methods

The following sections describe the experimental techniques employed to characterize SRC/SiC multilayers and nc-SiO_xN_y thin films. Section 2.3.1 deals with the measurement of the structural and compositional properties of the systems, Sec. 2.3.2 concerns the morphological characterization of the surfaces of the samples, while Sec. 2.3.3 is relative to the analysis of the electrical properties of the layers both at the nano-scale and at macroscopical level. Section 2.3.4 describes the techniques used for optical characterization.

2.3.1 Structural and compositional analyses

Raman spectroscopy, Fourier Transform InfraRed (FTIR) spectroscopy, High Resolution TEM (HR-TEM) and Energy-Dispersive X-ray spectroscopy (EDX) are performed in order to investigate the structural and compositional properties of the SiO_xN_y thin films. The latter has been used to evaluate the oxygen, nitrogen and silicon distribution within the layers. Both HR-TEM and EDX have been performed on a cross section of the layers deposited on Si and the system used are a JEM-220FS (HR) and a JED-2300 from JEOL.

The crystalline fraction χ of the samples is obtained by Raman spectroscopy on layers deposited on a glass substrate. The system used is from WITec and the laser used has a wavelength of 488 nm. The following expression has been used to evaluate χ:

$$\chi = \frac{I_C}{I_C + I_A} \tag{2.5}$$

where I_A is the integrated area of the peak at 480 cm^{-1} related to the amorphous component and I_C is the integrated area of the peak at 520 cm^{-1} related to the crystalline phase, as depicted in Fig. 2.5. The first peak is modeled as Gaussian, while the latter by a Lorentzian curve in order to perform the fit [13, 47].

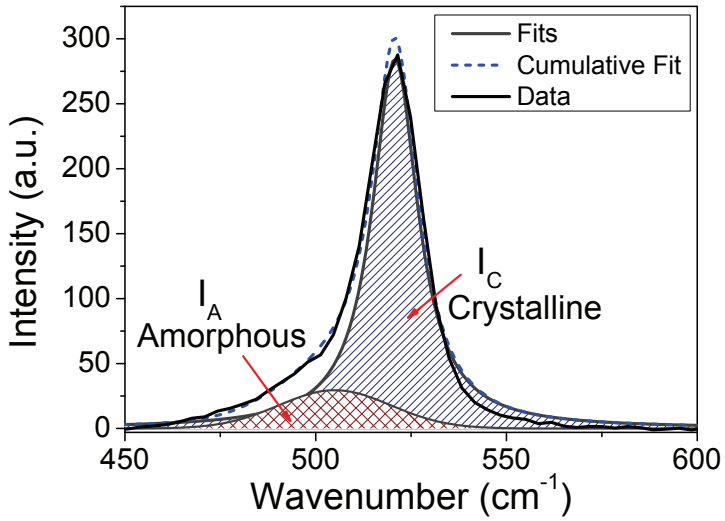

Figure 2.5: Raman spectrum of sample A (R_{N2O}=9.09%, 3h annealed). The fits for amorphous and crystalline components are reported, as well as the cumulative fit (dashed line).

Si-O-Si, Si-H and Si-H_2 bonds within the SiO_xN_y thin films are studied using FTIR spectroscopy using a Vertex 80 system by Bruker. The layers are deposited on a Si substrate only on one side. The measurements are carried out at room temperature in a nitrogen atmosphere, using a resolution in wavenumbers of 5 cm^{-1}. The following expression is used to determine the absorption coefficient [48]:

$$\alpha_{\text{eff}} = \frac{A_{\text{film}}}{d_{\text{film}} \log_{10} e} \tag{2.6}$$

where A_{film} is the absorbance of the nc-SiO_xN_y layers ($A_{\text{film}} = A_{\text{sample}} - A_{\text{substrate}}$) and d_{film} is the thickness of the layers obtained by ellipsometry measurements. The Drude term is accounted for subtracting a baseline correction of the FTIR data. In order to obtain the intensity I of a bond, an integration over the absorption band is needed [49]:

$$I = \int \frac{\alpha_{\text{eff}}(\omega)}{\omega} \mathrm{d}\omega. \tag{2.7}$$

The intensity obtained is proportional to the total bond density [49]. The

concentration of hydrogen N_H within the as-deposited layers has been evaluated from the intensities of the Si-H (I_{2000}) and Si-H_2 (I_{2100}) bonds using the following expression [49]:

$$N_H = A_{2000} I_{2000} + A_{2100} I_{2100} \tag{2.8}$$

where $A_{2000} = (9.0 \pm 1.0)\text{cm}^{-2}$ and $A_{2100} = (2.2 \pm 0.2)\text{cm}^{-2}$ are calibration factors for the Si-H and Si-H_2 bonds, respectively [49].

2.3.2 Surface morphology

The morphology of the SiO_xN_y thin films and the SRC/SiC ML has been investigated using Atomic Force Microscopy (AFM). The system used is a NT-MDT Solver P47H Pro in tapping mode with ultra-sharp tips (NT-MDT NSC10_DLC) with curvature radius less than 3 nm.

Tapping mode imaging employs an oscillating probe to investigate the surfaces. The tip is placed a few nanometers above the surface and it is mechanically excited at its resonance frequency ω_0 [50]. The motion of the free probe is described by the following equation:

$$z = z_0 + A_0 \cos(\omega_0 t - \phi) \tag{2.9}$$

where z is the vertical position of the probe with respect to the position z_0 of the non-oscillating probe, A_0 is the amplitude of the tip far from the sample surface and ϕ represents the phase of the oscillating motion and it is set at 90° for the free oscillating tip (i.e. far from the sample surface. When the tip approaches the sample, the tip-sample interaction leads to a reduction of the amplitude of the oscillation, which is then indicated by A. The normalized amplitude A/A_0 is kept constant during tapping mode imaging by a feedback system to measure the topography of the surface under investigation [50].

Phase contrast maps convey information about the energy dissipated during the scanning process and they have been obtained keeping the tip-sample interaction always in the same regime (attractive or repulsive) in order to avoid switches during the measurement [51, 52]. Figure 2.6 depicts the

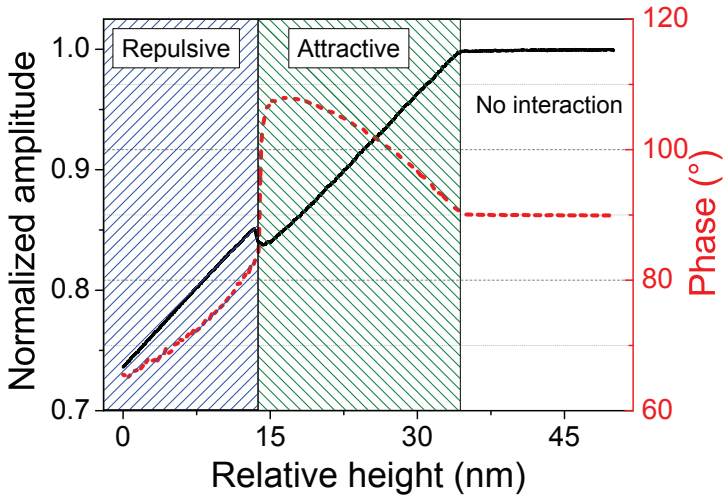

Figure 2.6: Normalized amplitude (black) and phase (red) as measured with NT-MDT Solver Pro 4 on sample X9-4. On the x-axis the relative tip-sample height is reported, where zero corresponds to the actual set point. The region of attractive and repulsive regime of interaction between the tip and the surface are highlighted.

recorded normalized amplitude A/A_0 and phase ϕ of the oscillating tip as a function of tip-sample relative height. The regions of attractive and repulsive regime of interaction are highlighted. The set point is chosen in order to keep the interaction between the tip and the sample repulsive over the whole image, and consequently all the phases recorded are less than 90° [43].

In these experimental conditions the phase lag between free and damped oscillation of the tip is proportional to the energy dissipated between the tip and the layer surface [50, 53]:

$$\sin\phi \propto E_{\text{diss}}. \tag{2.10}$$

Energy dissipation variation can be related to changes in the amorphous/crystalline phase, to compositional variations (such as the silicon content in different areas of the sample) and to variation in the local strain.

The surface roughness and the lateral correlation length ξ are evaluated from AFM topography maps. The lateral correlation length for mounded surfaces is a measure of the size of the mounds and has been obtained from

the Height-Height Correlation Function (HHCF) and the Watershed method.

The HHCF can be calculated from AFM topography maps with the image-analysis software *Gwyddion* as [54, 55]:

$$HHCF(r) = \frac{1}{N(M-m)} \sum_{l=1}^{N} \sum_{n=1}^{M-m} \left(z_{n+m,l} - z_{n,l}\right)^2 \tag{2.11a}$$

$$m = \frac{r}{\Delta x} \tag{2.11b}$$

where N and M are the dimensions in pixels of the map, z is the recorded height for each point of the map and Δx is the sampling interval of the AFM measurement.

The self-affine model has been used to describe the surfaces of the SiO_xN_y samples. Within this framework, a surface profile $z(x)$ follows the equation:

$$|z(x+r) - z(x)| \sim (mr)^{\alpha} \tag{2.12}$$

where α is called roughness exponent, while m denotes the local slope of the surface profile [55]. It is also valid that:

$$|z(\epsilon x + \epsilon r) - z(\epsilon x)| \sim (\epsilon m r)^{\alpha} \tag{2.13}$$

which can be rearranged in the following form:

$$|\epsilon^{-\alpha} z(\epsilon x + \epsilon r) - \epsilon^{-\alpha} z(\epsilon x)| \sim (mr)^{\alpha} \tag{2.14}$$

and compared with Eq. 2.12. It results that the profile could be expressed in the form:

$$z(x) \sim \epsilon^{-\alpha} z(\epsilon x) \tag{2.15}$$

and the profile is called self-affine [55]. The exponent α describes the short range roughness of a self-affine surface, as it is depicted in Fig. 2.7.

The HHCF obtained for an AFM map can be fitted in the hypothesis of

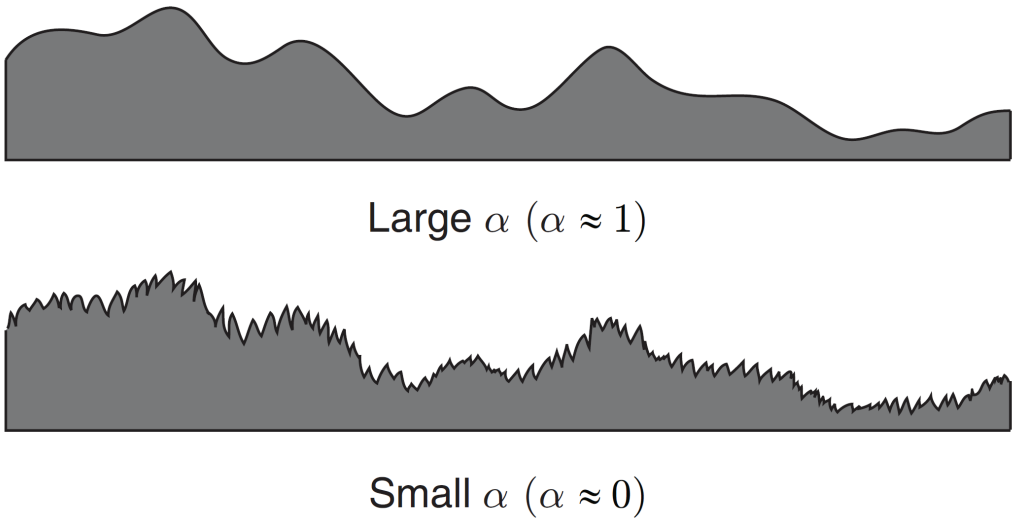

Figure 2.7: Local surface morphology for surfaces with different values of α. Smaller values indicate rougher local surfaces and $0 < \alpha < 1$ [55].

self-affine surfaces through:

$$HHCF(r) = 2R^2_{\mathrm{HHCF}} \left[1 - \exp \left[- \left(\frac{r}{\xi} \right)^{2\alpha} \right] \right] \tag{2.16}$$

where R_{HHCF} represents the surface roughness, α is the roughness exponent and ξ is the lateral correlation length, the quantity under investigation [55, 56].

The effect of finite sampling on the HHCF is to produce an oscillatory behavior for $r >> \xi$, as depicted in Fig. 2.8a, where the HHCF evaluated for a single simulated map of a self-affine surfaceis shown [56]. When several maps are acquired (or, in this case, simulated), the average of the obtained HHCF shows a reduced oscillatory behavior, as shown in Fig. 2.8b (thick line) [56]. Acquiring several AFM maps is equivalent to bigger sampling, with the advantage of maintaining high resolution on the single map.

The roughness obtained from the fitting of the HHCF can be compared with the root mean square roughness R_{rms}. The latter can be evaluated from an AFM as the root mean square of the height distribution. Figure 2.9 shows an example of height distribution of an AFM map acquired in tapping mode

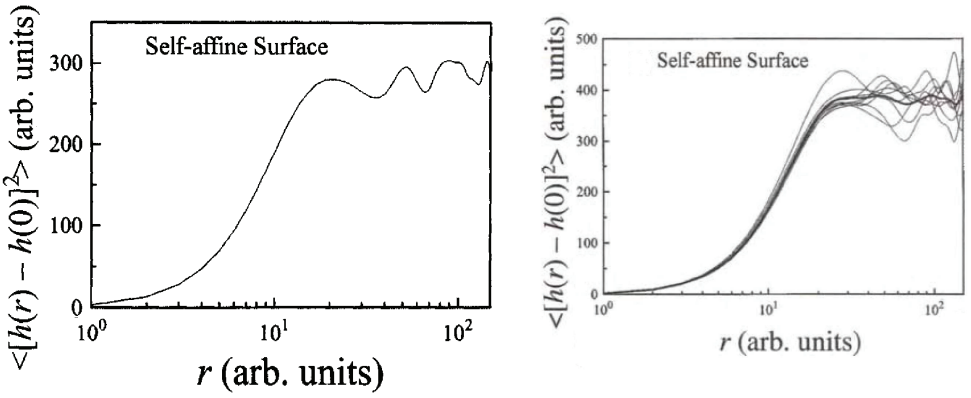

(a) (b)

Figure 2.8: Height-Height correlation function for a self affine simulated surface, single image sampling (a) and averaged over ten images (thick line) (b). The thin curves in (b) represent the HHCF of the individual images. Adapted from [56].

of sample B, 3 h annealed, with R_{rms} =1.51 nm. In order to reduce the effects of the noise over the fast scanning line, R_{rms} can be calculated row/column wise and its average R_q over the map is an estimation of the roughness of the surface [54].

The Watershed method is implemented by the software *Gwyddion* and it is used for marking and segmentation of the grains. The algorithm works on the inverted surface and local minima are searched. Virtual water drops are placed on the surface and they minimize their potential energy looking for a local minimum. After the grains are marked, the segmentation step fills the grains and sets the grain boundaries [54]. A mask superimposed to the original AFM topography map is produced by the software and statistical information about the grains are available.

2.3.3 Electrical characterization at nano-scale and macro-scale

Conductive AFM (c-AFM) measurements allow to investigate the conductivity at the nanoscale [57]. The SRC/SiC ML have been measured using a NT-MDT Solver P47H Pro system and a conductive Pt coated tip, with

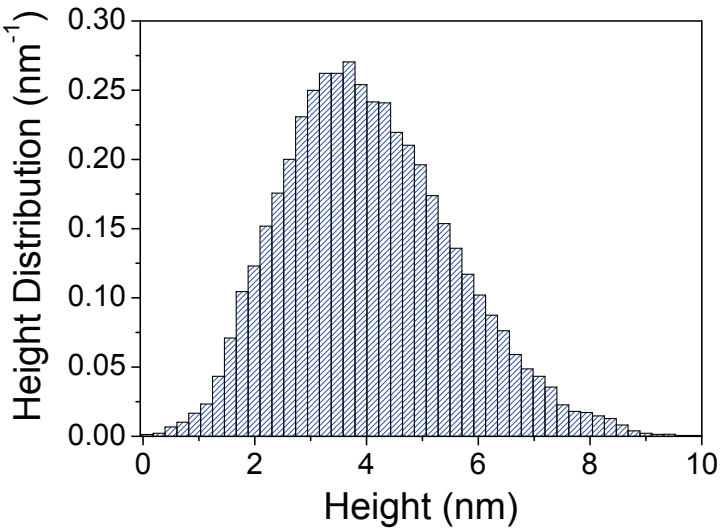

Figure 2.9: Height distribution of an AFM map acquired in tapping mode of sample B, 3 h annealed. The root mean square of this distribution is an estimation of the surface roughness R_{rms}.

nominal radius of curvature of 35 nm (NT-MDT CSG10/Pt) [43]. The measurements on SiO_xN_y thin films were performed using a Park NX10 system with a Pt coated probe (RMN 25Pt300B), with tip radius less than 20 nm. A conductive probe is put in contact with the layer surface and the current flowing between the tip and the sample is recorded in each point of the map for a fixed bias applied of 2 V (SRC/SiC systems) or 0.8 V (SiO_xN_y thin films). Figure 2.10 depicts a schematic view of the c-AFM set-up. Morphology and current maps are acquired simultaneously and profiles of both maps are analyzed in order to exclude artifacts related to the topography. It is possible to observe an increased current due to an increase of the contact area between the tip and the surface. This fact can be observed especially when the tip enters a dip during the scanning. If an absence of correlation between height and current profiles is observed, such kind of artifacts can be excluded.

Local current-voltage measurements can be performed using the AFM. The first electrical contact is made on the surface of the sample, while the second one is made by the conducting AFM tip in contact with the surface. A variable bias is applied to the system and the current flowing between the

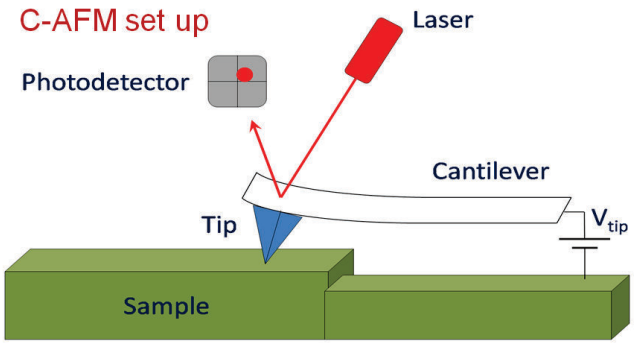

Figure 2.10: Schematic view of the c-AFM set up (not in scale).

tip and the sample is recorded.

Temperature dependent IV measurements are performed between 300 K and 373 K for the SRC/SiC ML and between 150 K and 300 K for the nc-SiO_xN_y layers in order to extract the activation energy E_a and the pre-exponential factor σ_0, which both could give information about the conduction mechanisms. The experimental data were fitted using the following expression:

$$\sigma = \sigma_0 \exp\left(-\frac{E_a}{kT}\right) \tag{2.17}$$

where T represents the temperature and k the Boltzmann constant [58, 59]. Typically, disordered systems show an exponential relationship between σ_0 and the activation energy, known as the Meyer-Neldel Rule (MNR) or the compensation law [58], expressed as:

$$\sigma_0 = \sigma_{00} \exp\left(\frac{E_a}{E_{MN}}\right) \tag{2.18}$$

with E_{MN} and σ_{00} MNR constants which are typical signature of a system [43].

2.3.4 Optical spectroscopy

Reflection and Transmission (R&T) spectra of the SRC/SiC ML were acquired in the UV-vis range by an Avantes fiber optics spectrophotometer and fitted by the software *Optical* [60]. The model implemented by this software is based on a generalized matrix method to treat multilayer systems composed of materials with coherent and incoherent optical behavior and the light energy flux inside the multilayer is computed. Internal light absorption is then derived [60]. The software allows to simulate R&T spectra of films deposited on glass and to fit the experimental spectra to obtain the extinction coefficient of the film (k) when the real part of the refractive index (n) is given as an input. The refractive index is given by $N = n + ik$. The software looks for the k values for which the following equation is satisfied:

$$\frac{T_e}{1 - R_e} = \frac{T_s}{1 - R_s} \tag{2.19}$$

where T_e and R_e are the measured R&T spectra, while T_s and R_s are the simulated spectra [60]. The absorption coefficient can be determined using the expression [61]:

$$\alpha = \frac{4\pi k}{\lambda} \tag{2.20}$$

The software *Optical* also allows the simulation of mixed layers once the optical constants of the constituting materials are known.

The simulations performed on the SRC/SiC ML spectra use the refractive index spectra of SiC and a-Si as determined by fitting [62] and the reference single SiC and a-Si layers, whereas the optical function of Si NCs were approximated using the literature function of continuous nc-Si [63].

The absorption coefficient and the Tauc gap of the SiO_xN_y thin films are obtained from R&T spectra measured by a Cary spectrometer from Varian. The layers have been deposited on glass. The spectra are taken in the range 300-1500 nm and the absorption coefficient has been deduced using the expression [64]:

$$\alpha(h\nu) = \frac{1}{d} \ln \left(\frac{1 - R(h\nu)}{T(h\nu)} \right) \tag{2.21}$$

where $T(h\nu)$ and $R(h\nu)$ are the measured transmission and reflection spectra, while d is the thickness of the layer obtained from ellipsometry measurements. Thin film interference fringes appears in the region of medium absorption, whose contribution for the determination of α could be reduced using Eq. 2.21 [65]. A fit in the high absorption region of $(\alpha h\nu)^{1/2}$ has been performed in order to obtain the Tauc gap E_T values following the relation:

$$(\alpha \cdot h\nu)^{1/2} \propto (h\nu - E_T) \tag{2.22}$$

in the hypothesis of indirect band gap and disordered material [66].

Chapter 3

Results: SRC/SiC multilayers

The following sections report the experimental results obtained on SRC/SiC multilayer (ML) systems for photovoltaic applications. Section 3.1 deals with the optical properties of the ML, Sec. 3.2 reports the results on the morphology measured with the Atomic Force Microscopy (AFM), the electrical properties at the nanoscale are described in Sec. 3.3 and the results on the conductivity of the multilayers are reported in Sec. 3.4.

3.1 Optical properties

The presence of silicon nanocrystals (NCs) within the multilayers deeply affects their properties. The question of which is their role in the optical properties of the ML has been addressed using Reflection and Transmission (R&T) measurements.

Previous studies on these systems clarified the structure of the annealed ML, evidencing the formation of Si NCs surrounded by an amorphous tissue [40, 67], as reported in Sec. 2.3. The SiC matrix shows a 63% crystallized fraction in form of 3C-SiC NCs of about 3 nm diameter. Some details relative to the analyzed samples can be found in Tab. 2.1 and Sec. 2.1. R&T spectra has been fitted using the software *Optical* and the Bruggeman Effective Medium Approximation (EMA) [68] in order to obtain quantitative information on the nc-Si, a-Si and SiC relative volumes, provided that the

optical functions (n, k) of the components are known [43].

An example of simulation for sample X9-4 (d_{SRC}=4 nm) deposited on quartz is reported in Fig. 3.1a, while nominal R&T spectra expected for varying SiC/a-Si/nc-Si composition are reported in Fig. 3.1b. The measured R&T spectra for sample X9-4 are also reported in Fig. 3.1a. The spectra can be qualitatively interpreted by distinguishing three regions: region A (high absorption, T=0), region B (low absorption, T$\neq$0, R+T$<$ 100%), and region C (transparency: R+T= 100%), as reported in Fig. 3.1a. In regions B and C, the interference of light reflected at the surface and at the interface with the substrate gives rise to an oscillating pattern.

In region C, the fringe contrast is determined by the refractive index contrast between multilayer and substrate. Such peculiarity allows to determine the SiC-to-Si ratio. This is also illustrated in Fig. 3.1b (right), where the crystallized fraction χ_c is fixed and the SiC-to-Si ratio is varied. χ_c is defined as the ratio between the nanocrystallized-to-total Si volume. The figure shows that the fringe contrast increases with decreasing SiC volume fraction, as a consequence of the lower refractive index of the mixture. The determination is basically independent of χ_c, due to the similarity of the refractive index of a-Si and nc-Si, as shown in the inset of Fig. 3.1b.

In region B, the fringe contrast is damped by absorption in the multilayer, and the onset of transmittance suffers a blue shift for increasing χ_c because of the higher absorption of a-Si with respect to nc-Si. The occurrence is illustrated in Fig. 3.1b (left). In this figure, the SiC-to-Si volume ratio is kept constant while χ_c is varied. Once the SiC-to-Si ratio is determined, χ_c is therefore univocally determined by the onset of T. The inset of Fig. 3.1b shows the absorption coefficient of the involved materials. Volume and crystalline fractions of the multilayers have been evaluated with this approach and they are reported in Tab. 3.1.

3.2 Morphological analyses with AFM

Figure 3.2a shows the surface topography of sample X9-2 measured by AFM in tapping mode. At the same time also the phase contrast image,

Sample name	V_{SiC} (%)	V_{Si} (%)	χ_c (%)	E_a (eV)	σ_0 (S/cm)	σ_d (S/cm)
X9-2	75	25	20	0.20	$1.74 \cdot 10^{-2}$	$8.03 \cdot 10^{-6}$
X9-3	72	28	47.5	0.21	$4.74 \cdot 10^{-2}$	$1.21 \cdot 10^{-5}$
X9-4	58	42	57	0.24	$1.6 \cdot 10^{-1}$	$1.38 \cdot 10^{-5}$
nc-SiC	100	0	-	0.19	$3.27 \cdot 10^{-4}$	$2.19 \cdot 10^{-7}$
nc-Si [40]	0	100	100	0.38	85	$3.53 \cdot 10^{-5}$
a-Si [40]	0	100	0	0.16	$9.00 \cdot 10^{-4}$	$1.78 \cdot 10^{-6}$

Table 3.1: SiC and Si (amorphous and crystalline) volumes and crystallized silicon fractions extracted by fitting of the R&T spectra. Activation energies (E_a), σ_0 and dark conductivity (σ_d) of the samples with d_{SRC} equal to 2, 3 and 4 nm and the reference SiC and Si layers. [43].

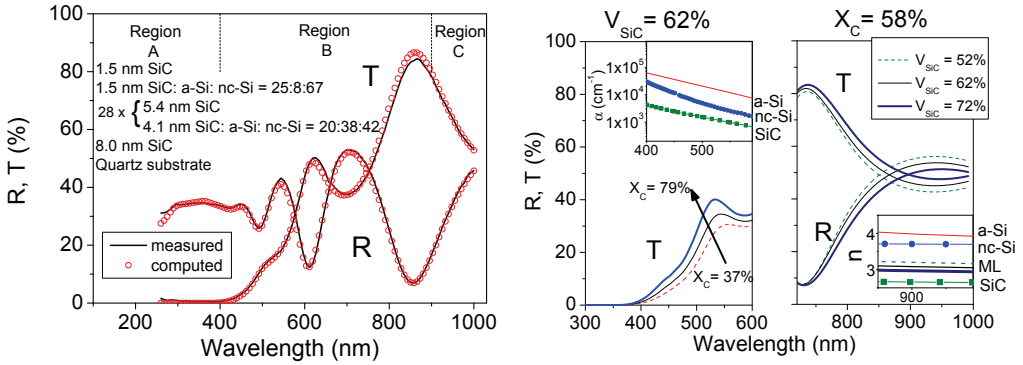

(a) (b)

Figure 3.1: (a) Measured (lines) and simulated (symbols) R&T spectra of sample X9-4 with d_{SRC}=4 nm. The simulation is obtained using the complete ML structure including surface and buffer layers as indicated in the figure. (b) Computed spectra of 220 nm film/quartz, for different SiC/a-Si/nc-Si compositions of the film. On the left: SiC=62%; χ_c=37-79%. On the right: χ_c=56%; SiC=52-72%. χ_c represents the crystallized fraction [43].

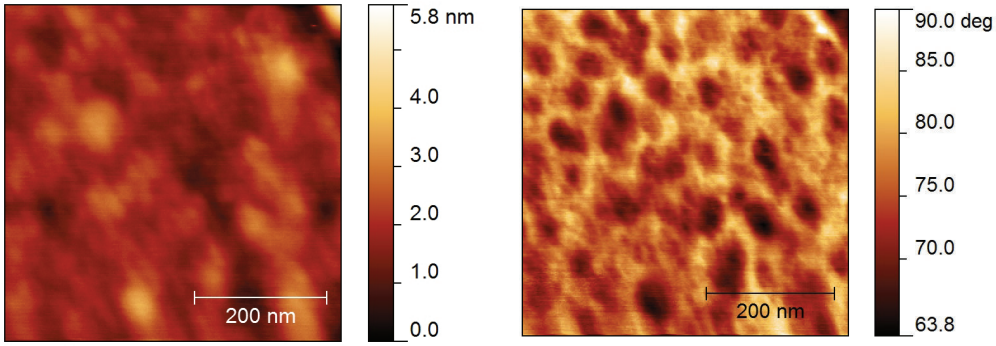

(a) (b)

Figure 3.2: Tapping mode AFM performed on sample X9-2 with d_{SRC}=2 nm: (a) topography and (b) phase contrast maps [43]. The maps have been acquired in repulsive regime.

which represents the difference in phase with respect to the free oscillation, is recorded and the results are shown in Fig. 3.2b. Phase contrast maps have been obtained keeping the tip-sample interaction always in the same regime (attractive or repulsive) in order to avoid switches during the measurement [51, 69]. The set point is therefore chosen in order to keep the interaction between the tip and the sample repulsive over the whole image, and consequently all the phases recorded are less than 90°. Energy dissipation variation can be related to changes in the amorphous/ crystalline phase, and/or to compositional variation, i.e. to the silicon content in different areas of the sample, and/or to variation in the local strain [50]. In the present map the phase contrast variation could be related to compositional and phase inhomogeneities, as Si and SiC crystalline phase coexist with amorphous Si and SiC, as shown from the volume and crystal fraction values reported in Tab. 3.1.

The features visible in the topography and phase contrast maps of Fig. 3.2 are larger than the Si or SiC NCs, which have diameters ranging from 3 to 5 nm, as observed by TEM [40], indicating either the presence of NC clusters, or a consequence of the AFM maps revealing features related to the tip-sample convolution. The same effect can be seen in maps acquired in attractive regime, as shown in Fig. 3.3. Figures 3.3a and 3.3b show the

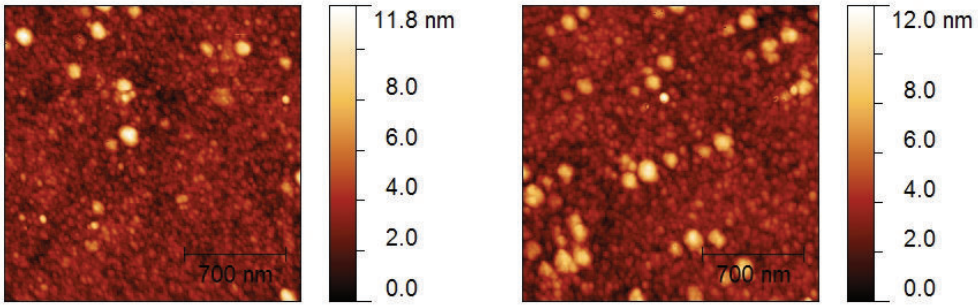

(a) (b)

Figure 3.3: Tapping mode AFM images of sample X9-2 (d_{SRC}=2 nm) (a) and X9-4 (d_{SRC}) (b). The maps have been acquired in attractive regime.

surface morphology measured by AFM in attractive regime for samples X9-2 and X9-4, respectively. Data acquisition in attractive regime allows reduced tip damage and resolved maps can be obtained. The maps reveal the presence of grains of different dimensions and more large aggregates are visible in Fig. 3.3b. These features can be related either to the presence of NC clusters or to the etching procedure described in Sec. 2.1. The attractive regime maps have been used to evaluate the RMS roughness of the surfaces, which varies between 1.2 and 1.4 nm for 1x1 μm^2 maps.

3.3 Conductivity at the nanoscale: c-AFM

The local conductivity of the layers is measured by c-AFM to identify the current paths at the nano-scale. Figure 3.4 shows 1x1 μm^2 c-AFM maps of multilayers. The bias applied to the tip is +2 V and the current ranges between 0 and 60 pA for sample X9-2 (Fig. 3.4b). Conductivity variations can be noted and the darker areas correspond to lower conductivity. Figure. 3.5a shows topography and current profiles taken over the same scanning line. As no direct correlation between topography and current profiles was observed, morphology related artifacts can be excluded. A similar behavior is observed for samples with 3 and 4 nm SRC layer thickness and the current measured at the same bias is in the range 0-68 pA for sample X9-3 (Fig. 3.4d) and 0-

103 pA for sample X9-4 (Fig. 3.4f). Profiles of topography and current over the same scanning line have been taken for these samples as well and they are reported in Fig. 3.5b and 3.5c, respectively. Morphology related artifacts can be excluded in these cases too. Artifacts relative to sample oxidation, memory effects and tip damage can be excluded due to the carefully chosen experimental conditions [70, 71].

The increase of d_{SRC} results in a higher crystalline fraction (see Tab. 3.1), that determines an increased conductivity. The current maps show cluster and dot-like features with diameters between 50-100 nm with different conductivities (Fig. 3.4). These features can be related to clusters formed by Si or SiC nano-crystals, as cluster formation is observed in [40]. This map presents a pronounced difference with respect to the case of nc-Si:H [72–74], where in the intrinsic layers all the Si NCs clusters showed similar conductivities, but different from the matrix one. In the present case the different conductivity of clusters can be related to compositional variation (Si or SiC content), and/or to unintentional doping by contamination with N and O. In particular, some of the clusters show a conductivity lower, others higher than the matrix. As for increasing Si content the conductivity increases, it can be assumed that conductive clusters are associated to Si rich NCs. In such a complex system it is unlikely that the current could flow across the clusters, which show very different conductivity levels, while it can be figured out that the current flows mainly through the cluster boundaries or through the disordered tissue surrounding the clusters.

3.4 Conductivity measurements

Current-voltage characteristics have been measured locally with the AFM in contact mode. Figure 3.6a shows the obtained results, where each curve is the average of 10 measurements taken in different positions on the sample surface. The IV curves show a defined trend: at the same bias the current increases with increasing d_{SRC}. It is possible to compare this result with the lateral conductivities measured with the deposited Ni contacts that are shown in Fig. 3.6b. The conductivity increases from $8.03 \cdot 10^{-6}$ S/cm to

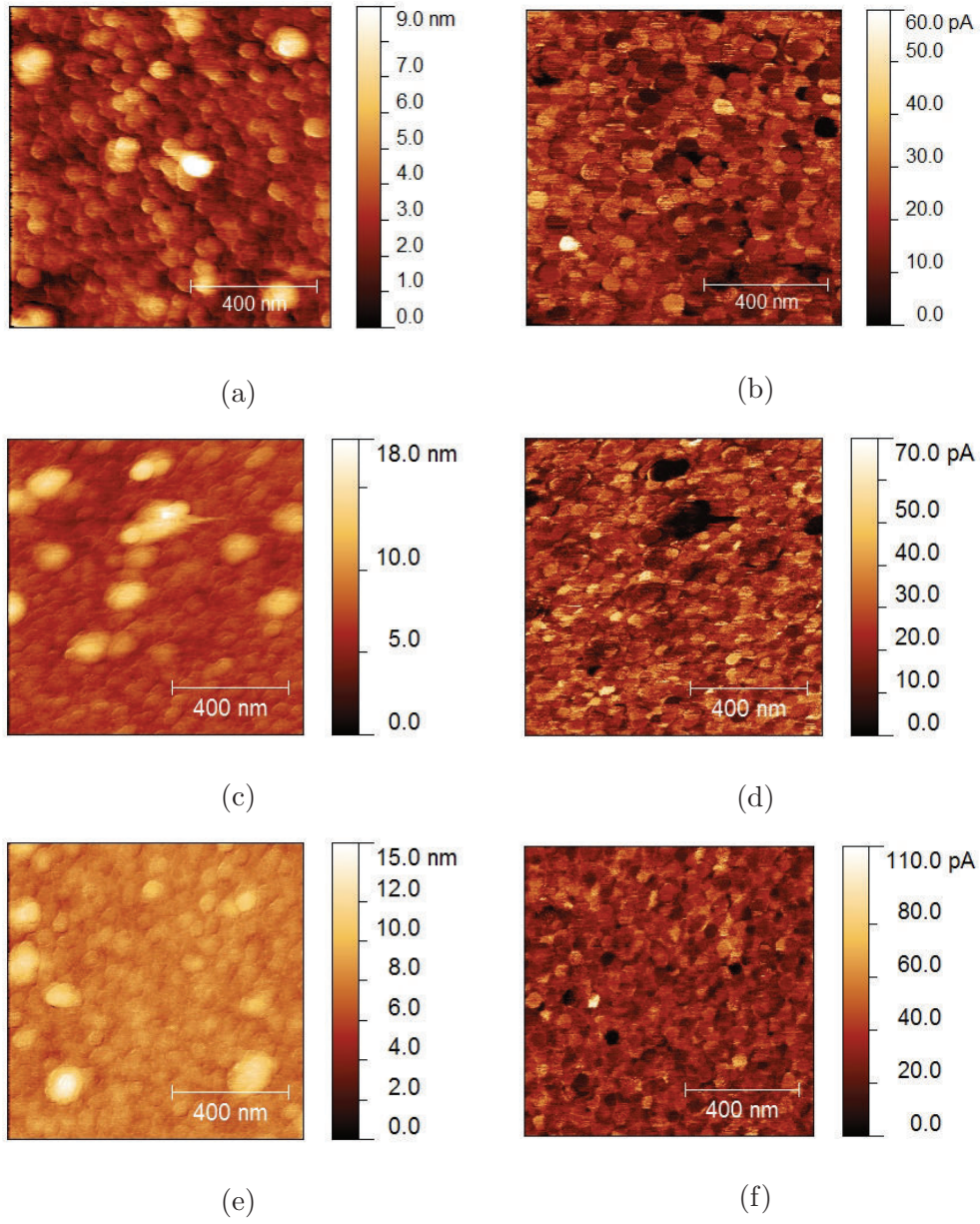

Figure 3.4: C-AFM performed on the SRC/SiC ML: (a) topography and (b) current maps of sample X9-2, (c) topography and (d) current maps of sample X9-3, (e) topography and (e) current maps of sample X9-4 for a bias voltage of 2 V applied to the AFM tip. (a) and (b) adapted from [43].

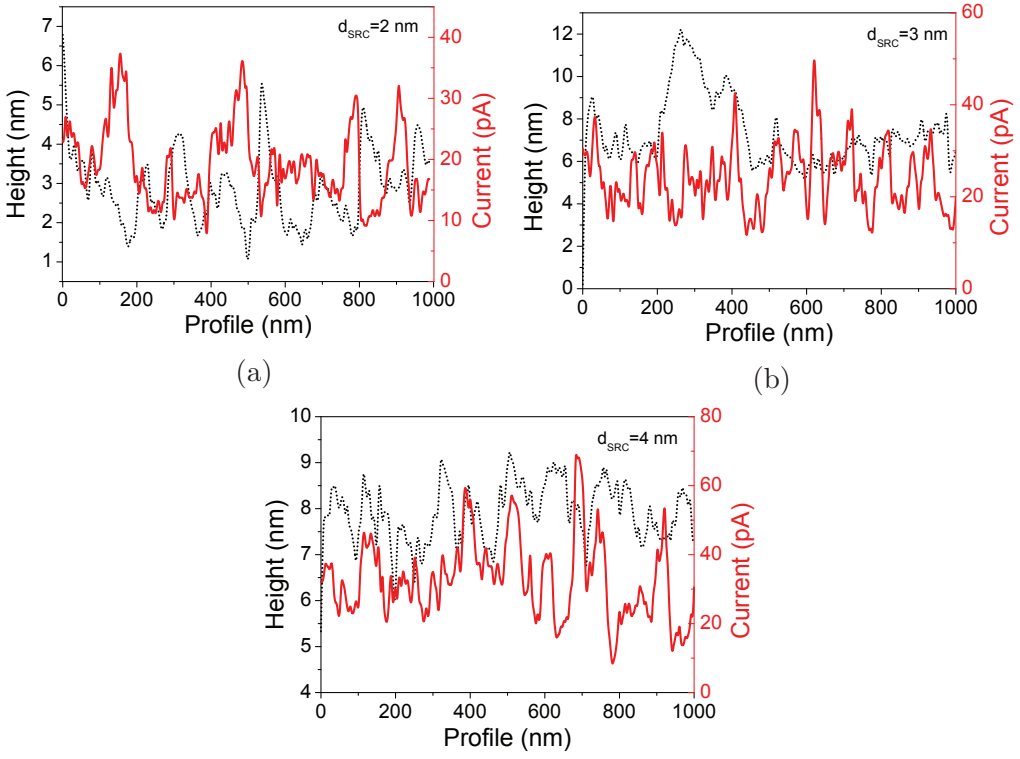

Figure 3.5: Height and current profiles of samples X9-2 (a), X9-3 (b) and X9-4 (c).

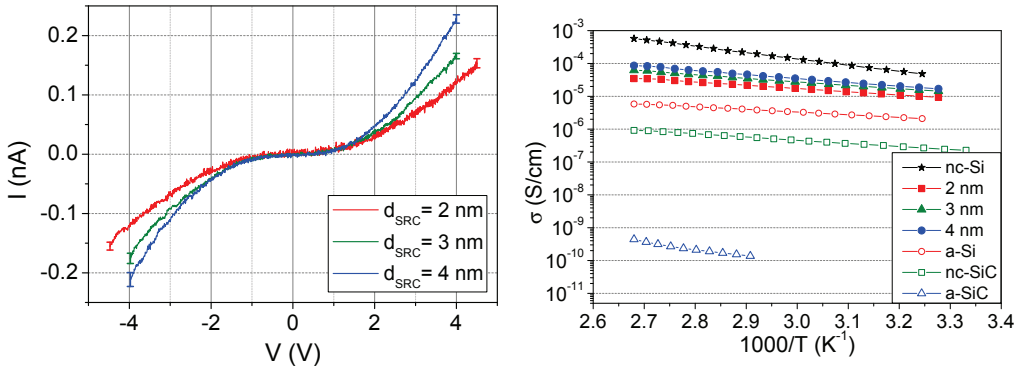

(a) (b)

Figure 3.6: (a) Local IV measured with AFM and (b) macroscopical conductivity measured as a function of temperature [43]. Reference data for nc-Si, a-Si, nc-SiC and a-SiC are reported [40].

$1.38 \cdot 10^{-5}$ S/cm with increasing d_{SRC} (2-4 nm), showing the same trend of the local measurements. Figure 3.6b shows measured conductivity values plotted as a function of inverse temperature for the SiC/SRC multilayers. For comparison, conductivity is also plotted for reference samples a-Si, a-SiC, nc-Si and nc-SiC. It is worth noting that the conductivity of the layer increases when the SRC layer thickness increases and the conductivity values are higher than a-Si, a-SiC and nc-SiC, but lower than nc-Si. All plots show thermally activated process that can be fitted by Eq. 2.17. The results obtained for E_a, σ_0 as well as the measured dark conductivity at room temperature σ_d are reported in Tab. 3.1.

Figure 3.7 shows the conductivity prefactor σ_0 as a function of the activation energy E_a. The data from [75, 76] are also reported for comparison. The data obtained from the SRC (2-4 nm) multilayers follow the Meyer-Neldel rule. MNR exists in many disordered systems as a-Si:H, nc-Si:H, nc-Si:H [76] and porous Si [75]. While the MNR *per se* does not allow to establish the conduction mechanism, the comparison of the MNR parameters with literature data can be useful to propose some hypothesis on the conduction. The authors of [75] showed that many data points of different groups mix around two distinct lines, replotted in Fig. 3.7, and attributed this behavior to the existence of two different transport mechanisms: the upper lines represent

extended-states transport and the lower line represents intercrystallite hopping transport. It is worth noting that our data points lie between the two lines, but for increasing d_{SRC} they move towards the upper line. The following picture can be figured out: for increasing d_{SRC} the layer structure changes. As shown in [40], the SiC/SRC multilayer survives after annealing only for d_{SRC} larger than or equal to 3 nm. For d_{SRC} lower than 3 nm the NCs form, but they are randomly dispersed in the matrix. For d_{SRC} >3 nm the multilayer structure is maintained after annealing and the related TEM image (Fig. 2.2 in Sec. 2.1) clearly shows the presence of NCs [40]. Boundaries between layers and dots, interfaces, disordered tissue are also present in this structure. The conduction mechanism across this multilayer likely occurs via extended states, as can be noted from the comparison between our data and upper line in Fig. 3.7.

This picture is also confirmed by the conductive AFM results shown in Fig. 3.4, where the clusters show different conductivity values. Hopping mechanisms between those clusters are unlikely, while the most probable conduction path involves intra-grain layers and interfaces.

3.5 Conclusions

The effect of the variation of the SRC layer thickness on the properties of the multilayers has been investigated. The SiC and Si volumes and Si crystalline fraction χ_c have been obtained from the analysis of R&T spectra. An increase of χ_c has been observed for increasing d_{SRC}. This fact leads to an increase of the transmission measured at low wavelengths.

Phase contrast maps acquired with AFM in tapping mode reveal variations in the tip-sample energy dissipation, that is due to either differences in the layer composition and/or changes in the amorphous/crystalline phase. The conductivity at the nano-scale has been measured by c-AFM and clusters with quite different conductivity have been observed. In this system it is unlikely that the current could flow across the clusters, while the disordered tissue surrounding the clusters can be a preferred conduction path.

The increase of d_{SRC} leads to a higher crystalline fraction that is re-

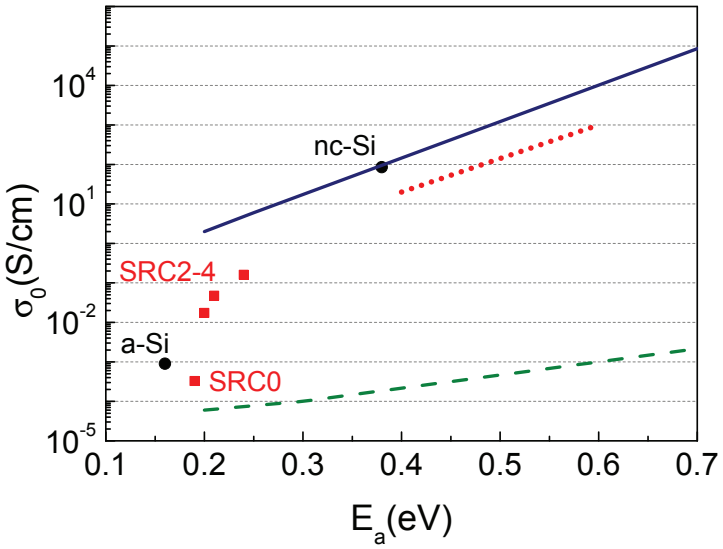

Figure 3.7: MNR parameters σ_0 plotted as a function of E_a for the present samples (squares - multilayers, dots refer to a-Si and nc-Si). Trends from literature data are also reported; the solid line and dashed line are data from [75], the dotted line is from [76]. Both upper lines (solid and dot) represent conduction through band-like states and the lower line (dashed) is related to conduction through hopping [43].

sponsible for an increased conductivity, measured both locally with c-AFM and macroscopically through the deposited Ni contacts. Temperature dependent IV curves have been performed and the results have been fitted using the Meyer-Neldel rule. The data lie between the literature trend for band-like and hopping conduction mechanism. For increasing d_{SRC} the data move towards the trend reported for band-like conduction. As the multilayer structure survives only for $d_{\mathrm{SRC}} > 3$ nm, where boundaries between layers and disordered tissue are present. The conduction mechanism across the ML likely occurs via extended states.

The band-like conduction observed for larger SRC thickness, which is a prerequisite for high mobility transport, is an encouraging feature in view of applications in photovoltaic of the Si NCs/SiC system. The material is expected to combine the needed tunable absorption properties with efficient charge collection and conduction.

Chapter 4

Results: SiO_xN_y thin films

The following sections review the results obtained on SiO_xN_y thin films. Section 4.1 is focused on the structural analyses of the SiO_xN_y layers. The characterization techniques used are HR-TEM, EDX, FTIR and Raman spectroscopy. In Sec. 4.2 the morphology of the layers is studied using the AFM, while Sec. 4.3 and 4.4 deal with conductivity and optical analyses, respectively.

4.1 Structural analyses

4.1.1 SEM and HR-TEM

The SiO_xN_y thin films were deposited by PECVD on both glass and FZ Si substrate. The deposition conditions are summarized in Tab. 2.2. Figure 4.1a shows a Scanning Electron Microscope (SEM) image of the cross section of sample B (R_{N2O}=16.7%) annealed for 3 h. The thickness of the sample is 224 nm. Areas with different contrast are visible and they can be ascribed to the NCs presence in the layers after the annealing process. The question on how the actual formation of crystals works in the SiO_xN_y layers therefore rises [44]. According to HR-TEM measurements (Fig. 4.1b), the crystals form randomly throughout the layer without a preferred crystalline orientation, as it is visible from the orientation of the lattice planes in Fig. 4.1b. The image shows HR-TEM results on the cross section of sample D (R_{N2O}=28.6%), annealed for

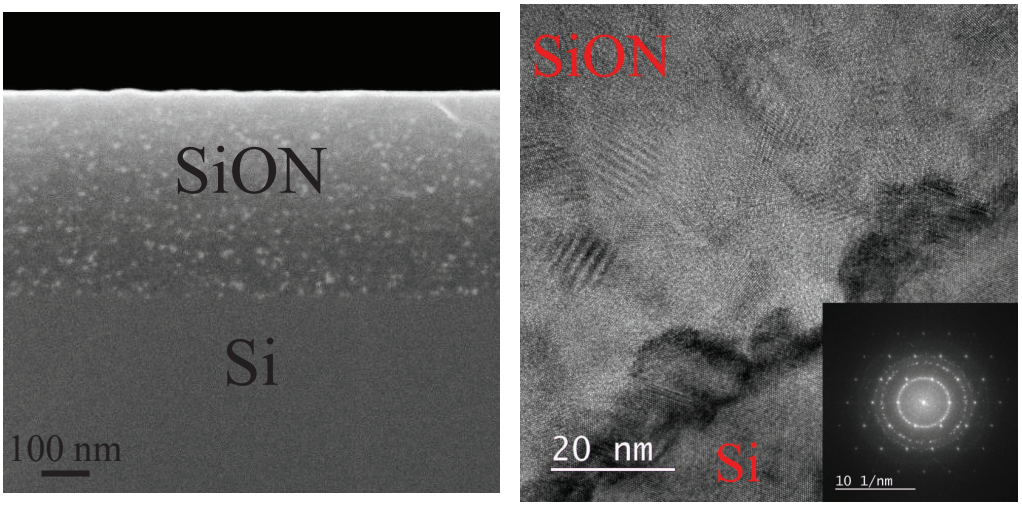

(a) (b)

Figure 4.1: a) SEM picture of sample B (R_{N2O}=16.7%, 3h annealed). b) HR-TEM picture of sample D (R_{N2O}=28.6%, 6 h annealed) [44].

6 h. The measurement has been done in proximity of the interface region between the SiO_xN_y film and the substrate. The inset of Fig. 4.1b depicts the diffraction pattern of the SiO_xN_y layer and the absence of a preferred NC orientation (as it is also visible from the SiO_xN_y region Fig 4.1b) and the presence of on amorphous network is visible thanks to the rings and the diffused halo present in the pattern.

4.1.2 Raman spectroscopy

Raman spectroscopy has been used in order to investigate the dependence of the crystalline fraction χ from the deposition conditions and thermal treatments and it has been obtained by Eq. 2.5. The resulting values of χ are plotted as a function of annealing time and N_2O dilution in Fig. 4.2a and Fig. 4.2b, respectively. χ generally increases as a function of the annealing time and the results relative to the highest and lowest R_{N2O} values are reported in Fig. 4.2a (9.09% for sample A and 47.4% for sample D). On the other hand, the crystalline fraction decreases with increasing R_{N2O} independently of the thermal treatment (Fig. 4.2a). However, even at the

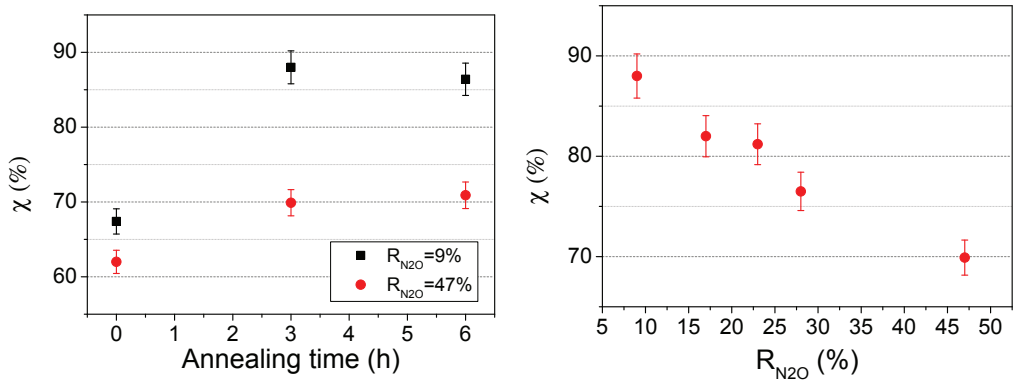

(a) (b)

Figure 4.2: a) Crystalline fraction χ depending on the annealing time for highest (R_{N2O}=47.4%) and lowest (R_{N2O}=9.09%) N_2O dilution. b) Crystalline fraction χ depending on N_2O dilution after 3 h annealing [44].

lowest N_2O concentration (9.09%) only a crystalline fraction of 67% could be reached in the as-deposited (i. e. without annealing) state (Fig. 4.2a), which is a lower value with respect to nanocrystalline silicon (nc-Si) layers, where a crystalline fraction of more than 85% can be reached in the as-deposited state. This result can be understood in view of an increasing disorder due to the incorporation of nitrogen and mainly oxygen within the amorphous network [12]. Generally, the order of the amorphous network can be enhanced by increasing the hydrogen (H_2) dilution during deposition, because monoatomic hydrogen etches weak bonds [77]. The SiO_xN_y films had to be annealed for 3 h at 800 °C in a nitrogen atmosphere in order to reach high crystalline fractions (up to 88%, see Fig. 4.2a) due to technical limitation to the higher H_2 to SiH_4 ratio achievable with the used PECVD system. χ rises during annealing, but saturates for all the N_2O dilutions after 3 h in the oven (Fig. 4.2a). Even in the annealed state crystalline fraction diminishes with ascending N_2O dilution (Fig. 4.2b) due to the increased disorder induced by oxygen. The increase of R_{N2O} accounts for an increased amount of oxygen in the matrix in the as-deposited state, while the nitrogen content remains almost constant as it was showed by SIMS results [12], reported in Sec. 2.2.

4.1.3 FTIR spectroscopy

The bonding structure of the layers has been investigated by FTIR spectroscopy and the results are shown in Fig. 4.3. In particular, the Si-O-Si, Si-H and Si-H_2 bond have been investigated. The frequency of these bonds in Si based materials is known from the literature [49, 78]. In the as-deposited state (squares), the peak position of the Si-O-Si bonding signal shifts linearly with rising N_2O dilution towards higher wavenumbers (Fig. 4.3a). The linearity of this shift for the as-deposited layers reveals a homogeneous distribution of Si-Si and Si-O-Si bonds, as shown in Ref. [45, 46]. In a similar way, the intensity of the Si-O-Si peak increases with rising N_2O dilution (Fig. 4.3b), indicating a higher oxygen incorporation within the layers, as it has been confirmed in previous work by SIMS measurements [12]. Figure 4.3a shows a shift of the peak position towards higher wavenumbers for the layers due to the annealing process (circles and triangles). In this case, the increase of the wavenumber with N_2O dilution becomes a non-linear trend of the wavenumber reaching 1081 cm^{-1}, which is the Si-O-Si peak position of stoichiometric SiO_2 [79]. This effect indicates the occurrence of a phase separation of the annealed layers in Si-rich and O-rich areas [45, 46]. This result is in agreement with what observed with EDX measurement that are presented in Sec 4.1.4. No difference between the 3 h and 6 h annealed sample can be seen with respect to the Si-O-Si peak position.

The intensity of the Si-O-Si bond is proportional to the density of this bond and increases during annealing for all N_2O dilutions as it is depicted in Fig. 4.3b. A difference between the 3 h and 6 h annealed layers is visible for low R_{N2O}, but vanishes with rising R_{N2O} (Fig. 4.3b) and the reason for this behavior is still under investigation.

An additional peak at 1190 cm^{-1} arises during annealing as it is depicted in Fig. 4.3c. The data are relative to sample B (R_{N2O}=16.7%) and the squares represent the Si-O-Si peak measured with FTIR in the as-deposited state, while the circles are relative to the 3h annealed layer. This peak can be attributed to interstitial oxygen [80, 81] and no clear trend of its intensity depending on the N_2O dilution or the annealing time could be

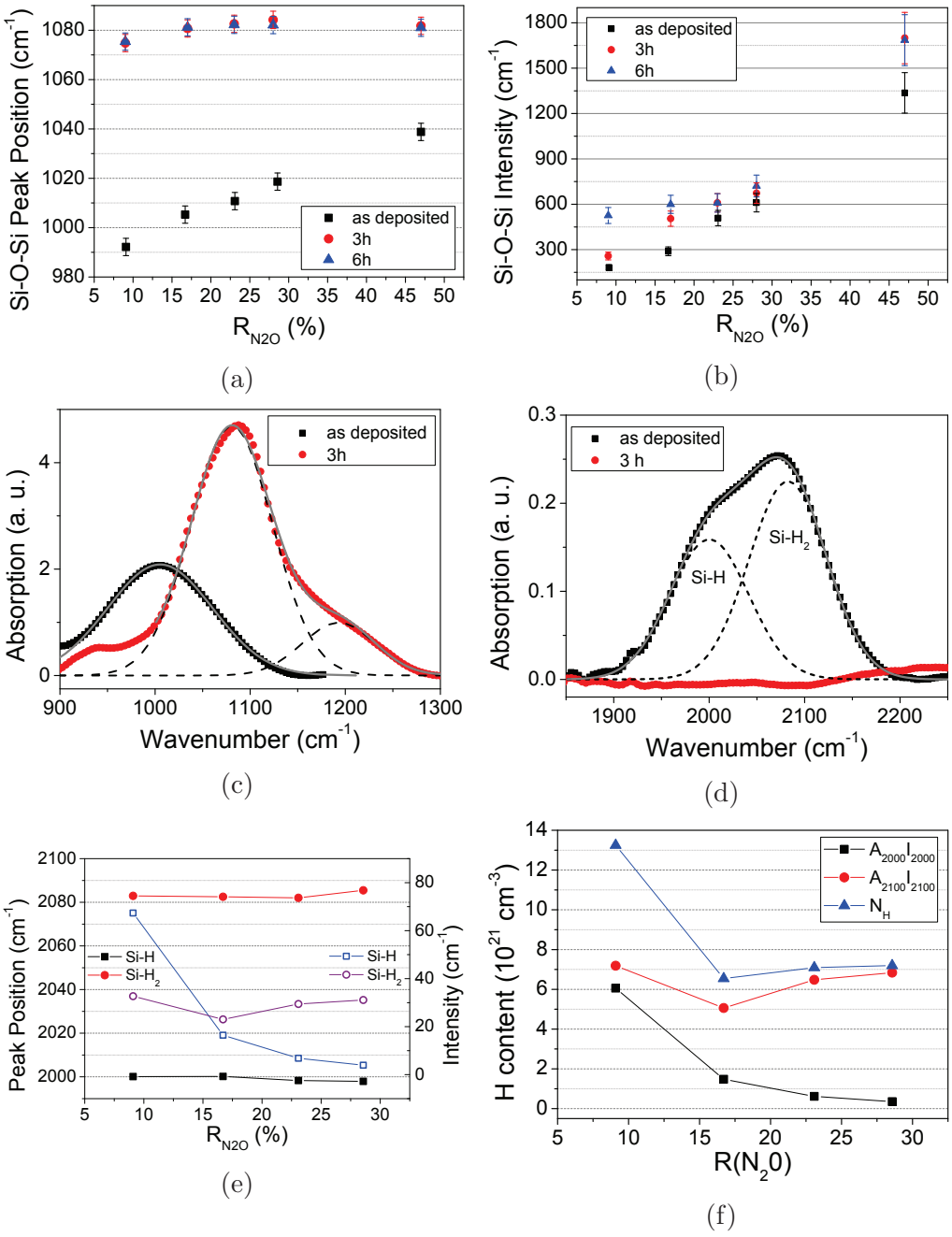

Figure 4.3: FTIR peak position (a) and integrated absorbance (b) for different N_2O dilutions and annealing times; FTIR measurements of sample B (R_{N2O}=16.7%, as-deposited and 3 h annealed state) in the Si-O-Si (c) and Si-H (d) bond region [44]. Squares and circles represent the experimental data, the dashed lines the single peak fits and the solid lines the cumulative fits. e) Si-H and Si-H_2 peak positions (filled markers) and intensities (empty markers). f) H content for different R_{N2O} dilutions.

found. However, as this peak is not observed in any spectrum of the as-deposited layers, this is another hint of annealing induced oxygen relocation, i.e. the formation of O-rich and Si-rich areas.

Figure 4.3d depicts the measured absorbance of sample B (R_{N2O}=16.7%) in the region of Si-H and Si-H_2 bonds. The squares and circles are relative to the measured data in the as-deposited and 3 h annealed state, respectively. The dashed lines represent the single peak fits, while the solid line is the cumulative fit. It is worth noting that Si-H and Si-H_2 bonds can only be observed in the FTIR spectra in the as-deposited state, as hydrogen desorbs due to the long annealing at high temperature as expected [82]. Figure 4.3e shows the peak positions (filled markers) and intensities (empty markers) of Si-H and Si-H_2 bonds as a function of R_{N2O} for the layers in the as-deposited state. The peak positions do not show any significant change with enhanced oxygen incorporation and the same is valid for the Si-H_2 bond intensity, while a decrease of the Si-H bond intensity can be observed. Figure 4.3f shows the H content (N_H) as obtained from Eq. 2.8. A decrease of N_H is observed when R_{N2O} increases from 9.09% to 16.7%, followed by a constant trend of N_H.

4.1.4 EDX results

The relocation of oxygen observed by FTIR spectroscopy has been confirmed by an EDX measurement taken with an HR-TEM. Figure 4.4a depicts the morphology (Fig. 4.4a) and the O, Si and N content (Fig. 4.4b-4.4d) of sample D (R_{N2O}=28.6%), annealed for 6 h. The measurement has been performed on a cross section of the sample. Figure 4.4b clearly reveals a non-homogeneous oxygen distribution within the film, while the Si distribution appears to be homogeneous within the layer (Fig. 4.4c). The distribution of nitrogen is shown in Fig. 4.4d, where some non-homogeneities are visible. It is worth noting that the nitrogen content within the layer after the deposition is lower than the oxygen one ($\sim$ one order of magnitude at this dilution [12]) and that the presence of nitrogen in the substrate area is related to the cross section cutting.

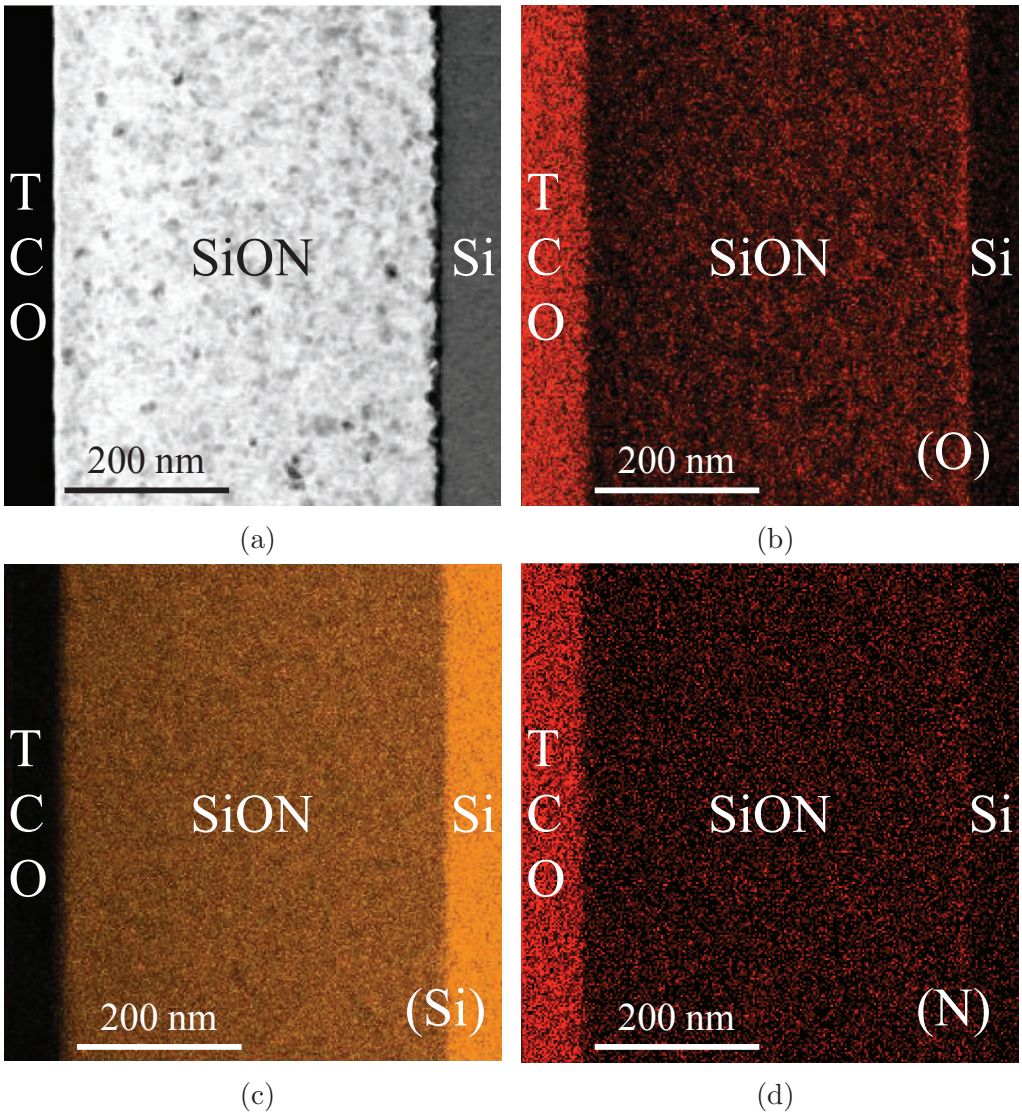

Figure 4.4: HR-TEM measured morphology (a) and EDX measured oxygen (b), silicon (c) and nitrogen (d) content of sample D (R_{N2O}=28.6%, 6 h annealed) [44].

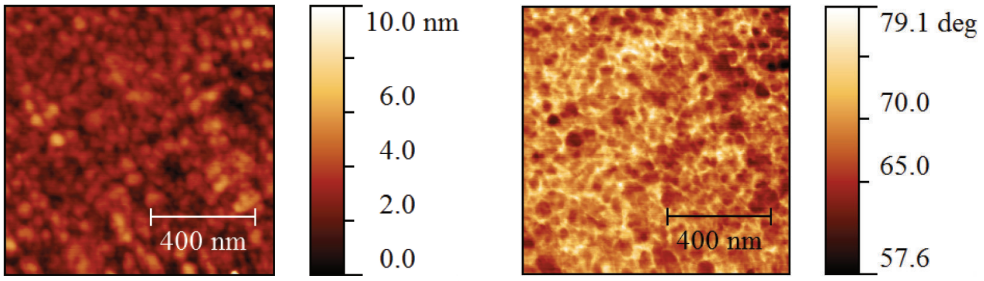

(a) (b)

Figure 4.5: (a) Topography and (b) phase contrast map of sample B, 6 h annealed, (R_{N2O}=16.7%) measured with AFM in tapping mode [44].

4.2 Morphological analyses: AFM

AFM microscopy has been used to measure the topography and the phase contrast of the SiO_xN_y thin films deposited on Si substrate. The measurements have been performed in repulsive mode (i.e. $\varphi < 90°$, see Sec. 2.3.2) and the obtained topography and phase contrast maps for sample B (R_{N2O}=16.7%, 6 h annealed) are reported in Fig. 4.5a and Fig. 4.5b, respectively. Variations in the recorded phase are related to differences in the energy dissipated between the tip and the sample, following Eq. 2.10 [50, 53]. Such kind of variation are visible in Fig 4.5b, where the recorded phase lies between 57° and 79° and clusters with different contrast are visible. These differences can be due to differences in the crystalline content in different areas of the sample, as well as to variations present in the composition of the layers. As EDX and FTIR measurements reveal a non-homogeneous distribution of the oxygen within the layers, it is possible to attribute the observed phase variations to the different oxygen content in different areas of the layer. This is, therefore, another indication of the relocation of oxygen within the layers after the annealing, in agreement with the structural results shown in Sec. 4.1.3 and 4.1.4.

The surface evolution with respect to the annealing time is measured with AFM in tapping mode, attractive regime (i.e. $\varphi > 90°$). A super-sharp tip (NT-MDT NSC-DLC) has been used for imaging and the regime chosen

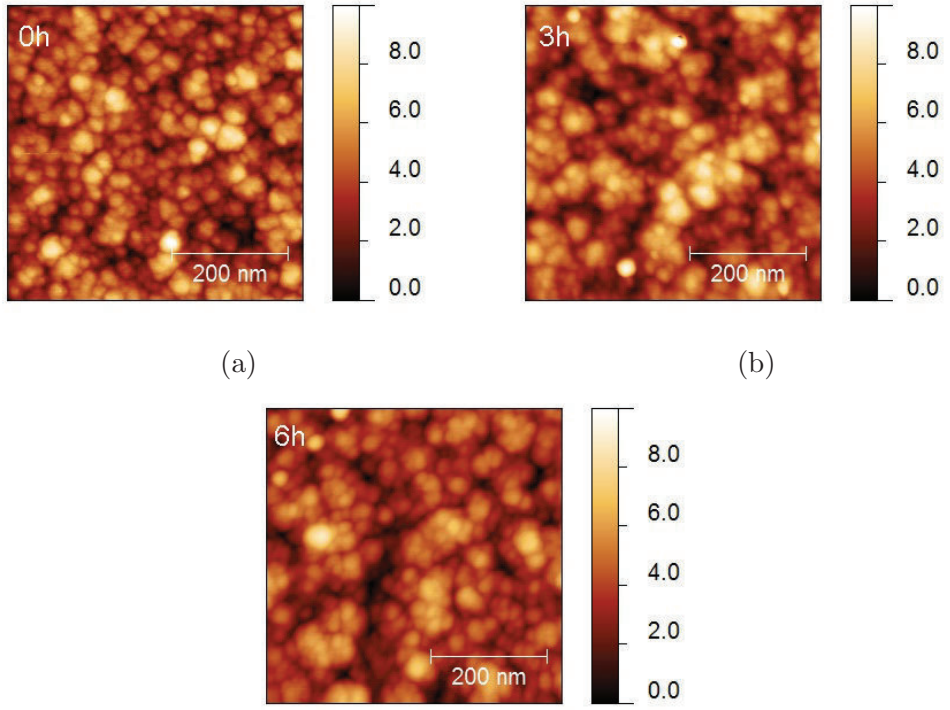

Figure 4.6: AFM topography map of a SiO_xN_y film (R_{N2O}=16%) in the as-deposited state (a) and after 3 h (b) and 6 h (c) annealing [44].

allowed to limit tip damage and to obtain defined images. Figure 4.6 depicts the recorded topography of sample B in the as-deposited state (Fig. 4.6a) and after 3 h (Fig. 4.6b) and 6 h (Fig. 4.6c) of annealing. It has been observed that larger clusters are emerging with increasing annealing time. In order to quantify the surface modifications as a function of the annealing time, the lateral correlation length ξ has been evaluated from the HHCF (Eq. 2.11) and the Watershed method described in Sec. 2.3. The lateral correlation length is a measure of the size of the mounds present on the surface.

The quantities that can be extracted from the fit of the HHCF are the roughness of the surface (R_{HHCF}), the correlation length (ξ) and the roughness parameter (α), as described in Sec. 2.3.2. The roughness obtained by this method can be compared with the averaged root mean square roughness (R_q). The HHCF has been evaluated for maps taken in different areas of

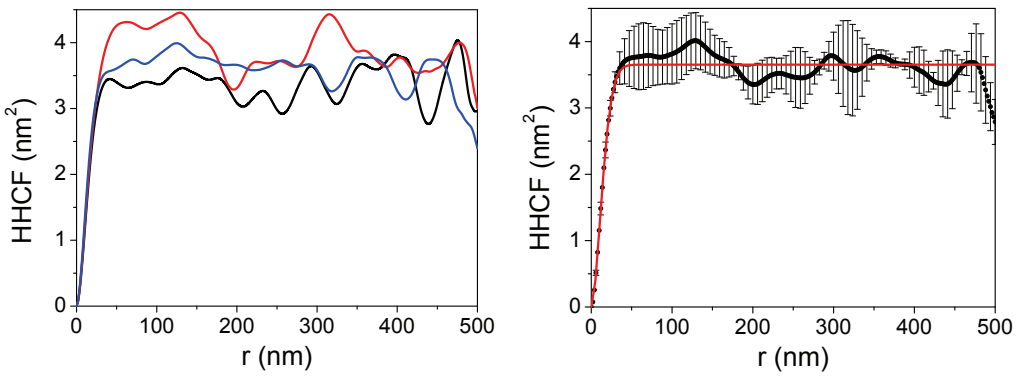

(a) (b)

Figure 4.7: a) HHCF obtained from three different AFM maps taken in different areas of sample B (R_{N2O}=16.7%), as-deposited. b) Averaged HHF of sample B, as-deposited. The solid line represent the fit to the HHCF.

the sample. Figure 4.7a reports the HHCF obtained for three 0.5x0.5 μm^2 maps of sample B (R_{N2O}=16.7%, as-deposited state) plotted as a function of the surface points distance. A fit of the HHCF has been performed using Eq. 2.16 on the HHCF averaged over three different maps for each sample analyzed. An example of the fit is shown in Fig 4.7b, where the markers represent the averaged HHCF and the solid line is the result of the fitting procedures. It is worth noting that the HHCF curves obtained for single AFM maps show variations in the region where $r >> \xi$ (Fig. 4.7a). This effect is due to the finite size investigated by the AFM and evaluating the HHCF for more maps and taking the average value is equal to a bigger sampling, as shown in Ref. [56]. The variation observed for $r >> \xi$ are reduced when the average HHCF is calculated (Fig. 4.7b), as it is expected when the size of the investigated area for self-affine surfaces is increased [56].

The results obtained for sample B (R_{N2O}=16.7%) in the as-deposited state and after the thermal treatment are reported in Tab. 4.1. The values of the surface roughness R_{HHCF} and R_q do not change as a function of the annealing time within the standard deviation. It is worth noting that the errors reported in Tab. 4.1 are only the statistical ones, i.e. the ones that arise from the average over different maps. Therefore, the small errors associated to R_{HHCF} indicate that this quantity is less sensitive to variations over

Annealing time (h)	R_q (nm)	R_{HHCF} (nm)	α
0	1.3 ± 0.1	1.35 ± 0.01	0.89 ± 0.01
3	1.4 ± 0.1	1.36 ± 0.01	0.94 ± 0.04
6	1.3 ± 0.1	1.26 ± 0.01	0.94 ± 0.03

Table 4.1: Root mean square roughness (R_q), HHCF roughness (R_{HHCF}) and α as a function of the annealing time for sample B (R_{N2O}=16.7%). The errors reported are standard deviations.

different areas of the sample with respect to R_q. A study of the systematic sources of errors to these quantities needs to be performed in order to evaluate their contribution to the analysis. Anyhow, statistical errors lower than 1% are guaranteed by HHCF analysis. The obtained values of the roughness parameter are between 0.8 and 1, similar to what is expected for Si [83–85]. The results relative to the lateral correlation length will be presented in comparison with the ones obtained with the Watershed method later on in this section.

The results of the HHCF analysis relative to different R_{N2O} values are reported in Tab. 4.2. All the samples analyzed were annealed for 3 h. No significant differences between the recorded surface roughness can be observed for R_{N2O} values up to 28.6%. A slight increase can be seen for sample E, which has a high R_{N2O} value of 47.4%. This increase can be due to a higher disorder of the layer, which shows a lower crystalline fraction (70%) than the others ($\chi > 75\%$), as reported in Tab. 4.3. The enhanced disorder of this layer can be the source of the increase in the recorded roughness. The values of R_{HHCF} and R_q are compatible with each other within the errors and α lies between 0.8 and 1.

The lateral correlation length ξ can be evaluated from the fit of the HHCF and from the Watershed method, as described in Sec. 2.3. The first step in the Watershed analysis is the location of the grains present on the AFM maps and their segmentation. The two main sources of errors in this procedure are the following: a single grain could be split in two or more grains and several different grains could be grouped together in a single grain. The parameters showed in Tab. 4.4 are the best choice for the samples under investigation

Sample name	R_{N2O} (%)	R_q (nm)	R_{HHCF} (nm)	α
A	9.09	1.4 ± 0.1	1.49 ± 0.01	0.84 ± 0.01
B	16.7	1.4 ± 0.1	1.36 ± 0.01	0.94 ± 0.04
C	23.1	1.3 ± 0.1	1.31 ± 0.01	0.92 ± 0.01
D	28.6	1.4 ± 0.1	1.41 ± 0.01	0.86 ± 0.02
E	47.4	1.6 ± 0.1	1.59 ± 0.01	0.90 ± 0.02

Table 4.2: Root mean square roughness (R_q), HHCF roughness (R_{HHCF}) and α as a function of R_{N2O} for 3 h annealed samples. The errors reported are standard deviations.

Sample name	R_{N2O} (%)	χ (%)
A	9.09	88 ± 2
B	16.7	82 ± 2
C	23.1	81 ± 2
D	28.6	77 ± 2
E	47.4	70 ± 2

Table 4.3: Crystalline fraction χ as a function of R_{N2O} for 3 h annealed samples.

and they strongly depend on the kind of morphology under study.

The software *Gwyddion* has been used for the grain identification with the parameters of Tab. 4.4 and the software produces a mask superimposed to the original AFM map that represents the identified grains. Statistical information, such as grain number and equivalent disc radius distributions, are also available after the identification.

Two sources of error in the identification of grains can be present:

- small grains close to each other are grouped and identified as a single grain;
- experimental noise is incorrectly identified as a very small grain.

A careful choice of the parameters reduces the incorrect merging of grains, but very small grains are still incorrectly identified in a lot of cases. The latter are therefore noise contributions left to the analysis. The reason for

Grain location	
Number of steps	1
Drop size	10%
Threshold	2px^2
Segmentation	
Number of steps	100
Drop size	10%

Table 4.4: Watershed parameters used for grain location and segmentation in *Gwyddion*.

the incorrect identification is the following: local minima are identified on the inverted surface when small variations in the topography are recorded due to noise in the AFM measurements. Some of the contributions to this effect are acoustic noise, mechanical vibrations and thermal effects. Even if the experimental set up is optimized for the reduction of the mentioned sources of noise, some effects are anyhow present. Figure 4.8a shows the AFM topography recorded for sample B (R_{N2O}=16.7%) in the as-deposited state and in Fig. 4.8b the mask of identified grains is superimposed to the AFM map.

In order to reduce the contribution of incorrectly identified grains to the analysis results, a threshold to the smallest accepted area can be applied to the mask subsequently. Thresholds from 0 up to 25 px^2 have been applied to the masks and the Equivalent Disc Radius (EDR) distribution is studied. Figure 4.9 depicts the obtained distributions for sample B (R_{N2O}=16.7%, as-deposited) with different threshold applied. The EDR reported in Fig. 4.9a is the one obtained if no threshold is applied to the analysis. The first peak visible for low ERD value is due to the presence of Incorrectly Identified Grains (IIGs). When a threshold of 2 px^2 is applied, this peak is strongly reduced, as it can be seen in Fig. 4.9b. The increase of the threshold value leads to an incorrect increase of the average EDR, because real grains are removed from the mask in this case. This effect is underlined by Fig. 4.9c, where a 19 px^2 threshold is applied. The value chosen for the Watershed

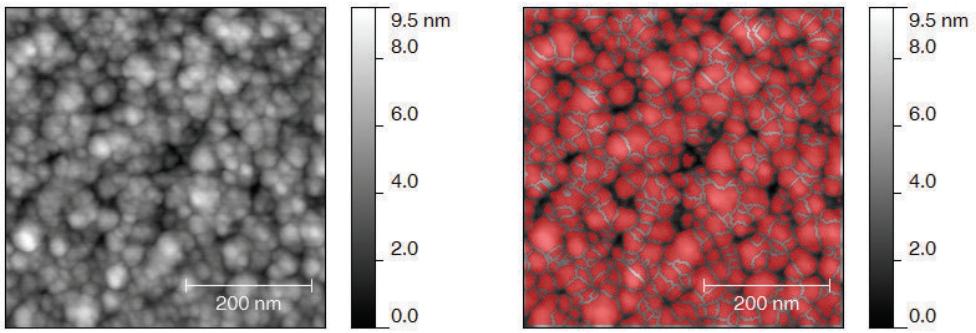

(a) (b)

Figure 4.8: a) AFM topography map of sample B (R_{N2O}=16.7%), as-deposited. b) Watershed mask superimposed to the topography map of sample B.

analysis is 2 px^2, as this threshold guarantees a significant reduction of noise without removing grains relevant for the analysis.

The lateral correlation length obtained with HHCF and Watershed analyses is reported in Fig. 4.10. Figure 4.10a shows ξ as a function of the annealing time for sample B (R_{N2O}=16.7%) in the as-deposited state and after annealing, while in Fig. 4.10b ξ is plotted as a function of R_{N2O} for 3 h annealed samples. The increase of ξ with the annealing time (Fig. 4.10a) indicates that the mounds enlarge with annealing time, which is quite typical in 3D growth [86]. The increase of ξ observed with increasing N_2O dilution (Fig. 4.10b) indicates the formation of larger mounds that could be related the observed changes of the structural properties of the SiO_xN_y layers with increasing R_{N2O}, such as increased the increased disorder observed with oxygen incorporation within the films (Fig. 4.2b). ξ obtained with HHCF and Watershed analysis shows a similar increasing trend with respect to increasing annealing time and R_{N2O} and the errors associated to the Watershed results are larger. This is due to the higher statistical fluctuation of Watershed analysis with respect to the HHCF one. More statistic is therefore needed to obtain reliable results with the Watershed method.

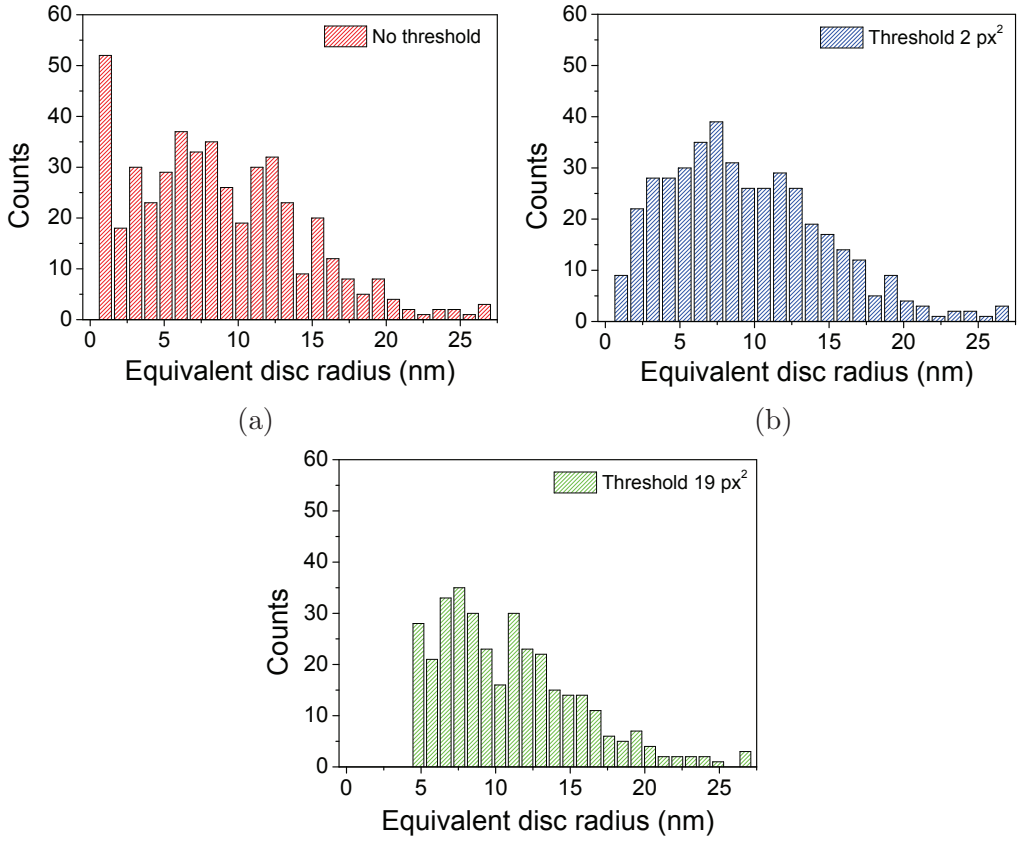

Figure 4.9: Equivalent disc radius distribution of an AFM map of sample B (R_{N2O}=16.7%) with no threshold applied (a) and with a threshold applied of 2 px^2 (b) and 19 px^2 (c).

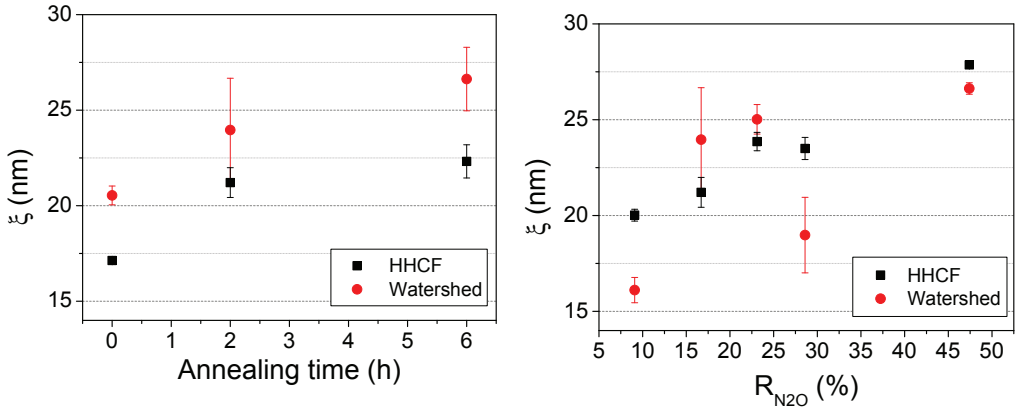

(a) (b)

Figure 4.10: Lateral correlation length ξ depending on annealing time (a) and N_2O dilution (b) determined via the HHCF and Watershed analyses.

4.3 Conductivity analyses: c-AFM and temperature dependent conductivity

The conductivity of the SiO_xN_y layers has been investigated both at macroscopical and microscopical level. In order to gain information about the transport properties at the nano-scale, AFM microscopy in current mode (c-AFM) has been used. The measurements have been performed following the scheme depicted in Sec. 2.3. Figure 4.11 shows the recorded topography (Fig. 4.11a) and current (Fig. 4.11b) of sample A (R_{N2O}=9.09%, 3 h annealed).

The c-AFM map shows dark grains with an enhanced conductivity, likely related to clusters of nanocrystals that could have a higher Si content with respect to the surrounding matrix. In addition, grains with quite different conductivity appear in the map. The reason can be the size of the nanocrystals itself, which can cause different effective doping concentrations [30, 87] and/or the grain composition. The crystalline phase has a strong role in conductivity enhancement as demonstrated by macroscopical current-voltage measurements, which show that conductivity increases with the crystalline fraction (Fig. 4.12a). Therefore, the dark conductive grains in Fig. 4.11b

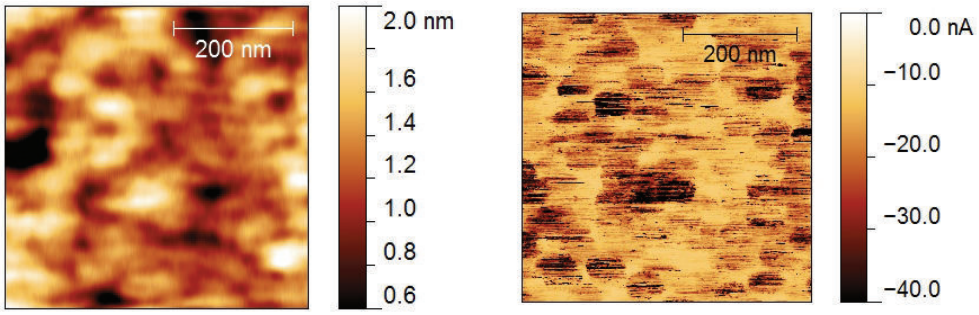

(a) (b)

Figure 4.11: (a) Topography and (b) c-AFM map for sample A (R_{N2O}=9.09%, 3 h annealed). Differences in the conductivity can be associated with the presence of the nanocrystals [44].

could likely be related to regions with high crystalline content. Those grains could be formed of clustering of nanocrystals with high Si content. Structural measurements have pointed out that oxygen incorporation within the layers results in enhanced crystalline disorder (Fig. 4.2b), therefore oxygen could cluster at the amorphous sites, leading to lower local conductivity paths observed by c-AFM (Fig. 4.11b). Similar behavior has been observed for samples with different R_{N2O} content.

The room temperature dark conductivity σ_{dark} measured by IV analyses follows the trend of the crystalline fraction, decreasing with rising N_2O dilution (Fig. 4.12b) and a very high dark conductivity up to 44 S/cm can be reached in the annealed state for sample A (R_{N2O}=9.09%, 3 h annealed). No significant difference in dark conductivity between the 3 h and 6 h annealed films could be found. The activation energy E_a and the pre-factor σ_0 have been calculated from temperature dependent conductivity measurements and have been plotted in Fig. 4.12c and Fig. 4.12d, respectively. The pre-factor σ_0 follows the same trend of the crystalline fraction, while the activation energy E_a shows an increasing trend with N_2O dilution. E_a represents the amount of energy required for the conduction to occur, and its increase with N_2O dilution can be explained by taking into account that a higher R_{N2O} improves the amount of the amorphous phase, which impedes conduction.

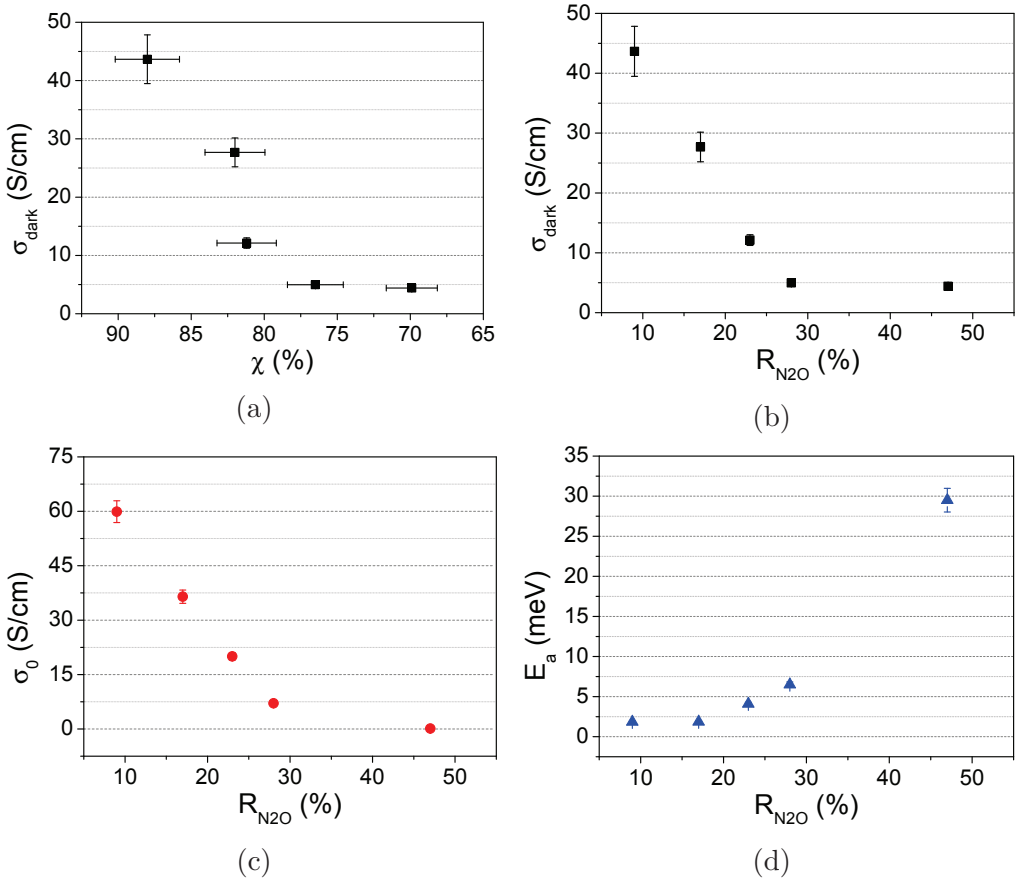

Figure 4.12: a) Room temperature dark conductivity σ_{dark} as a function of the crystalline fraction after 3 h annealing. Room temperature dark conductivity σ_{dark} (b), pre-factor σ_0 (c) and activation energy E_a (d) as a function of N_2O dilution after 3 h annealing; [44].

In addition, very small values of E_a, ranging from 1.85 to 29.5 meV have been obtained (Fig. 4.12d), showing the very good transport properties of these layers. This result evidences the role played by the crystalline fraction in the electrical conduction in SiO_xN_y films.

4.4 Optical analyses: Tauc gap

Optical spectroscopy analyses have been performed to determine the Tauc optical band gap, E_{Tauc}, as defined in Eq. 2.22. The Reflection and Trans-

mission (R&T) spectra of the SiO_xN_y layers deposited on glass have been measured and compared with a Si reference sample, obtained with the same deposition condition of the SiO_xN_y layers and R_{N2O}=0% (sample R, Tab. 2.2). Figure 4.13a and Fig. 4.13b show the measured transmission and reflection spectra of the reference Si layer, respectively. In both cases thin film interference fringes are visible. The effect of the annealing on the Si sample is to enhance the transmission as well as the modulation present for reflection at low wavelengths. No significant differences can be observed between 3 and 6 h of annealing.

The measured R&T spectra for sample B (R_{N2O}=16.7%) are reported in Fig. 4.13c and Fig. 4.13d. The effect of the thermal treatment on the layer is similar to what happens in the case of the reference Si sample. The enhancement of the transmission at low wavelengths, as well as the increased modulation present in the reflection spectrum at low wavelengths can be related to the increased crystalline fraction measured by Raman spectroscopy after the annealing (Fig. 4.2a). Simulations performed using the software *Optical* for a mixed Si material where amorphous and crystalline material coexist are reported in the Fig 4.13e and Fig. 4.13f. Three different values of crystalline fraction have been considered (χ =0%, 50%, 100%) and the same trend of the experimental data for the transmission and reflection spectra can be observed.

Figure 4.14a and Fig. 4.14b depict the R&T spectra for samples with different R_{N2O}, in the as-deposited state. The variations in the spectra with increasing R_{N2O} are related to an increased oxygen content within the layer, which contributes to an increased Tauc gap of the layers, as will be shown in the following results. The change in the peak position can be related to both the different thickness of the layers (Tab. 2.2) and the change expected in the refractive index due to an increased O-content. The peak position is indeed given by $2nd = m\lambda$, where n is the refractive index, d the layer thickness, m the order of the maximum and λ the wavelength, thus its position depends on the value of n.

The values of the absorption coefficient α have been evaluated from the R&T spectra using Eq. 2.21 to reduce the effect of the interference fringes

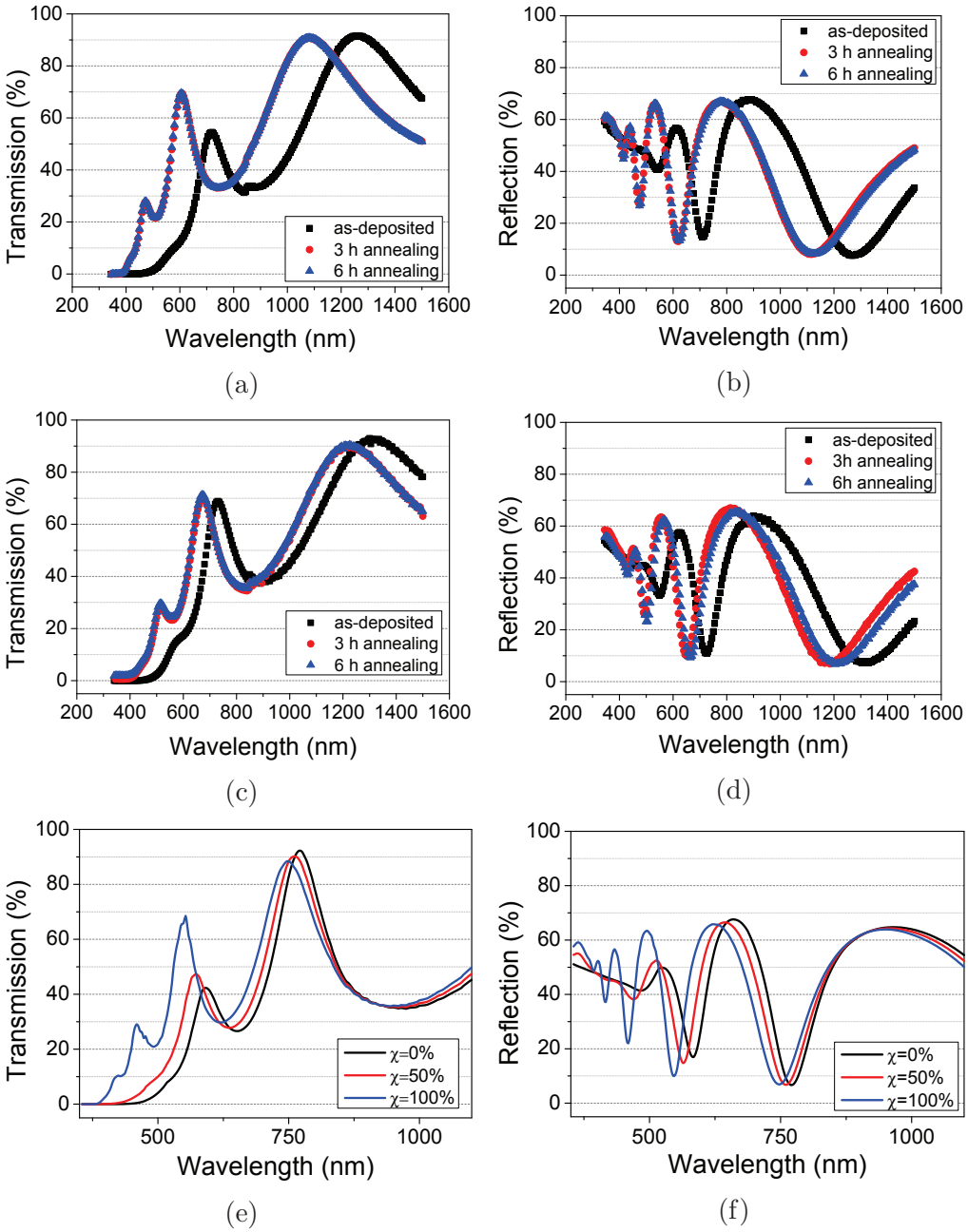

Figure 4.13: Transmission (a) and reflection (b) spectra of Si for different annealing times; transmission (c) and reflection (d) spectra of sample B (R_{N2O}=16.7%) for different annealing times; Simulated transmission (e) and reflection (f) spectra of Si for different crystalline fraction. The thickness of the simulated layer is 200 nm.

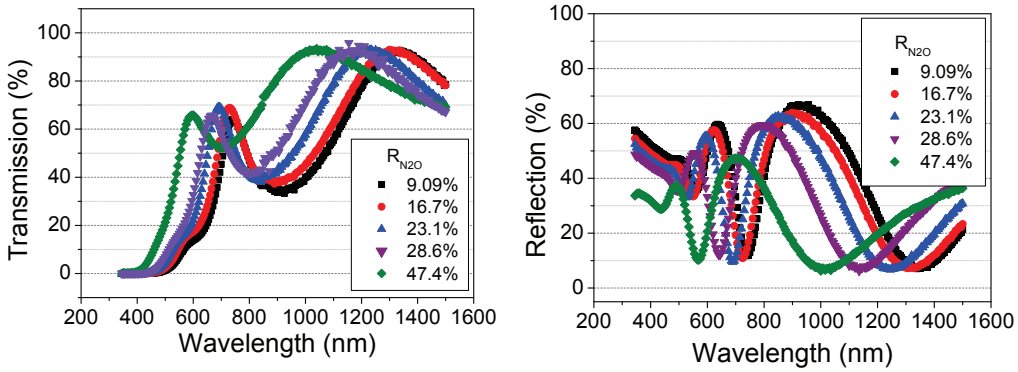

(a) (b)

Figure 4.14: Transmission (a) and reflection (b) spectra of SiO_xN_y layers annealed for 3 h.

on the analysis. Figure 4.15a depicts the measured spectra of sample B (R_{N2O}=16.7%, as-deposited state) as well as the quantity $T/(1-R)$. The latter shows a significant reduction of the thin film interference, in agreement with Hishikawa *et al.* [65]. This desirable effect is achieved for the as-deposited samples in a larger wavelength range than the annealed ones. However, in the region of high absorption the fringes are reduced in the annealed layers as well, as it can be seen in Fig. 4.15b. The different behavior of the as-deposited and annealed samples can be attributed to the phase separation that occurs during annealing, as in the layers different phases and composition coexist, giving rise to internal scattering in regions with different refractive index. The Tauc gap has been obtained from a linear fit in the region of high absorption following Eq. 2.22 for all the analyzed samples. Figure 4.15c depicts $(\alpha h\nu)^{1/2}$ as a function of $h\nu$ for sample B (R_{N2O}=16.7%) and the lines represent the fits (the solid, dashed and dot lines are relative to as-deposited, 3 h and 6 h annealed samples, respectively). The intersection of the linear fit with the x-axis gives the value of the Tauc gap.

The obtained values of E_{Tauc} are reported in Fig. 4.16 as a function of R_{N2O} for the as-deposited SiO_xN_y layers as well as the annealed ones. E_{Tauc} increases linearly with N_2O dilution in the as-deposited state and this fact can be due to a higher oxygen incorporation within the film (Fig. 4.16 and [12]). After the annealing, no trend of E_{Tauc} with N_2O dilution can be observed,

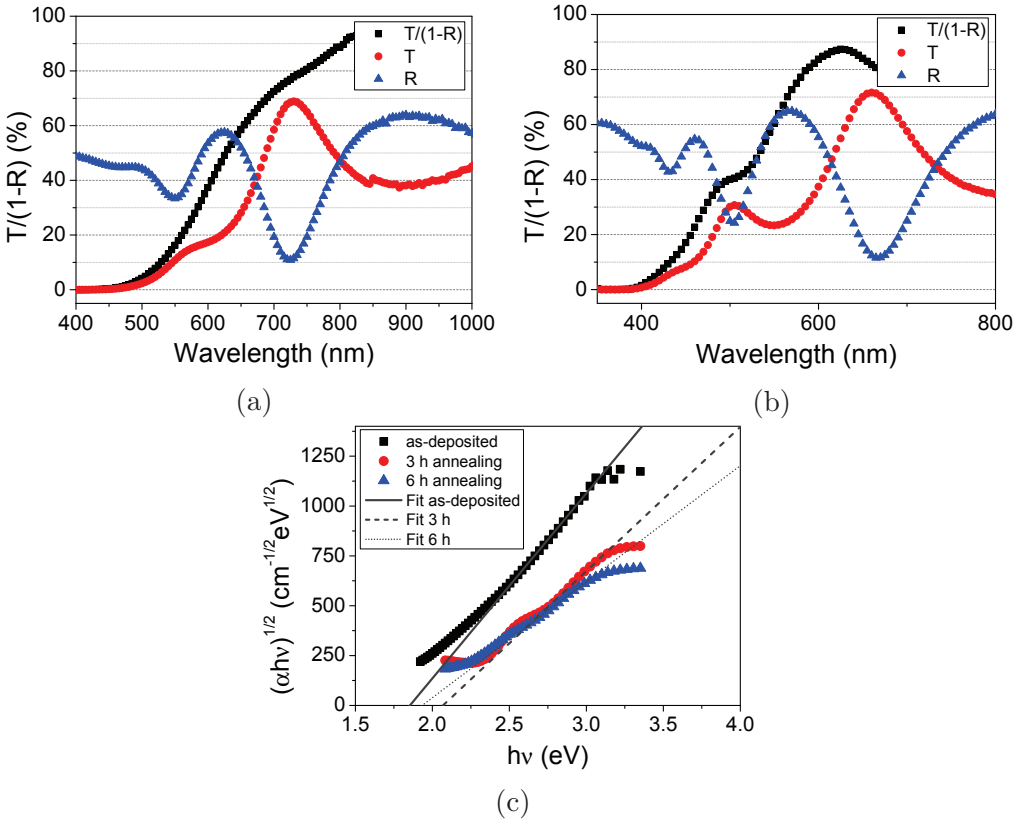

Figure 4.15: Transmission, reflection and $T/(1-R)$ spectra of sample B (R_{N2O}=16.7%, as-deposited) (a) and sample A (R_{N2O}=9.09%, 3 h annealed) (b). c) Tauc plot of sample B for different annealing times. The lines represent the fit for E_{Tauc} determination.

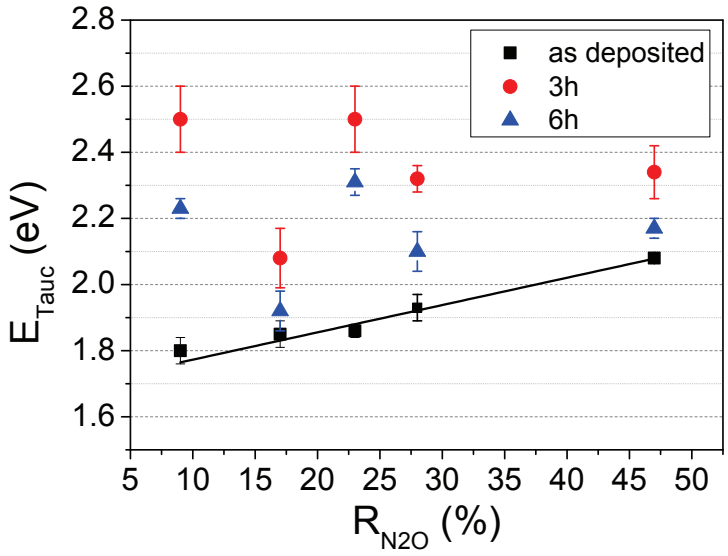

Figure 4.16: E_{Tauc} as a function of the N_2O dilution for different annealing times. The solid line is a linear fit of the data points relative to the as-deposited SiO_xN_y layers [44].

but E_{Tauc} is generally larger after the thermal treatment. The increase of E_{Tauc} after 3 h annealing could be due to two different effects: 3 h annealing leads to the formation of nanocrystals smaller than 10 nm as observed by HR-TEM, which could cause quantum confinement effects [26], and to the formation of O-rich areas, that could shift the gap of the layer towards the SiO_2 gap (9.3 eV [88]). The decrease of E_{Tauc} from 3 h to 6 h annealing can be related to the formation of larger nanocrystals and thus to a reduced quantum confinement effect [26].

The Tauc gap determination of the SiO_xN_y layers have revealed the effect of the thermal treatment as well as of the oxygen incorporation on the optical properties of the layers. The reduced absorption of the SiO_xN_y films after the annealing is a suitable property for the application in the photovoltaic field as the absorption within the emitter layer is undesirable as the carriers recombine before the extraction, as pointed out in Sec. 1.3.2.

4.5 Conclusions

The annealing process deeply affects the structure of the analyzed samples. The thermal treatment is effective in the enhancement of the crystalline content of the thin films, reaching a maximum value of 88% for sample A (R_{N2O}=9.09%). An annealing of 3 h is sufficient for obtaining high χ values, as no significant improvement is visible after additional 3 h. FTIR and EDX measurements reveal oxygen relocation within the layers during the annealing process, with the formation of oxygen-rich areas.

The band gap of the SiO_xN_y layers increases after the annealing for all R_{N2O} values and this observation can be due to both quantum confinement effects and the formation of oxygen-rich areas, with a shift of the gap towards SiO_2 values. The decrease observed after additional 3 h of annealing can be due to the formation of larger nanocrystals.

The morphology of the layers changes with the thermal treatment: an increase of the lateral correlation length ξ is observed with respect to the as-deposited samples with both HHCF and Watershed data analyses, indicating the presence of larger structure on the sample surface.

The effects of the oxygen incorporation within the nc-SiO_xN_y layers have been studied and a general increase of the disorder is observed. The crystalline fraction χ decreases from 88% for sample A (R_{N2O}=9.09%) to 70% for sample E (R_{N2O}=47.4%) and a consequent decrease of the lateral dark conductivity σ_{dark} is observed. The activation energy E_a measured for the layers increases with R_{N2O} and small values of E_a have been obtained (1.85-29.5 meV). This result, together with the very high conductivity (up to 44 S/cm), shows the very good transport properties of the layers.

The conductivity at the nano-scale has been investigated by c-AFM and grains with higher conductivity with respect to the surrounding matrix are evidenced by the maps of the annealed layers. Oxygen rich clusters can be related to the less conductive paths observed by c-AFM.

The increase of the oxygen content within the layers results in a generally larger lateral correlation length, as it is observed with both HHFC and Watershed analyses. The Tauc gap shows an increasing linear trend with higher

R_{N2O} for the as-deposited layers, due to a higher incorporation within the layers. No trend is observed for the annealed layers.

Sample A, which has has been deposited with low N_2O dilution (R_{N2O}=9.09%), shows optimum performances for photovoltaic applications. The measured lateral dark conductivity σ_{dark}, Tauc gap E_t, activation energy E_a and crystalline fraction χ are the following: $\sigma_{dark} = (44 \pm 4)$ S/cm, E_{Tauc}=(2.5 ± 0.1) eV, E_a=(1.85 ± 0.09) meV and χ= (88 ± 2)%, values which are significantly different than the ones obtained for nc-Si:H deposited in similar conditions (σ_{dark} = 1.7 S/cm, E_{Tauc}=2.06 eV and E_a=77 meV).

High crystalline fraction values of SiO_xN_y layers could be obtained also by increasing the H_2 dilution in the PECVD deposition step, thus making this material suitable for photovoltaic applications.

Conclusions

Silicon Rich Carbide (SRC)/SiC multilayers and SiO_xN_y thin films have been studied in view of their application in third generation photovoltaics. The deep knowledge and improved understanding of the basic physical properties of these quite complex, multi-phase and multi-component systems, made by nanocrystals and amorphous phases, will contribute to improve the efficiency of Si based solar cells. Si is an abundant, non-toxic element, suitable for worldwide terrestrial and low cost PV applications. In 2013 Si-wafer based PV technology accounted for about 90% of the total production [89]. An improvement of Si based solar cell efficiency behind the actual values can thus significantly impact PV technology. From the obtained experimental results, the following conclusions can be drawn.

SRC/SiC multilayers are promising within the field of photovoltaic as they offer a tunability of their band gap thanks to the quantum confinement capability of the Si nanocrystals (NCs) [6]. However, different phases (amorphous/crystalline) and compositions (Si and SiC) coexist in such systems and formulating a model of the structure and of the transport properties is challenging. Therefore, the properties of the multilayers (ML) have been investigated through Atomic Force Microscpoy (AFM), optical spectroscopy and conductivity measurements. In particular, the effect of the variation of the SRC layer thickness (d_{SRC}) has been clarified.

The tip-sample energy dissipation is mapped at the nano-scale and reveals inhomogeneities in the sample composition and the coexistence of different phases (amorphous and crystalline). Si and SiC crystalline and amorphous volume fractions have been determined from the simulation of reflection and transmission spectra. The results show that multiple phases and composi-

tions coexist [43].

c-AFM imaging has shown variations in the conductivity at the nanoscale. This result is in agreement with what is observed in phase contrast imaging, and it is due to the differences in sample composition and crystallinity. Clusters with significantly different conductivity have been observed. Local IV measurements have been acquired with the AFM and show a defined increasing trend with d_{SRC}, in agreement with what it is observed by macroscopical conductivity measured through the deposited Ni contacts. The comparison between microscopical and macroscopical electrical measurements, and in particular the evaluation of results in view of the Meyer-Neldel rule, suggests the presence of preferential conduction paths through the disordered tissue surrounding the clusters. The conduction mechanism, when the multilayer structure is maintained, is likely band-like. Moreover, the conduction mechanism occurs via band states likely located at the disordered tissue at the interface between nanodot clusters.

This result significantly differs from the case of Si nanodots in a SiO_2 matrix, where field dependent conduction mechanisms are observed [90]. In band-like conduction, defect states and disordered tissue should play a major role in the electrical transport, similarly to what is observed in nc-Si and nc-SiC, where hydrogen or chlorine passivation have been tried in order to reduce the defect role [90–93]. However, even with comparable activation energy, the dark conductivity of SRC/SiC multilayers is remarkably higher than the one of nc-SiC, showing better conduction properties of the layers under investigation.

The band-like conduction observed for larger SRC thickness, which is a prerequisite for high mobility transport, is an encouraging feature in view of applications in photovoltaic of the Si NCs/SiC system. The material is expected to combine the needed tunable absorption properties with efficient charge collection and conduction.

In addition to SRC/SiC multilayers, SiO_xN_y thin films deposited by PECVD have been studied in this thesis. SiO_xN_y thin films show promising features for their application in the photovoltaic field. In particular, amorphous silicon oxy-nitride (a-SiO_xN_y) could replace amorphous silicon

as emitter layer in Silicon HeteroJunction (SHJ) solar cells thanks to its reduced parasitic light absorption [10, 11]. Nanocrystalline films can lead to an increased efficiency thanks to the lower contact resistance with the transparent conductive oxide layer [13]. Therefore, the characterization of nc-SiO_xN_y thin films has been carried out in order to clarify the effect of crystallization on the properties of the films.

The crystallization of SiO_xN_y layers with respect to the annealing time and the N_2O dilution during deposition have been studied, as well as the influence of these two parameters on the properties of the layers [44]. The obtained results show that the material undergoes a phase transition from a homogeneously distributed material in terms of Si-Si and Si-O-Si bonds towards a two phase material consisting of Si-rich and O-rich clusters during annealing. Both phase separation and increase of crystalline fraction χ upon annealing could be responsible for the increase of the conductivity. In particular, oxygen rich clusters seem to be related to the less conductive paths observed by c-AFM. An increase of N_2O dilution causes an enhancement of crystal disorder, revealed through a decrease of the crystalline fraction and an increase of the lateral correlation length.

The electrical and optical studies show that the layers exhibit very high conductivity σ_{dark}, low activation energy E_a and high Tauc gap $\mathrm{E_{Tauc}}$, a very interesting characteristic for their application in Si-based heterojunction solar cells, where low parasitic absorption and high conductivity are required.

In particular, the films deposited with low N_2O dilution ($\mathrm{R_{N2O}}$=9%) and annealed for 3 h at 800°C show optimal performances for photovoltaic applications: $\sigma_{\mathrm{dark}} = (44 \pm 4)$ S/cm, $\mathrm{E_{Tauc}}$=(2.5 ± 0.1) eV, E_a=(1.85 ± 0.09) meV and χ= (88 ± 2)%, values which are significantly different than the ones obtained for nc-Si:H deposited in similar conditions ($\sigma_{\mathrm{dark}} = 1.7$ S/cm, $\mathrm{E_{Tauc}}$=2.1 eV and E_a=77 meV).

High crystalline fraction values of SiO_xN_y layers could be obtained also by increasing the H_2 dilution in the PECVD deposition step, thus making this material suitable for photovoltaic applications.

In conclusion, the study of nc-SiO_xN_y thin films has clarified the role of crystallinity in the enhancement of the optical and electrical properties of

SiO_xN_y layers. The study also evidences annealing-induced phase separation, in particular oxygen relocation within the layers. The improved knowledge of the microscopical and macroscopical properties of these layers is very important for its use as window layer in innovative Si based heterojunction solar cells.

Further analyses on the electrical transport at the nano-scale for SiO_xN_y layers and a detailed study on the morphology evolution are needed. Simulation tools can be employed within this framework to better understand the obtained results. High values of crystalline fraction should be obtained without the annealing step. One way to do this is to increase the hydrogen content during the deposition. Both SRC/SiC multilayers and SiO_xN_y thin films should then be employed for the realization of solar cells, in order to further optimize the material properties for increasing the cell efficiency.

The research in the photovoltaic field is of major importance to address the problem of climate change. Several different technologies exist to convert solar light into electricity, but nowadays silicon based solar cells still represent the majority of the market. Silicon is a non-toxic material, abundant and widely distributed and offers a mature technology. However, the record efficiency for silicon Heterojunction with Intrinsic Thin layer (HIT) is 25.6% [23], therefore the improvement of the efficiency of Si based cells is of major importance for phovotoltaic power generation competitiveness. Multijunction approach as well as the employment of quantum confinement properties are possible strategies to address such a problem. A deep knowledge of the physical properties, modeling of the electrical transport and understanding of the optical properties are necessary to achieve this target. With this thesis the transport properties of SRC/SiC systems as well as the nanocrystal formation process in SiO_xN_y thin films have been clarified.

Acknowledgments

I would like to thank my supervisor Prof. Daniela Cavalcoli. This thesis has been possible thanks to her constant and competent guidance and infinite patience. I am extremely grateful for all the time she spent in advising me on the experiments and in discussing the results, constantly helping me in learning how to carry on academic research.

I am very thankful to the collaborators that gave their contribution to the realization of this thesis. In particular, I would like to thank Dr. Caterina Summonte and Dr. Marica Canino from CNR-IMM Institute of Bologna, Italy, for sample preparation and characterization of SRC/SiC multilayers and the useful scientific discussion. My sincere thanks go to the collaborators of University of Konstanz, Germany. I would like to thank Dr. Barbara Terheiden for giving me the great opportunity of being in Konstanz as a visiting student. Many thanks go to Dr. Nils Brinkmann for the extremely valuable contribution in growth and characterization of SiO_xN_y thin films, useful discussion of the results and for sharing his expertise. I would like to thank all the colleagues in Konstanz that advised me in characterization and analyses, especially Svenja Wilking and Daniel Sommer. Thanks to Adnan Hammud, Lisa Mahlstedt and Josh Engelhardt for sample characterization, technical support and useful discussion. I would like also to thank Dr. Tobias Cramer for his contribution in AFM characterization and all the students of Prof. Cavalcoli that worked on this project in the last years.

I gratefully acknowledge the financial support by the PhD scholarship program of the Spinner 2013 Project of the Emilia-Romagna region and the financial support of the Marco Polo project of the Physics and Astronomy Department of the University of Bologna for the months spent in Konstanz.

This work has been possible also because of my wonderful colleagues. Sharing a joyful and cooperative working environment with you, as well as the evenings outside the Department have greatly contributed in overcoming the stressful periods. Thanks to Laura, Geeta, Andrea, Marco the I, Marco the II, Lucia, Isacco, Stefania, Albert, Shankar, Alberto, Giacomo, Tobias, Alessandra and Saurabh. Thanks to Sara, Dave and Nico for the fun at lunchtime and outside the University. I would like to thank Nils, Jan, Sarah, Svenja, Susanne, Erkan, Philipp and Florian for the wonderful time spent in Konstanz.

Dulcis in fundo, thanks to the people that helped me behind the scenes. Because of you and your constant support I was able to achieve my goals. A huge thanks to Ilaria and Giulia L. (yes, it always stands for "Liscia") that were by my side as witnesses at the beginning of the long journey of marriage. Thanks to my family, that always supported me in the last years.

I always leave you as last, but you know you are my best. Thanks to my wonderful husband, Massimo.

Publications and conference presentations

Publications

- M. Perani, N. Brinkmann, A. Hammud, D. Cavalcoli, B. Terheiden, *Nanocrystal formation in silicon oxy-nitride films for photovoltaic applications: optical and electrical properties*, submitted.

- M. Perani, D. Cavalcoli, M. Canino, M. Allegrezza, M. Bellettato, C. Summonte, *Electrical properties of silicon carbide/silicon rich carbide multilayers for photovoltaic applications*, Sol. Energ. Mater. Sol. C. (2014) doi: 10.1016/j.solmat.2014.09.022

- M. Perani, D. Cavalcoli, M. Canino, M. Allegrezza, M. Bellettato, C. Summonte, *Electrical properties of silicon nanodots embedded in a SiC matrix for photovoltaic applications*, Microscopie Anno XI, **1** (21) Marzo 2014

Conference presentations

- M. Perani, D. Cavalcoli, M. Canino, M. Allegrezza, M. Bellettato, C. Summonte, *Silicon Nandotots/ Si Rich Carbide Systems: Investigation of the Electrical Properties for Photovoltaic Applications*, oral contribution at E-MRS Spring Meeting, Lille (FR), May 2014.

- M. Perani, E. di Russo, N. Brinkmann, B. Terheiden, D. Cavalcoli,

Morphology of Multiphase and Functional Thin Films by Atomic Force Microscopy, poster presented at E-MRS Spring Meeting, Lille (FR), May 2014.

- M. Perani, N. Brinkmann, D. Cavalcoli, B. Terheiden, *Nanocrystalline Silicon-Oxy-Nitride Films for Photovoltaic Applications: Electrical, Optical and Structural Properties*, poster presented at E-MRS Spring Meeting, Lille (FR), May 2014.

- M. Perani, D. Cavalcoli, M. Canino, M. Allegrezza, M. Bellettato, C. Summonte, *Electrical properties of silicon nanodots embedded in a SiC matrix for photovoltaic applications*, oral contribution at the workshop Science trough Scanning Probe Microscopy, Bologna, December 2013.

- M. Perani, N. Brinkmann, A. Bauer, D. Cavalcoli, B. Terheiden, *Microstructural and electrical properties of silicon-oxy-nitride layers for photovoltaic applications*, oral contribution at E-MRS Fall Meeting, Warsaw, September 2013.

- M. Perani, D. Cavalcoli, M. Canino, M. Allegrezza, M. Bellettato, C. Summonte, *Electrical properties of Silicon nanodots/Si rich carbide systems for photovoltaic application*, poster presented at the Italian National Conference on Condensed Matter Physics, Milano, September 2013.

- M. Perani, D. Cavalcoli, M. Canino, M. Allegrezza, M. Bellettato, C. Summonte, *Electrical properties of Silicon nanodots/Si rich carbide systems for photovoltaic application*, poster presented at the 27th International Conference on Defects in Semiconductors (ICDS), Bologna, July 2013.

- M. Perani, D. Cavalcoli, A. Cavallini, C. Summonte, M. Canino, M. Allegrezza, M. Bellettato, R. Shukla, I.P. Jain, *Conduction mechanisms in silicon nano-dots/SiC:Si systems investigated by macroscopical and microscopical analyses*, poster presented at International School of Solid State Physics "Materials for Renewable Energy", Erice, July 2012.

Bibliography

[1] T. F. Stocker, D. Qin, G. K. Plattner, et al., eds., *Climate Change 2013: The Physical Science Basis. Contribution of Working Group I to the Fifth Assessment Report of the Intergovernmental Panel on Climate Change*, Cambridge: Cambridge University Press, 2013.

[2] Q. Schiermeier et al., *Energy alternatives: Electricity without carbon*, Nature **454** (2008), 816 –823.

[3] S. De Wolf et al., *High-efficiency Silicon Heterojunction Solar Cells: A Review*, Green **2** (2012), 7–24.

[4] M. A. Green, *Third Generation Photovoltaics Advanced Solar Energy Conversion*, Berlin: Springer, 2003.

[5] G. Conibeer et al., *Silicon nanostructures for third generation photovoltaic solar cells*, Thin Solid Films **511 - 512** (2006), 654 –662.

[6] G. Conibeer et al., *Silicon quantum dot nanostructures for tandem photovoltaic cells*, Thin Solid Films **516** (2008), 6748–6756.

[7] Z. Wan et al., *Rapid thermal annealing and crystallization mechanisms study of silicon nanocrystal in silicon carbide matrix*, Nanoscale Res. Lett. **6** (2011), 129–135.

[8] M. A. Green, *Potential for low dimensional structures in photovoltaics*, Mater. Sci. Eng. B-Solid. **74** (2000), 118 –124.

[9] A. Lambertz et al., *Microcrystalline silicon-oxygen alloys for application in silicon solar cells and modules*, Sol. Energ. Mat. and Sol. C. **119** (2013), 134 –143.

[10] L.V. Mercaldo et al., *Development of mixed phase p-SiO_x by VHF-PECVD for thin film Si solar cells*, Proc. 28th EUPVSEC, Paris (2014), 2588 –2591.

[11] T. Müeller, S. Schwertheim, and W.R. Fahrner, *Crystalline silicon surface passivation by high-frequency plasma-enhanced chemical-vapor-deposited nano-composite silicon suboxides for solar cell applications*, J. Appl. Phys. **107** (2010), 014504.

[12] N. Brinkmann et al., *Electrical, optical and structural investigation of plasma-enhanced chemical-vapour-deposited amorphous silicon oxynitride films for solar cell applications*, Sol. Energ. Mat. and Sol. C. **108** (2013), 180 –188.

[13] S. Olibet, *Properties of interfaces in amorphous/crystalline silicon heterojunctions*, PhD thesis, Institut de Microtechnique Université de Neuchâtel, 2009.

[14] M. Marquis and P. Tans, *A primer on climate change*, in: *Fundamentals of Materials for Energy and Environmental Sustainability*, ed. by D. S. Ginley and D. Cahen, Cambridge: Cambridge University Press, 2012.

[15] N. L. Bindoff, P. A. Stott, K. M. Achutarao, et al., *2013: Detection and Attribution of Climate Change: from Global to Regional*, in: *Climate Change 2013: The Physical Science Basis. Contribution of Working Group I to the Fifth Assessment Report of the Intergovernmental Panel on Climate Change*, ed. by T. F. Stocker, D. Qin, G. K. Plattner, et al., Cambridge: Cambridge University Press, 2013.

[16] G. Flato, J. Marotzke, B. Abiodun, et al., *2013: Evaluation of Climate Models*, in: *Climate Change 2013: The Physical Science Basis. Contribution of Working Group I to the Fifth Assessment Report of the Intergovernmental Panel on Climate Change*, ed. by T. F. Stocker, D. Qin, G. K. Plattner, et al., Cambridge: Cambridge University Press, 2013.

[17] M. Collins, R. Knutti, J. Arblaster, et al., *2013: Long-term Climate Change: Projections, Commitments and Irreversibility*, in: *Climate Change 2013: The Physical Science Basis. Contribution of Working Group I to the Fifth Assessment Report of the Intergovernmental Panel on Climate Change*, ed. by T. F. Stocker, D. Qin, G. K. Plattner, et al., Cambridge: Cambridge University Press, 2013.

[18] B. Kirtman, S. B. Power, J. A. Adedoyin, et al., *2013: Near-term Climate Change: Projections and Predictability*, in: *Climate Change 2013: The Physical Science Basis. Contribution of Working Group I to the Fifth Assessment Report of the Intergovernmental Panel on Climate Change*, ed. by T. F. Stocker, D. Qin, G. K. Plattner, et al., Cambridge: Cambridge University Press, 2013.

[19] R. H. Bube, *Photovoltaic Materials*, London: Imperial College Press, 1998.

[20] National Renewble Energy Laboratory, `http://www.nrel.gov/pv/`.

[21] ASTM G173-03(2012), *Standard Tables for Reference Solar Spectral Irradiances: Direct Normal and Hemispherical on 37° Tilted Surface*, `www.astm.org`, ASTM International, West Conshohocken, PA, 2012.

[22] ASTM E490-00a(2014), *Standard Solar Constant and Zero Air Mass Solar Spectral Irradiance Tables*, `www.astm.org`, ASTM International, West Conshohocken, PA, 2014.

[23] *Panasonic HIT® Solar Cell Achieves World's Highest Energy Conversion Efficiency of 25.6% at Research Level*, `http://news.panasonic.com/press/news/official.data/data.dir/2014/04/en140410-4/en140410-4.html`, 2014.

[24] R. L. Anderson, *Experiments on Ge-GaAs heterojunctions*, Solid State Electron. **5** (1962), 341.

[25] W. Shockley and H. J. Queisser, *Detailed Balance Limit of Efficiency of pn Junction Solar Cells*, J. Appl. Phys. **32** (1961), 510 –519.

[26] F. Priolo et al., *Silicon nanostructures for photonics and photovoltaics*, **9** (2014), 19 –32.

[27] W. D. A. M. de Boer et al., *Red spectral shift and enhanced quantum efficiency in phonon-free photoluminescence from silicon nanocrystals*, Nature Nanotech. **5** (2010), 878 –884.

[28] L. Pavesi, *Photonics applications of nano-silicon*, in: *Frontiers in Optical Technology*, ed. by P. K. Choudhury and O. N. Singh, New York: Nova Science Publishers, 2006.

[29] D. J. Lockwood et al., *Optical properties of porous silicon*, Can. J. Phys. **70** (1992), 1184–1193.

[30] G. Cantele et al., *First-principles study of n- and p-doped silicon nanoclusters*, Phys. Rev. B **72** (2005), 113303.

[31] R. D. Schaller et al., *Seven Excitons at a Cost of One: Redefining the Limits for Conversion Efficiency of Photons into Charge Carriers*, Nano Lett. **6** (2006), 424 –429.

[32] M. C. Beard et al., *Multiple Exciton Generation in Colloidal Silicon Nanocrystals*, Nano Lett. **7** (2007), 2506 –2512.

[33] A. Brewer and K. von Haeften, *In situ passivation and blue luminescence of silicon clusters using a cluster beam/H_2O codeposition production method*, Appl. Phys. Lett. **94** (2009), 261102.

[34] A. Luque and A. Martí, *Increasing the Efficiency of Ideal Solar Cells by Photon Induced Transitions at Intermediate Levels*, Phys. Rev. Lett. **78** (1997), 5014 –5017.

[35] K. W. J. Barnham and G. Duggan, *A new approach to high efficiency multibandgap solar cells*, J. Appl. Phys **67** (1990), 3490 –3493.

[36] K. W. Boer, *Survey of semiconductor physics*, New York: van Nostrand Reinhold, 1990.

[37] T. Saga, *Advances in crystalline silicon solar cell technology for industrial mass production*, Asia Mater. **2** (2010), 69 –102.

[38] A. G. Aberle, *Surface Passivation of Crystalline Silicon Solar Cells: A Review*, Prog. Photovolt: Res. Appl. **8** (2000), 473 –487.

[39] W. T. Read W. Shockley, *Statistics of the ricombinaitons of holes and electrons*, Phys. Rev. **87** (1952), 835.

[40] C. Summonte et al., *Silicon nanoscrystals in carbide matrix*, Sol. Energ. Mat. and Sol. C. **128** (2014), 138–149.

[41] M. Zacharias et al., *Size-controlled highly luminescent silicon nanocrystals: A SiO/SiO_2 superlattice approach*, Appl. Phys. Lett. **80** (2002), 661 –663.

[42] M. Canino et al., *Identification and tackling of a parasitic surface compound in SiC and Si-rich carbide films*, Mat. Sci. Eng. B **178** (2013), 623 –629.

[43] M. Perani et al., *Electrical properties of silicon carbide/silicon rich carbide multilayers for photovoltaic applications*, Sol. Energ. Mat. and Sol. C. (2014), DOI: http://dx.doi.org/10.1016/j.solmat.2014.09.022.

[44] M. Perani et al., *Nanocrystal formation in silicon oxy-nitride films for photovoltaic applications: optical and electrical properties*, submitted.

[45] W.L. Scopel et al., *Chemical and morphological properties of amorphous silicon oxynitride films deposited by plasma enhanced chemical vapor deposition*, J. Non-Cryst. Solids **288** (2001), 88–95.

[46] K. Haga and H. Watanabe, *A structural interpretation of Si-O-Si vibrational absorption of high-photoconductive amorphous a-SiO_x:H films*, J. Non-Cryst. Solids **195** (1996), 72 –75.

[47] E. Vallat-Sauvain et al., *Determination of Raman emission cross-section ratio in hydrogenated microcrystalline silicon*, J. Non-Cryst. Solids **352** (2006), 1200 –1203.

[48] D. Suwito, *Intrinsic and Doped Amorphous Silicon Carbide Films for the Surface Passivation of Silicon Solar Cells*, PhD thesis, University of Konstanz, 2011.

[49] A. A. Langford et al., *Infrared absorption strength and hydrogen content of hydrogenated amorphous silicon*, Phys. Rev. B **45** (1992), 13367–13377.

[50] R. García, R. Magerle, and R. Pérez, *Nanoscale compositional mapping with gentle forces*, Nat. Mater. **6** (2007), 405 –411.

[51] R. García and A. San Paulo, *Attractive and repulsive tip-sample interaction regimes in tapping-mode atomic force microscopy*, Phys. Rev. B **60** (1999), 4961.

[52] R. García and R. Pérez, *Dynamic atomic force microscopy methods*, Surf. Sci. Rep. **47** (2002), 197–301.

[53] R. García et al., *Identification of nanoscale dissipation processes by dynamic atomic force microscopy*, Phys. Rev. Lett. **97** (2006), 016103.

[54] P. Klapetek, D. Nečas, and C. Anderson, *Gwyddion user guide*, 2009, URL: `http://gwyddion.net/documentation/user-guide-en/`.

[55] M. Pelliccione and T. M. Lu, *Evolution of thin film morphology*, Springer, New York, 2007.

[56] Y. Zhao, G. C. Wang, and T. M. Lu, *Characterization of amorphous and crystalline rough surface: principles and applications*, Academic Press, San Diego, 2000.

[57] C. Teichert and I. Beinik, *Conductive Atomiv Force Micriscopy Investigation of Nanostructures in Microelectronics*, in: *Scanning Probe Microscpy in Nanoscience and Nanotechnology 2*, ed. by B. Bhushan, Berlin: Springer, 2011, 691–722.

[58] W. Meyer and H. Neldel, *Relation between the energy constant and the quantity constant in the conductivity-temperature formula of oxide semiconductors*, Z. Tech. Phys.Leipzig **18** (1937), 588 –593.

[59] G. Micard et al., *Conductivity measurement of nanocrystalline silicon thin films grown by LEPECVD for photovoltaic applications*, Proc. 22nd EUPVSEC, Milan (2007), 2169 –2172.

[60] E. Centurioni, *Generalized matrix method for calculation of internal light energy flux in mixed coherent and incoherent multilayers*, Appl. Opt. **44** (2005), 7532–7539.

[61] R. Swanepoel, *Determination of the thickness and optical constants of amorphous silicon*, J. Phys. E: Sci. Instrum. **16** (1983), 1214–1222.

[62] M. Allegrezza et al., *Tail absorption in the determination of optical constants of silicon rich carbides*, Thin Solid Films **556** (2014), 105–111.

[63] G.E. Jellison, M. F. Chisholm, and S. M. Gorbatkin, *Optical functions of chemical vapor deposited thin-film silicon determined by spectroscopic ellipsometry*, Appl. Phys. Lett. **62** (1993), 3348–3350.

[64] L. A. Feitknecht, *Microcrystalline Silicon Solar Cells in the N-I-P configuration: optimisations on light scateering back-reflectors*, PhD thesis, Institut de Microtechnique Université de Neuchâtel, 2003.

[65] Y. Hishikawa et al., *Interference-free determination of the optical absorption coefficient and the optical band gap of amorphous silicon thin films*, Jpn. J. Appl. Phys. **30** (1991), 1008–1014.

[66] J. Tauc, R. Grigorovici, and A. Vancu, *Optical properties and electronic structure of amorphous Germanium*, Phys. Stat. Sol. **15** (1966), 627–637.

[67] S. Janz et al., *Processing and characterisation of tandem solar cells from crystalline silicon materials*, Proc. 28th EUPVSEC, Paris (2014), 142–146.

[68] D.A.G. Bruggeman, *Berechnung verschiedener physikalischer Konstanten von heterogenen Substanzen*, Annalen der Physik (Leipzig) **5** (1935), 636–664.

[69] A. Minj et al., *Strain distribution and defect analysis in III-nitrides by dynamical AFM analysis*, Nanotechnology **24** (2013), 145701.

[70] D. Cavalcoli et al., *Degeneracy and instability of nanocontacts between conductive tips and hydrogenated nanocrystalline Si surfaces in conductive atomic force microscopy*, Nanotechnology **20** (2009), 045702.

[71] A. Vetushka et al., *Comment on "Current routes in hydrogenated microcrystalline silicon"*, Phys. Rev. B **81** (2010), 237301.

[72] D. Cavalcoli et al., *The electrical conductivity of hydrogenated nanocrystalline silicon investigated at the nanoscale*, Nanotechnology **21** (2010), 045702–045706.

[73] D. Azulay et al., *Current routes in hydrogenated microcrystalline silicon*, Phys. Rev. B **71** (2005), 113304.

[74] B. Rezek et al., *Local characterization of electronic transport in microcrystalline silicon thin films with submicron resolution*, Appl. Phys. Lett. **74** (1999), 1475–1477.

[75] Y. Lubianiker and I. Balberg, *Two Meyer-Neldel rules in porous silicon*, Phys. Rev. Lett. **78** (1997), 2433–2436.

[76] S. K. Ram, S. Kumar, and P. Roca i Cabarrocas, *Influence of the statistical shift of Fermi level on the conductivity behavior in microcrystalline silicon*, Phys. Rev. B **77** (2008), 045212.

[77] R.A. Street, *Hydrogenated amorphous silicon*, Cambridge University Press, Cambridge, 1990.

[78] G. Lucovsky et al., *Oxygen-bonding environments in glow-discharge-deposited amorphous silicon-hydrogen alloy films*, Phys. Rev. B **28** (1983), 3225–3233.

[79] M.I. Alayo et al., *On the nitrogen and oxygen incorporation in plasma-enhanced chemical vapor deposition (PECVD) SiO_xN_y films*, Thin Solid Films **402** (2002), 154 –161.

[80] *DIN 50438/1*, 1995.

[81] A. Borghesi et al., *Oxygen precipitation in silicon*, J. Appl. Phys. **77** (1995), 4169 –4244.

[82] S. Gloger, N. Brinkmann, and B. Terheiden, *Low Surface Recombination Velocity using amorphous Silicon on industrial-type cleaned Surfaces*, Energy Procedia **8** (2011), 666 –671.

[83] T. Karabacak et al., *Growth-front roughening in amorphous silicon films by sputtering*, Phys. Rev. B **64** (2001), 085323.

[84] K. R. Bray and G. N. Parsons, *Surface transport kinetics in low-temperature silicon deposition determined from topography evolution*, Phys. Rev. B **65** (2001), 035311.

[85] F. Liu et al., *Kinetic roughening and mound surface growth in microcrystalline silicon thin films*, Phys. Status Solidi C **7** (2010), 533–536.

[86] J. W. Evans, P. A. Thiel, and M. C. Bartelt, *Morphological evolution during epitaxial thin film growth: Formation of 2D islands and 3D mounds*, Surf. Sci. Rep. **61** (2006), 1 –128.

[87] L. E. Ramos et al., *Structural features and electronic properties of group-III-, group-IV-, and goup-V-doped Si nanocrystallites*, J. Phys.: Condens. Matter **19** (2007), 466211.

[88] Z.A. Weinberg, G.W. Rubloff, and E. Bassous, *Transmission, photoconductivity, and the experimental band gap of thermally grown SiO_2 films*, Phys. Rev. B **19** (1979), 3107 –3117.

[89] *Fraunhofer ISE 2014 PV report*, `http://www.ise.fraunhofer.de/de/downloads/pdf-files/aktuelles/photovoltaics-report-in-englischer-sprache.pdf`.

[90] S. Gutsch et al., *Charge transport in Si nanocrystal/SiO_2 superlattices*, J. Appl. Phys **113** (2013), 133703.

[91] K. Ding et al., *Defect passivation by hydrogen reincorporation for silicon quantum dots in SiC/SiO_x hetero-superlattice*, J Non-Cryst. Sol. **358** (2012), 2145–2149.

[92] M. Kořínek et al., *Influence of boron doping and hydrogen passivation on recombination of photoexcited charge carriers in silicon nanocrystal/SiC multilayers*, J. Appl. Phys. **114** (2013), 07310.

[93] R. Wang, X. Pi, and D. Yang, *Surface modification of chlorine-passivated silicon nanocrystals*, Phys. Chem. Chem. Phys. **15** (2013), 1815–1820.